MULTISPECTRAL BIOLUMINESCENCE TOMOGRAPHY WITH SPATIAL PRIORS

MULTISPECTRAL BIOLUMINESCENCE TOMOGRAPHY WITH X-RAY CT SPATIAL PRIORS

By

Julius Pekar, B.Sc.

A Thesis
Submitted to the School of Graduate Studies
In Partial Fulfillment of the Requirements
for the Degree
Doctor of Philosophy

McMaster University

Doctor of Philosophy (2011)		McMaster University
(Medical Physics)		Hamilton, Ontario

TITLE: Multispectral Bioluminescence Tomography with X-ray CT Spatial Priors

AUTHOR: Julius Pekar, B.Sc. (McMaster University)

SUPERVISOR: Professor Michael S. Patterson

NUMBER OF PAGES: xvii, 145.

Abstract

Small animal imaging is a valuable tool in preclinical biomedical research which relies on the use of animal models to understand human disease. Newly emerging optical imaging techniques such as bioluminescence tomography offer an inexpensive and sensitive alternative to more established imaging technologies. These techniques are capable of non-invasively imaging a variety of cellular and molecular processes *in vivo*. As an emerging technology, current bioluminescence imaging methods suffer from several limitations, preventing them from reaching their full potential.

In this work, we describe the design and characterization of an integrated imaging system capable of multispectral bioluminescence tomography (BLT), diffuse optical tomography (DOT), and X-ray computed tomography (CT). The system addresses many of the inherent problems encountered in planar bioluminescence imaging techniques, allowing for the recovery of more accurate and quantitative bioluminescence data. The integrated X-ray CT scanner provides anatomical information which aids in the visualization and localization of the recovered bioluminescence distributions and also helps to constrain the inverse reconstruction in the diffuse optical tomography system. It was found that the inclusion of spatial priors from X-ray CT improved the reconstructed image quality dramatically. Four image reconstruction algorithms were evaluated for their ability to recover the effective attenuation coefficients of a series of test phantoms. Two of the algorithms (a modified Levenberg-Marquardt method, and a single-step Tikhonov method) did not use any *a priori* spatial information. Two other algorithms (hard priors and soft priors) used *a priori* structural information from X-ray CT to constrain the reconstruction process. The two methods incorporating spatial prior information resulted in recovered optical property distributions with RMS errors ranging from 8 % to 15 % in a series of test phantoms versus errors of 11 % to 26 % for non-spatial methods. The soft priors method was shown to be more resilient to imperfect *a priori* information.

The multispectral BLT component was used to recover accurate bioluminescence distributions in test phantoms using *a priori* background optical properties recovered from the DOT system. Multispectral measurements were shown to provide an accurate method for estimating the position of a bioluminescence source due to the wavelength dependent attenuation of tissue. Experimental measurements are presented which explore the importance of accurate estimates of background optical properties in BLT. The hard spatial prior method was found to provide the best overall recovery of total source strength, position, and fidelity at all source depths up to 12.5 mm. The total source strength was recovered to within 8 %, while the source position was recovered to within 0.16 mm in all cases. Errors in recovered power and position showed no dependence on depth up to the maximum of 12.5 mm.

Acknowledgements

I would like to thank my supervisor, Dr. Michael S. Patterson for all his advice, support and encouragement throughout the research of this thesis. I would also like to thank my supervisory committee members, Dr. Tom Farrell and Dr. Troy Farncombe for their guidance and support.

I would like to thank Dr. Douglas Wyman for his help and expertise in radiation protection during the design of the X-ray CT system and Dr. Kevin Diamond for sharing his knowledge and insight into biomedical optics and for the many helpful discussions and suggestions. I would also like to acknowledge the technical expertise provided by the electronics technicians and the machinists at the Juravinski Cancer Centre. My project would not have been possible without their assistance.

I would also like to thank the all of the students and staff that I have had the pleasure to work with during my graduate studies - your friendship and support have made my years at the JCC truly memorable ones.

Finally, I would like to thank my friends and family for their support, especially my parents for always pushing me to do my best. This achievement would not have been possible without their sacrifice, love and support.

Contents

List of Tables

List of Figures

Chapter 1

Introduction

Preclinical biomedical research relies on animal models to understand the pathogenesis of human disease and to provide methods for developing and testing new therapies. Consequently, the *in vivo* imaging of small laboratory animals (i.e. mice and rats) has become an essential component of such research and has resulted in an explosion in the use and development of small animal imaging technologies (1-3). Small-animal imaging provides a non-invasive means of examining biological structure and function, yielding quantitative, spatial and temporal information on normal and diseased tissues such as tumors. Finding ways to conduct animal experiments more accurately and efficiently becomes a key factor in the success and timeliness of such research. Due to the noninvasive nature, imaging allows for longitudinal studies of animal models of human cancer and other diseases over the natural history of the disease process. With the development of genetically engineered, transgenic and knock out rodent models of cancer and other diseases, such models are increasingly more accurate in reproducing the natural history of human disease and the ability to track these disease models long-term is invaluable (4). Unlike cell or tissue culture based experiments, studies in whole animals include all of the interacting physiological factors – neuronal, hormonal, nutritional, immunological, etc. – present in the complex *in vivo* environment. In addition, whole animal models also facilitate the investigation of systemic aspects of disease such as cancer metastasis, which are difficult to replicate in *ex vivo* systems (5).

Dedicated small animal imaging systems have been developed for anatomical, physiological, and molecular applications. Well established technologies such as micro computed X-ray tomography (CT), magnetic resonance imaging (MRI), and ultrasound imaging provide anatomical and physiological information. These systems provide a high degree of spatial resolution and thus excel at imaging anatomic detail. Other technologies such as micro positron emission tomography (PET), single photon emission computed tomography (SPECT), and optical imaging methods including bioluminescence, near infrared, and fluorescence imaging excel at imaging cellular and molecular processes. These relatively new imaging techniques allow for the visualization of normal and abnormal cellular processes in living subjects at the molecular or genetic level rather than at the anatomic level (6). Since molecular and genetic changes precede anatomical changes during disease development, these techniques can detect events that occur during the early stages of disease progression. Among these molecular imaging techniques, optical methods have attracted considerable attention due to their unique advantages.

Optical imaging studies offer excellent performance, and are simpler and more cost effective than other imaging modalities (6). Bioluminescence and fluorescence imaging are among the most widely used optical imaging methods. In fluorescence imaging an external excitation source is required to initiate fluorescence, as a consequence the detector system needs to discriminate between excitation and emission wavelengths. The need for external excitation introduces complications, as a number of endogenous fluorophores in tissue are excited, adding a significant background signal. Even though fluorescent probes generate a stronger signal than bioluminescent probes, the background autofluorescence limits the sensitivity. A major advantage of bioluminescence imaging over fluorescence imaging is its high sensitivity, due to the absence of background light emission from external illumination (7). Bioluminescence imaging has found many uses in small animal imaging including the study of gene therapy and targeted gene expression (8), the detection of protein–protein interactions (9, 10), monitoring of tumor growth, metastasis, and therapeutic response (11-13), and in drug development (14).

Optical imaging methods such as bioluminescence imaging rely on the detection of photons emitted from living tissues. The interpretation of these raw two dimensional bioluminescence images can be difficult due to the scattering and absorption of visible light in biological tissues. Approximately 99% of the bioluminescence signal is lost per centimeter of tissue, and thus, the photon intensity detected at the surface may not proportionately reflect the bioluminescence emitted at depth. In addition, the photons that escape are scattered multiple times before reaching the surface resulting in a highly diffuse image (15). Correcting for the effects of absorption and scattering would result in a more quantitative measure of source intensity (related to the number of light emitting cells), position and geometry.

The most common method developed to account for the propagation of photons in tissue is called bioluminescence tomography (BLT). In general, BLT provides a three-dimensional tomographic reconstruction of the distribution of bioluminescence inside the animal from measurements of the emittance on the animal surface. In the past decade, researchers from many institutions have been developing small animal BLT systems for many applications. Despite many promising developments, the quantitative accuracy of BLT is still limited as the inverse problem is ill-posed due to strong light scattering and underdetermined due to the limited boundary measurement data that is available (16).In order to improve the quantitative accuracy of BLT, several attempts have been made to combine it with other anatomic imaging modalities such X-ray CT and MRI. The idea of combining a functional or molecular imaging modality with a high-resolution anatomical imaging modality has been applied previously to optical and nuclear imaging. Examples of this approach can be found in combined PET and X-ray CT systems and combined SPECT and MRI (17, 18). There are two main advantages to such techniques. First, functional information provided by nuclear imaging is easily co-registered with high-resolution anatomical images, improving the visualization of the functional information. Second, the structural *a priori* information can improve the quantitative accuracy of the nuclear imaging by constraining the reconstruction algorithm. Another example of the multi-modality approach is the combination of DOT with MRI and X-ray mammography (19, 20). Similar to PET, DOT is a low-resolution functional imaging modality that uses near-infrared light to investigate the absorption and scattering properties of tissue. Recently DOT has been integrated with other imaging modalities to obtain accurate optical property maps of the tissue under investigation (19, 21, 22). This approach also achieves more accurate information with the inclusion of high-resolution anatomical priors (21, 23).

Similarly, several studies have demonstrated the value of using structural information in BLT. Like the other multi-modality approaches mentioned, the addition of *a priori* structural information to BLT helps in the visualization of bioluminescence information, but more importantly, it can be used to constrain the reconstruction algorithm. Specifically, quantitative accuracy can be improved if the tissue optical heterogeneity is taken into account. The simplest approach is to treat the tissue as an object with homogeneous optical properties (24-28). Alexandrakis *et al*. showed that the assumption of a homogeneous optical property background is inadequate for describing photon transport in optically heterogeneous tissues and leads to inaccurate source localization in the reconstructed images (28). Several groups have proposed the use of a mouse atlas to assign optical property estimates to various tissue regions segmented from *a priori* anatomical information with some success (29-32). The main disadvantage of this solution is that optical property distributions assigned from a library of standard optical properties are not likely to match those found *in vivo*, both in magnitude and position. These effects were investigated by Alexandrakis *et al*. who showed that in the absence of noise, the optical properties need to be within 10 % to 25 % of actual values for successful source recovery (30). A more elaborate method is to obtain and use the actual background optical property distribution through some other measurement technique. The optical property distributions obtained from DOT can be used. The instrumentation used in continuous wave (CW) DOT is very similar to BLT and can be easily integrated into a single multi-modality system.

Some groups have developed systems that combine MRI/DOT/BLT or X-ray CT/BLT however most studies use co-registered X-ray CT/MRI data obtained separately (24), or do not employ the *a priori* anatomical information to constrain the DOT reconstruction (29, 32-34). To date Yan *et al.* are the only group to report a fully integrated BLT/DOT/X-ray CT system (35). The most sophisticated commercial solution available currently (IVIS Spectrum, Caliper LifeSciences, USA) employs a single view tomographic reconstruction geometry and structured light techniques to determine surface contour information. It does not account for the individual variation in the optical properties within the subject, nor does it offer any multi-modality imaging capabilities (though it offers co-registration of independently acquired CT or MRI data) (36).

This thesis describes the development of an integrated multispectral BLT/DOT/X-ray CT imaging system. The system accounts for the propagation of light through tissue by using DOT to recover the background optical property distribution and an integrated cone beam X-ray CT scanner to provide *a priori* anatomical information.

1.1 Bioluminescence Imaging

Bioluminescence refers to the light produced by an enzymatic reaction of a luciferase enzyme with its substrate. Firefly (Photinus pyralis) luciferase is the most commonly used luciferase for molecular imaging. This enzyme oxidizes its substrate, luciferin, in a reaction that requires oxygen and adenosine triphosphate (ATP), emitting light with a broad emission spectrum from approximately 500 nm to 700 nm with a peak at 560 nm (37). Due to tissue attenuation, measureable emissions from firefly luciferase range from 550 nm to 650 nm in small animals. Luciferin distributes throughout an animal rapidly after intraperitoneal injection. Light from firefly luciferase peaks 10–12 minutes after injection of luciferin and decreases slowly over 60 min, providing a broad time window for imaging (38). The combination of enzymatic amplification of signals from luciferase and the insignificant bioluminescence background *in vivo* makes bioluminescence imaging a highly sensitive method for small-animal molecular imaging. The most common method used in bioluminescence imaging is referred to as the reporter gene strategy. In order for living cells to express luciferase, the animal model or cell line needs to be transfected with the gene encoding the luciferase enzyme. When placed under the action of the promoter region of the gene of interest, luciferase is transcribed at the same rate as the gene of interest. Therefore, measuring the amount of luciferase (via light emission) provides a measure of the activity of the gene of interest (6).

1.1.1 Bioluminescence Imaging Instrumentation

In bioluminescence imaging the goal is to detect the light emitted from within the animal. This is accomplished by placing the animal in a light-tight box and using highly sensitive, low noise charge-coupled device (CCD) cameras as shown in Figure 1.1. Mice are usually anesthetized during imaging to prevent movement, with heat provided to maintain body temperature. Two dimensional systems produce a single image of the animal surface; the bioluminescent images are overlaid on a black and white image of the animal providing additional anatomical information. These systems feature rapid image acquisition (typically on the order of a few minutes) with the ability to image multiple animals at once making them ideal for large longitudinal studies. The images are generally sufficient for visualization or semi-quantitative studies; however they do not provide truly quantitative data. Since the effects of scattering and absorption are ignored, the counts detected at the surface are not proportional to the number of cells producing the signal. Thus, a large number of cells located deep within attenuating tissue may appear identical to a smaller number located closer to the surface. Consequently, two dimensional bioluminescence images are generally useful for the study of superficial sources or longitudinal studies where only relative information is required. In order to discuss the techniques used to correct for scattering and absorption it is important to describe the interaction of light with biological tissues.

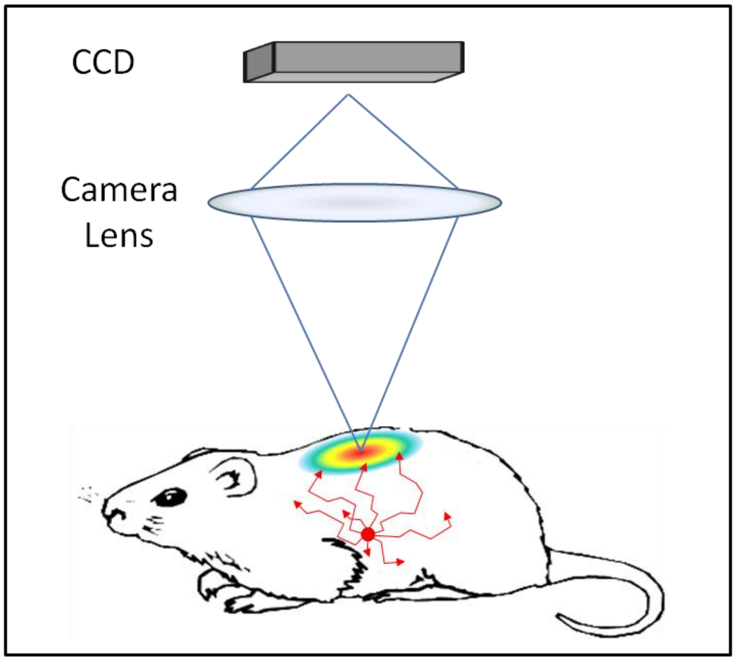

Figure 1.1. Schematic view of two dimensional planar bioluminescence imaging system. The light emitted by a bioluminescence source propagates through the animal tissue and the surface emittance is imaged on a CCD detector.

1.1.2 Tissue Optical Properties

The details of light transport in tissue and the parameters that are used to describe tissue optical properties have been discussed in detail by Cheong *et al*. (39). The pertinent concepts will be briefly discussed here. Scattering and absorption are the two main processes governing light propagation in biological tissues. In the visible and NIR range of interest in optical imaging scattering, is the dominant interaction. Scattering is caused by mismatches in refractive index at microscopic boundaries such as cell membranes and intracellular structures. The scattering properties of tissue are described by the scattering coefficient (μ_s), which is the probability of a scattering event per unit path length. The scattering phase function is used to describe the probability of a photon travelling in direction $\hat{s}$ being scattered into direction $\hat{s}'$. In randomly organized soft tissues the distribution does not depend on the original direction prior to scattering and thus is expressed as a function of angle between the incident and scattered directions.

The angular dependence of the scattering distribution is described by the anisotropy factor $g = \int_{-1}^{1} \cos\theta \cdot f(\cos\theta) \cdot d(\cos\theta)$. The limiting cases of g =1, 0, and -1, describe complete forward, isotropic, and back scattering respectively. In the visible and NIR region, tissues are strongly forward scattering. The reduced scattering coefficient is a combination of the anisotropy factor and scattering coefficient $\mu_s' = \mu_s(1-g)$, which is essentially an equivalent isotropic scattering coefficient. Typical values of μ_s range from 10 to 50 mm^{-1} at visible wavelengths, while g ranges from approximately 0.6 to 0.97 (40, 41).

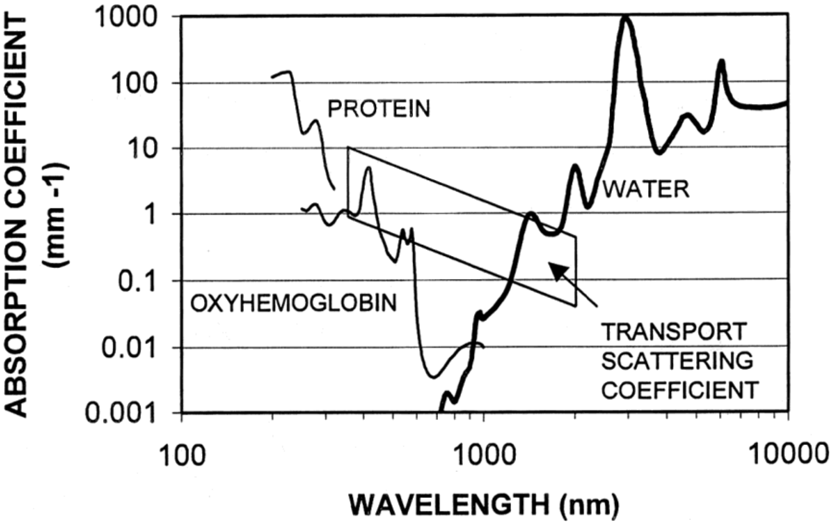

Figure 1.2. The absorption spectrum of three important tissue components; protein (bovine serum albumin, 170 mg/g), oxyhemoglobin (40 µM) and water (40 µM). The parallelogram covers reported values for the transport scattering coefficient in soft tissues (42).

Absorption is described by the absorption coefficient (μ_a), which is the probability of an absorption event per unit path length. The components of tissue that absorb light are known as chromophores, each characterized by a unique absorption spectrum. In the visible region, the main chromophore is hemoglobin (see Figure 1.2). Beyond 950 nm the absorption of water begins to increase and dominates tissue absorption. The region between 650 nm and 950 nm is known as the "optical window". The relatively low absorption in this region allows for the furthest penetration of light, and is the region that is of interest in most optical imaging modalities including bioluminescence.

1.2 Optical Tomography

By far the most common method used to correct for the attenuation of light in bioluminescence imaging involves full tomographic reconstruction of the bioluminescent sources. Other innovative techniques have been proposed including a planar imaging method incorporating video reflectometry and diffusion theory by Comsa *et al* (43), however tomographic techniques offer the greatest flexibility and are the current focus of many researchers. In optical tomography, light that is emitted from the surface of the subject is collected at multiple locations and used to reconstruct the imaging parameters of interest. In BLT the goal is to reconstruct the internal distribution of bioluminescent sources within the subject, while in DOT the goal is to recover the unknown optical properties (either absorption or scattering at each wavelength, or chromophore concentration and scattering properties from multi-wavelength data). The similarities and difference of these techniques will be discussed in the following sections.

1.2.1 Bioluminescence Tomography

The fundamental difference between bioluminescence tomography and bioluminescence imaging is the use of mathematical models of light propagation to correct for the attenuation and scattering of light in tissue. Many different techniques are employed to collect images of the surface emittance. Initially, systems employed optical fibers in contact with the subject surface, although more recently non contact methods using CCD cameras are used. The most common setup is to place the subject on a rotation state and record images of the surface fluence at multiple angles by rotating the subject (see Figure 1.3), or rotating the CCD camera around a fixed subject. Alternatively, some systems use a system of mirrors to record multiple views of the subject with no moving parts.

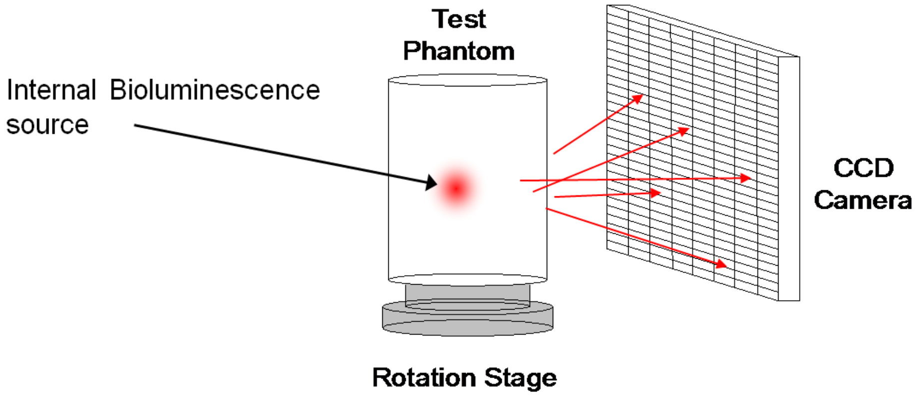

Figure 1.3. Schematic representation of a typical BLT system. The light emitted from the internal sources propagates to the surface and imaged on a CCD camera. A rotation stage is used to acquire multiple views of the subject.

Image reconstruction in BLT is considerably more complex than for bioluminescence imaging. Model based iterative reconstruction methods are composed of two main parts; a forward model of light propagation in tissue and a method to recover the internal bioluminescence distribution, often referred to as the inverse problem. The forward problem is discussed in more detail in section 1.3, which describes models of light propagation in turbid media. The inverse problem in BLT suffers from many challenges that need to be solved if accurate images are to be realized. It is highly ill-posed and underdetermined due to strong scattering and limited measurements of boundary data (16). Many different distributions of internal sources can result in similar light fluence distributions at the surface. In addition, it has been shown that measurements at a single wavelength are not adequate to obtain a unique source distribution. Lastly, there can be errors in the modeled light propagation due to uncertainty in the optical properties used in the forward model. Several methods have been proposed to overcome these limitations. Multispectral imaging and permissible source region approaches have been employed in order to alleviate the underdetermined and ill-posed inverse source problem (24-26, 44, 45). Images taken at different wavelengths of the bioluminescence spectrum increase the amount of linearly independent measurement data available for source reconstruction (44). The permissible source region approach decreases the number of possible source locations and, hence, makes the source reconstruction problem less underdetermined (26, 31, 32, 46). In addition, it has been demonstrated that correct anatomical information and heterogeneous optical property maps also result in more accurate reconstructions (25, 29, 35).

1.2.2 Diffuse Optical Tomography

Diffuse optical tomography is a non-invasive imaging technique that has been under development since the early 1990s for the detection and characterization of functional changes within biological tissue (47). DOT is typically performed at near-infrared wavelengths where the absorption of tissue is relatively low. Several applications have emerged for imaging biological tissue, including applications in breast cancer detection and characterization (48), brain functional imaging (49), as well as small animal imaging (21).

The implementation of DOT is very similar to BLT, therefore only the pertinent difference will be discussed here. Non-contact CW methods are less common then time domain and frequency domain based systems which use optical fibers placed directly in contact with the subject. Optical fiber based methods allow for simpler calibration and more reliable operation, although small animal imagers typically use non-contact, CW CCD based detection. The instrumentation in DOT is similar to the instrumentation used for BLT as seen in Figure 1.4. The primary difference is the addition of an external light source to inject light into the subject.

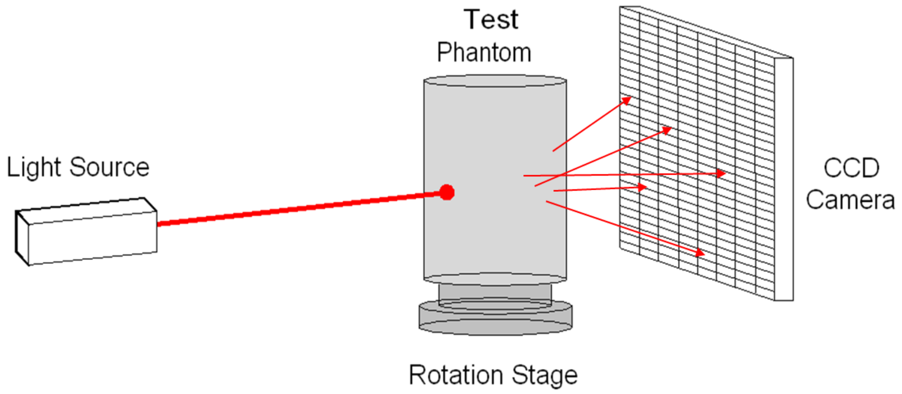

Figure 1.4. Schematic representation of a typical DOT system configured for trans-illumination imaging. A light source is used to inject light into the subject. The light propagates through the subject and the surface fluence is imaged on a CCD camera. A rotation stage is used to acquire multiple views of the subject.

The inverse reconstruction problem in DOT is very similar to BLT. It is a similarly ill-posed problem in that multiple distributions of optical properties can result in identical surface emittance. Similar to BLT, DOT benefits from the inclusion of multispectral information by using spectroscopic techniques to recover chromophore concentrations (19, 50). Perhaps the greatest improvement has been realized through the use of spatial priors from an alternative imaging technique. Structural information from other modalities such as MRI and CT has been shown to improve the stability and accuracy of the reconstructed optical property distributions by reducing the number of unknown parameters in the inverse reconstruction problem (19, 21-23). In this thesis, we used DOT to recover the internal optical property distribution to improve the subsequent BLT reconstruction. A cone beam X-ray CT system was used to provide a priori anatomical information to constrain the DOT algorithm. The DOT system is described in Chapter 4 while the X-ray CT system is covered in Chapter 2.

1.3 Models of Light Propagation in Turbid Media.

A fundamental component in almost all optical imaging techniques including tomographic methods is an accurate mathematical description of light propagation in tissue. This section will discuss several models used in optical imaging with an emphasis on those employed in DOT and BLT. These models are used to solve the “forward” problem in optical imaging, i.e., given the source distribution and optical properties, how much light reaches the external detectors?

A number of different models can be used, including stochastic, analytical and numerical. A detailed description of the models used with an emphasis on optical tomography is presented by Arridge *et al*. (51). Stochastic models involve tracking individual photon interactions. Two of the most common methods include Monte Carlo simulation (52) and random walk theory (53). Monte Carlo methods can be very accurate, and are highly adaptable and increasing popular due to the rapid increase in computing power; however accurate solutions are still too time-consuming for many applications. Analytical models are computationally fast, but suffer from the disadvantage of being limited to simple geometries with mostly homogeneous optical property distributions. Analytical solutions for various geometries have been derived and discussed by Arridge *et al.* (54). Numerical models are the most widely used methods due to their relatively short computation times and ability to model complex geometries with complex heterogeneous optical properties. A number of different numerical models have been developed and used in optical tomography including finite element (55-57), finite difference (58), finite volume (59), and boundary element(50).

1.3.1 The Radiative Transport Equation

Light propagation in tissue is described most accurately by Maxwell's electromagnetic theory or by the radiative transport equation (RTE). The first approach is very complex in biological tissues and there have been few attempts to apply this method in tissue optics (60). In radiative transport theory the propagation of light through a medium is described in terms of a conservation law that accounts for gains and losses of photons due to scattering and absorption (51). The radiative transport equation is a generalized form of the Boltzmann equation:

$$\begin{aligned}\left(\frac{1}{c}\frac{\partial}{\partial t} + \hat{s}\cdot\nabla + [\mu_a(r) + \mu_s(r)]\right) L(r,\hat{s},t) \\ = \mu_s(r)\int_{4\pi} f(\hat{s}\cdot\hat{s}')\, L(r,\hat{s}',t)d\hat{s}' + q(r,\hat{s},t)\end{aligned} \tag{1.1}$$

where $L(r,\hat{s}',t)$ is the energy radiance at all points r within the medium at time t, and unit of solid angle $\hat{s}$, c is the velocity of light in the medium, and $f(\hat{s}\cdot\hat{s}')$ is the normalized differential scattering function which describes the probability of scattering from angle $\hat{s}'$ into angle $\hat{s}$. The first term represents the change of the energy radiance with time, the second term is the net change due to energy flow, the third term represents the decrease in radiance due to absorption and scatter, the fourth term is the gain in radiance due to in-scatter from all other directions, and the fifth term describes the contributions from sources located within the medium.

The RTE it is not commonly used in biomedical optics due to the computational complexity required to achieve accurate results if the radiance is highly anisotropic (42). A number of approximations to the RTE have been proposed. The majority of these approximations are based on the diffusion approximation (DA). The DA has played a vital role in the emergence and maturation of present day biomedical optics.

1.3.2 The Diffusion Approximation

The RTE is simplified to yield the diffusion equation by making two assumptions; 1) the radiance is only linearly anisotropic and 2) the rate of change of the flux is much lower than the collision frequency. The derivation of the DA assumes that the radiance in tissue can be represented by an isotropic fluence rate, $\Phi(r,t)$, plus a small directional flux, $J(r,t)$ where:

$$\Phi(r,t) = \iint_{4\pi} L(r,\hat{s}',t) d\hat{s} \tag{1.2}$$

$$J(r,t) = \iint_{4\pi} L(r,\hat{s}',t)\hat{s} d\hat{s} \tag{1.3}$$

The radiance can be expanded into a first order set of spherical harmonics and integrated over all solid angles to give:

$$L(r,t,\hat{s}) = \frac{1}{4\pi}\Phi(r,t) + \frac{3}{4\pi}J(r,t)\cdot\hat{s} \tag{1.4}$$

Next, integrating the radiative transport equation over all angles and implementing equations 1.2 and 1.3 results in the continuity expression for the photon flux:

$$\frac{1}{c}\frac{\partial\Phi(r,t,\hat{s})}{\partial t} + \nabla\cdot J(r,t,\hat{s}) + q_0(r,t) \tag{1.5}$$

where $q_0(r,t)$ is an isotropic source term. The diffusion equation is reached by substituting Fick's Law ($J(r,t) = -\kappa(r)\nabla\Phi(r,t)$) which relates the flux to the gradient of the fluence rate into equation 1.5:

$$\frac{1}{c}\frac{\partial\Phi(r,t)}{\partial t} - \nabla\cdot\kappa(r)\nabla\cdot\Phi(r,t) = -\mu_a\Phi(r,t) + q_0(r,t) \tag{1.6}$$

where $\kappa(r)$ is the diffusion coefficient defined as $\kappa(r) = 1/3(\mu_s' + \mu_a)$. The DA can reliably calculate the fluence rate within a highly scattering medium because the radiance is dominated by the isotropic fluence rate and is only weakly anisotropic (61). The DA is valid in media where scattering interactions dominate absorption, which is the case for most biological tissues over the emission spectrum of firefly luciferase (28, 39), but it is not accurate near boundaries or sources. Hence, boundary conditions need to be implemented such that there is a good match between calculated and measure data. The DA is used in this work to simulate light transport in tissue. Details of the implementation and boundary conditions are discussed in the next section.

1.3.3 FEM Modeling – NIRFAST

In this thesis we use a free and open source software package called Near Infrared Fluorescence Absorption and Spectral Tomography (NIRFAST) to model light transport in tissue. NIRFAST is a comprehensive software package that uses finite element methods (FEM) to provide numerical solutions to the diffusion equation. It was originally developed by Dehghani *et al.* for use in NIR diffuse optical tomography (48) , but is equally well suited for modeling light propagation at shorter wavelengths provided scattering interactions dominate. In this work NIRFAST is used mainly to solve the forward model in optical tomography, however it also contains routines that make it useful for solving the inverse problem. Details on the inverse methods used in this thesis are presented in detail in Chapters 4 and 5. Here we provide a brief description of the forward model. NIRFAST produces numerical solutions to the frequency domain version of the diffusion equation:

$$-\nabla \cdot \kappa(r)\nabla\Phi(r,\omega) + \left(\mu_a(r) + \frac{i\omega}{c}\right)\Phi(r,\omega) = q_0(r,\omega) \tag{1.7}$$

where ω is the intensity modulation frequency. In this formulation the fluence is a complex field (i.e. it has both a real and imaginary component) which is then mapped to amplitude and phase. In this work only continuous wave measurements are performed using a CCD, therefore no phase data are available. The model is easily adapted to CW measurements by setting the modulation frequency to zero.

Several types of boundary conditions have been proposed to deal with model data mismatch at tissue boundaries due to changes in refractive index. Two examples are the partial-current boundary condition and the extrapolated boundary condition described by Haskell (61), and Farrell (62). The solution employed in NIRFAST is similar to the partial-current condition. The air–tissue boundary is represented by an index-mismatched Robin boundary condition (type III), in which light at the surface of the tissue exits but does not return (63). The flux leaving the external boundary is equal to the fluence rate at the boundary weighted by a factor that accounts for the internal reflection of light back into the tissue. This relationship is described in the following equation:

$$\Phi(\zeta,\omega) = 2A\hat{n}\cdot\kappa(\zeta)\Phi(\zeta,\omega) \tag{1.8}$$

where ζ is a point on the external boundary, $\hat{n}$ is the outward pointing normal, and A depends upon the relative refractive index (RI) mismatch between the tissue and air. Here, A can be derived from Fresnel's law:

$$A = \frac{2/(1-R_0) - 1 + |\cos\theta_c|^3}{1 - |\cos\theta_c|^2} \tag{1.9}$$

where $\theta_c = \sin^{-1}(1/n)$, is the angle at which total internal reflection occurs for photons moving from the region with RI of n_1 to air, and $R_0=(n_1/n_{\mathrm{air}}-1)^2/(n_1/n_{\mathrm{air}}+1)^2$.

1.4 Thesis Proposal

Small animal imaging is a valuable tool in preclinical biomedical research which relies on the use of animal models to understand the pathogenesis of human disease and to provide methods for developing and testing new therapies. The newly emerging optical imaging techniques such as bioluminescence tomography offer an inexpensive, versatile, and highly sensitive alternative to more established anatomical imaging technologies. These techniques are capable of non-invasively imaging a variety of cellular and molecular processes *in vivo* – providing unique insights into disease pathogenesis and treatment. As an emerging technology, current bioluminescence imaging methods suffer from several limitations, preventing them from reaching their full potential.

In this thesis I report how we developed and characterized an integrated multispectral BLT/DOT/X-ray CT imaging system. The system addresses many of the inherent problems encountered in planar bioluminescence imaging techniques, allowing for the recovery of more accurate and quantitative bioluminescence data. The integrated X-ray CT scanner provides anatomical information which aids in the visualization and localization of the recovered bioluminescence distributions and also helps to constrain the inverse reconstruction in the DOT system. The system accounts for the propagation of light through tissue by using the diffusion approximation to model light transport in tissue. DOT is used to recover accurate optical property distributions that are used in tomographic reconstructions of bioluminescent sources. Lastly, the BLT component makes use of multispectral emission information to constrain the BLT reconstruction resulting in more accurate recovery of sources located deep within biological tissues. Simulations and tissue-simulating test phantoms are used to characterize all stages of the imaging system. A description of the organization of the thesis is given below.

Chapter 2 describes the design and characterization of a cone beam X-ray CT scanner. The bench top X-ray CT scanner is based on a flat panel X-ray detector (FPD) coupled to a gadolinium oxysulfide scintillator, a micro-focus X-ray source and a high precision rotation stage. The imaging performance of the X-ray source and FPD is examined in detail. Also discussed are gain correction methods, system alignment techniques and contrast performance. The detector response curve was found to be non-linear at both low and high exposures. The response curve was "linearized" by using a polynomial gain correction technique involving fitting the response of the detector with a 3rd order polynomial function. The modulation transfer function of the detector was measured at approximately 8.6 cycles/mm at 10% contrast by using the angled edge technique. Contrast phantom measurements demonstrate very good low dose contrast for soft tissue and bone, however soft tissue contrast is limited. Contrast-to-noise ratio measurements show that the CT scanner performance is quantum noise limited.

Chapter 3 describes the fabrication and characterization of the tissue-simulating phantoms that were used during the development of the bioluminescence tomography system. The optical properties of liquid and solid epoxy-based phantoms are investigated by measurements on a steady-state spatially resolved diffuse reflectance system (64). Several dyes were examined for their ability to mimic the absorption properties of tissue over the emission spectrum of luciferase (500–700 nm). The long term stability of the solid epoxy phantoms was also investigated. The solid epoxy phantoms required a few days to fabricate and machine and were stable after an initial curing period of 3 months.

Chapter 4 describes the construction and characterization of an integrated DOT/X-ray CT system. The DOT system uses a non-contact CCD camera to acquire surface fluence measurements, and a finite element model of the propagation of light in tissue to recover the internal optical property distribution of a test subject. *A priori* spatial information from the X-ray CT is used to constrain the DOT reconstruction algorithm. A set of simulations is used to determine the optimal source detector geometry for the DOT system. Four image reconstruction algorithms are evaluated for their ability to recover the effective attenuation coefficient of a series of test phantoms. Two of the algorithms (a modified LM method, and a repeated single-step Tikhonov method) does not use any *a priori* spatial information. Two other algorithms (hard priors and soft priors) use *a priori* structural information to constrain the reconstruction process. A spectrally constrained algorithm is also described that is useful for multi-wavelength reconstructions. The results indicate that the inclusion of spatial priors improves the reconstructed image quality dramatically. The hard priors and soft priors methods result in similar recovered optical property distributions, but the soft priors case is more resilient to imperfect *a priori* information. The spectrally constrained algorithm is successful at removing the fluctuations in reconstructed scattering properties of non-spectrally constrained methods.

Chapter 5 describes the performance of the whole integrated imaging system. The integrated BLT system uses a non-contact CCD camera to acquire surface emittance measurements and a reconstruction algorithm based on an FEM model of light propagation to recover the internal distribution of bioluminescence. The accuracy of the proposed bioluminescence reconstruction algorithm is demonstrated and validated using simulated and experimental data. The non-uniqueness of the BLT reconstruction problem is shown using simulations at single wavelengths. Multispectral measurements are shown to provide an accurate method for estimating the depth of a bioluminescence source due to the wavelength dependent attenuation of tissue. The spatial resolution of the BLT algorithm is demonstrated down to a source separation of 1.5 mm. Experimental measurements are been presented which explore the importance of accurate estimates of background optical properties in BLT. Five methods are examined for incorporating background optical properties into the BLT. The hard spatial prior method is found to provide the best overall recovery of total source strength, position, and fidelity at all source depths up to 12.5 mm. The total source strength is recovered to within 8 %, while the source position is recovered to within 0.16 mm. No significant depth dependence is found using either method up to a depth of 12.5 mm.

Chapter 6 summarizes the results of this thesis and recommends possible future direction of research.

Chapter 2

X-ray Computed Tomography Design and Characterization

In this chapter I describe the design and characterization of a cone beam X-ray computed tomography (CBCT) scanner. The X-ray CT scanner is an important component in the development of the integrated bioluminescence tomography system. The X-ray CT system provides both surface contour information and internal structural information on the subject. Surface contour information is used for generating accurate FEM meshes used in both DOT and BLT reconstructions. The internal structural information is valuable during reconstruction of the internal optical properties of the subject with DOT. The main goal was to design an inexpensive X-ray CT scanner that could be integrated into the bioluminescence tomography system without modification.

2.1 Cone Beam X-ray CT Design

2.1.1 Instrumentation

A schematic diagram of the CBCT scanner is shown in Figure 2.1. The prototype CBCT scanner consists of a small air-cooled microfocus X-ray source, a flat-panel CMOS (complementary metal-oxide semiconductor) X-ray detector, a motorized rotation stage and a personal computer (PC). The components are mounted on an optical bench inside a lead-lined enclosure and operated from the PC. The enclosure is fitted with interlock switches and warning lights to prevent any accidental exposure to radiation. The system is designed to acquire data in a cone beam geometry. The X-ray detector and the rotation stage are mounted on a rail system to allow for changes in the source-to-object distance (SOD) and the source-to-detector distance (SDD) as needed. The SOD and SDD determine the imaging parameters such as the magnification ratio, cone beam angles (ϕ_1, ϕ_2), and the field of view.

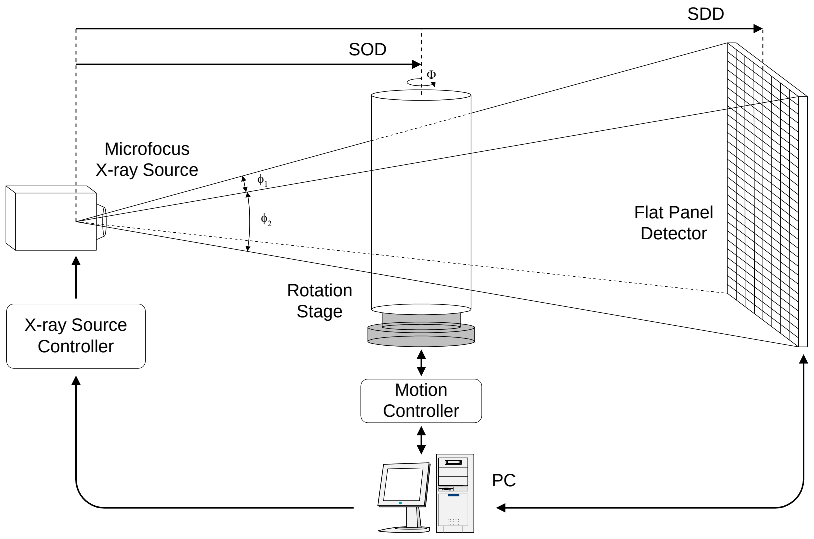

Figure 2.1. Schematic diagram of the CBCT system. The microfocus X-ray source irradiates a subject on the rotation stage, and 2D projections are acquired on the flat panel detector. The personal computer (PC) controls the data acquisition, varying the integration time and rotation angle as needed. The source-to-detector distance (SDD) and the source-to-object distance (SOD) determine the cone beam angles (ϕ_1, ϕ_2), the magnification ratio, and the field of view.

The microfocus X-ray source (PXS5-926EA, Thermo Electron Corp.) consists of a sealed X-ray tube and a high voltage power supply in a single enclosure. The X-ray tube has a fixed tungsten anode having an anode angle of 45 degrees to the electron beam with a 127 µm thick beryllium window, and the focal spot size is 5 µm. X-rays are emitted in a cone with its apex located at the focal spot, at a 45 degree cone angle. The source has a maximum tube voltage of 90 kVp and maximum power of 8 W. A 1 mm thick aluminum filter has been added to the X-ray source to absorb the low energy X-rays emitted by the source and thus reduce the radiation dose to the subject. All functions of the source are controlled by an X-ray controller which monitors the tube voltage and current as well as the interlock switches.

The flat-panel CMOS X-ray detector (Shad-o-Box 2048, Rad-icon Imaging Corp.) consists of a 2D photodiode array coupled to a gadolinium oxysulfide (Gd_2O_2S) scintillator screen (Min-R 2190, Kodak). The photodiode array has a detection area of 98.6 mm x 49.2 mm and contains 1024 x 2048 pixels with a 48 µm pixel pitch. The Gd_2O_2S scintillator screen converts the incoming X-rays into visible photons (510 nm) which are then converted into electrical charges in the photodiode array. The analog signal from the photodiodes is then digitized to 12-bit resolution at a maximum frame rate of 2.7 frames per second.

A motorized rotation stage (URM100, Newport Corp.) serves as the subject holder. The rotation stage rotates the subject during imaging and is controlled by the PC. It has an angular precision of 0.01 degrees.

2.1.2 Data Acquisition

The CBCT scanner is controlled by a PC which is also used for data processing. The microfocus X-ray source and rotation stage are interfaced to the computer via their respective controllers through a serial port connection to the PC. The flat panel detector (FPD) is run by a digital frame grabber board (PXD1000, CyberOptics Corp.) installed in the PC. A user interface for data acquisition, display, and storage was created in LABVIEW graphical programming language (National Instruments Corp.). The user interface allows for control of all important imaging parameters including X-ray tube current and voltage, FPD frame exposure time, rotation stage motion and projection number.

Two data acquisition modes have been programmed for CT data collection. In the first mode the rotation stage rotates at a constant angular velocity and the frame grabber is run in continuous mode, acquiring projections at fixed time intervals. The second is a “step and shoot” approach where the rotation stage is kept stationary during irradiation and FPD readout and is rotated between projections. The “step and shoot” method has a number of advantages. Since the rotation stage is stationery during frame exposure, there is no blurring of the projection images as would occur in the continuously rotating case. It is also easier to measure the position of the rotation stage with high accuracy. A major disadvantage, however, is a longer scan time and an increase in total dose to the subject as data are not collected continuously.

2.1.3 Image Reconstruction

Image reconstruction for the CBCT scanner is handled by commercially available reconstruction software (COBRA, Exxim Computing Corp.). The software employs a filtered back-projection algorithm (Feldkamp, (65)) for 3D reconstructions that is both highly customizable and computationally efficient. A typical 512^3 volume with 360 input projections of 1024 x 2048 pixels each requires approximately 3 minutes for reconstruction on a single CPU personal computer (P4 3.6 Ghz, Intel Corp.).

2.2 X-ray Source Characterization

The X-ray flux of the microfocus X-ray source was measured using a pre-calibrated Farmer dosimeter with a 0.6 cc ionization chamber (Nuclear Associates). Exposures were measured from 5 to 30 cm from the source end window at tube voltages of 20, 30, 40, 60, and 80 kVp at a tube current of 100 μA with no additional filtering (Figure 2.2). The measured exposures follow the inverse-square law as is expected. Measurements were also performed with a 1 mm aluminum filter. The exposure rates measured from 20 to 80 kVp are shown in Figure 2.3, with and without the filter, at a distance of 5 cm from the tube end window. The dose rate decreases significantly when the 1 mm aluminum filter is used. This is important for small animal imaging, as the aluminum filter absorbs much of the X-ray spectrum below 15 keV. While these X-rays would offer enhanced soft tissue contrast, removing them decreases the dose to the subject significantly (66). The exposures and doses reported in the work that follows are based on these measurements.

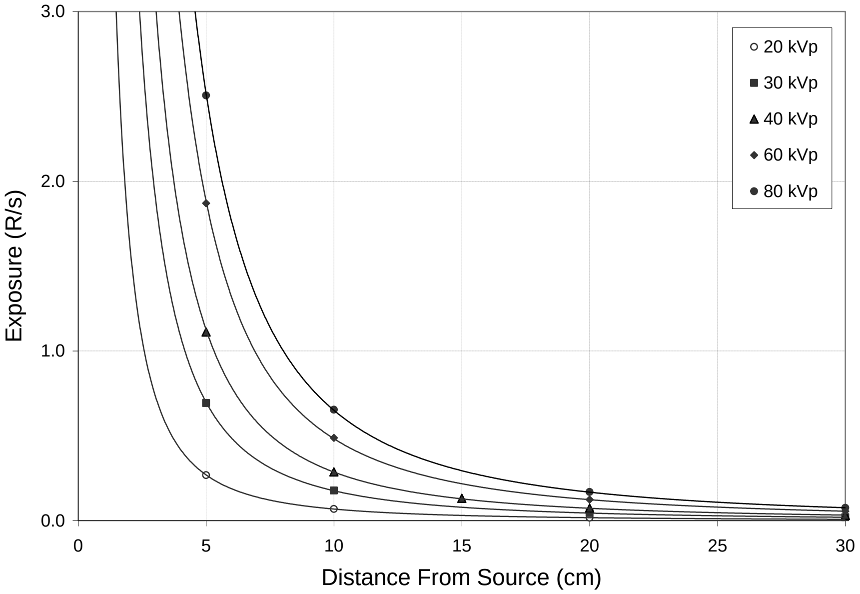

Figure 2.2. X-ray source dose rate as a function of distance from the source end window. Radiation dose was measured using a pre-calibrated Farmer dosimeter.

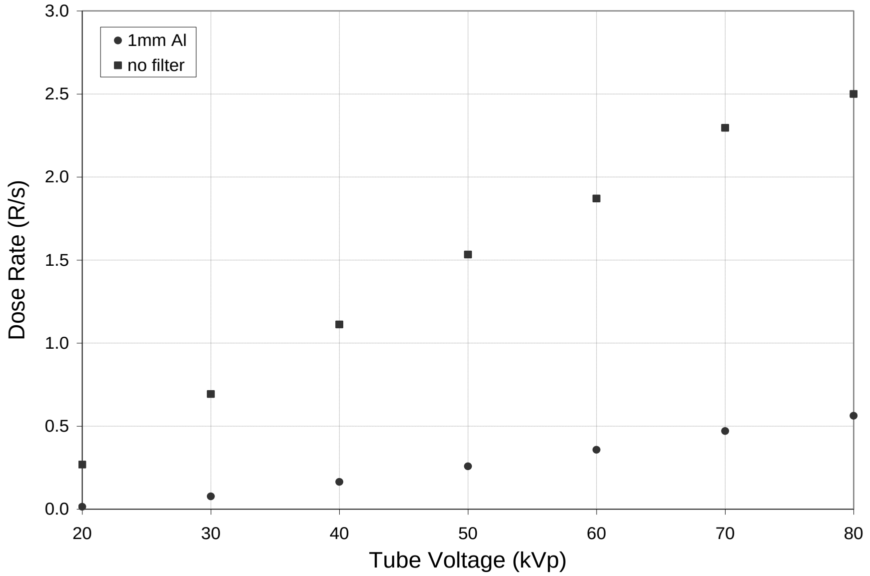

Figure 2.3. X-ray source dose rate with and without aluminum filtering at a tube current of 100 μA and distance of 5 cm from the source.

The linearity of the X-ray source output with tube current was examined (Figure 2.4). The exposure rate was linear over the entire operating range of the X-ray tube from 0 to 178 μA. This is important because this allows the doses and exposures for subsequent experiments to be calculated using tube current, exposure time and the set of ion chamber measurements made previously. X-ray tube stability, as reported by the manufacturer is ± 2.5 % over a period of 24 h. Additional exposure measurements still need to be performed periodically to determine if there are any changes in X-ray flux throughout the lifetime of the X-ray source.

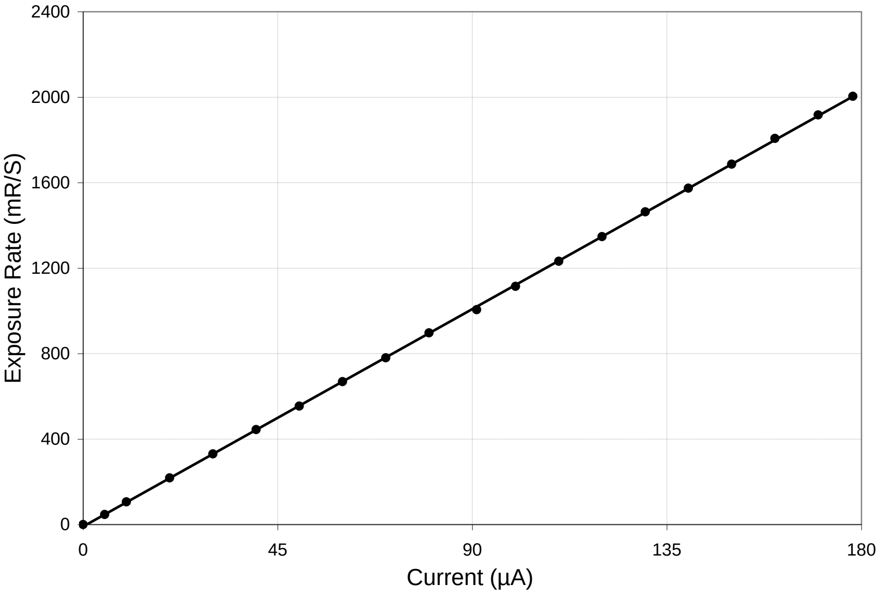

Figure 2.4. X-ray source linearity.

2.3 Flat Panel X-ray Detector Characterization

2.3.1 Temporal Stability

The characterization of the FPD was begun by examining the temporal stability of the dark current signal. This was done by operating the FPD in the absence of any X-ray signal and reading the pixel signal as a function of time. The FPD was left unpowered overnight prior to each measurement. Measurements began at time t = 0, corresponding to the time power was supplied to the FPD. Data were recorded at frame times ranging from 0.4 to 6.7 seconds, and the internal temperature of the FPD was monitored using a thermocouple. The average dark signal value for each frame was calculated from an average of a 10 x 10 pixel region at the center of each of the four detector panels.

The plot of dark current signal as a function of time is shown in Figure 2.5. The trend in the dark signal is seen to be very similar for all frame times. The dark signal exhibits an initial decrease, followed by a gradual increase beyond startup levels before stabilizing. The observed trend can be at least partially correlated with an increase in the temperature inside of the FPD enclosure (Figure 2.6). Starting from an ambient temperature of ~ 23 °C, the FPDs internal temperature increases quickly after power is applied, rising to a maximum temperature of 30 °C before stabilizing. The rise in temperature and subsequent stabilization matches well with the corresponding rise in dark current signal observed in Figure 2.5. The effect of temperature on dark signal is not unexpected as dark current noise is known to increase with temperature.

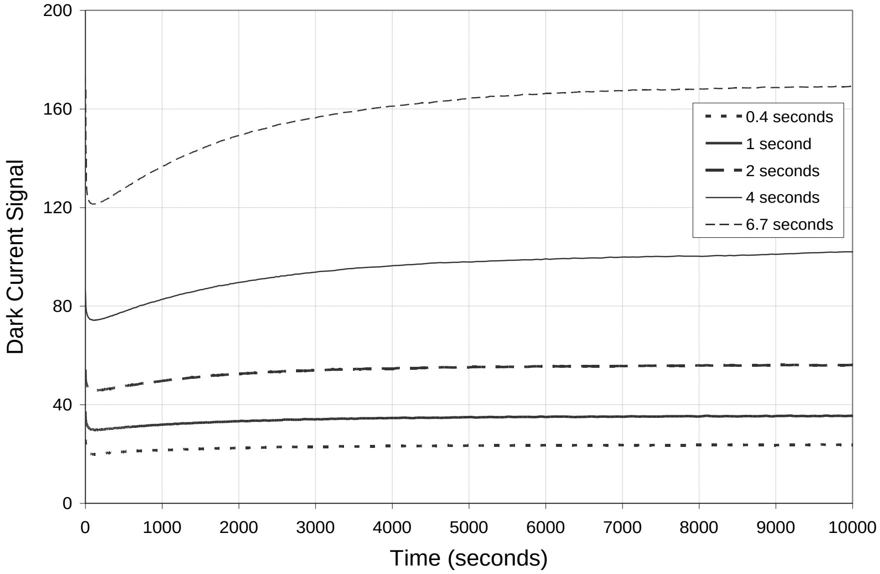

Figure 2.5. Temporal stability of the FPD dark current signal. The dark signal was measured for a period of 10000 seconds after initial power up of the detector. Data are shown for frame times ranging from 0.4 to 6.7 seconds.

The dark current signal can be easily subtracted from images using gain correction techniques provided that it remains stable during the imaging period. The removal of the dark current signal is an important step during data acquisition as the dark current signal makes up a significant portion of the detector response. In addition, the dark current increases significantly during the life of the detector due to X-ray damage from cumulative exposure (67). Based on the data shown, the FPD should be allowed to "warm up" for approximately 2 hours before any images are collected.

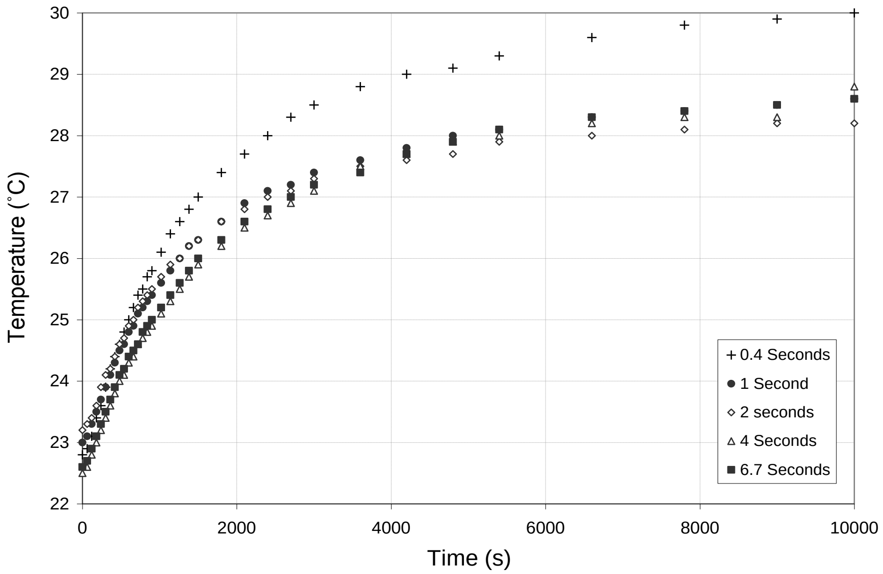

Figure 2.6. FPD internal temperature vs. time for each dark current measurement in Figure 2.5.

2.3.2 Dose Response

The FPD dose response curve was measured within an exposure range of 5 – 145 mR at a tube voltage of 50 kVp and SDD of 400 mm (Figure 2.7). For exposures above 40 mR, the FPD frame time was kept constant at 3 seconds, and the tube current was progressively increased to obtain the desired frame exposure. Exposures below 40 mR were obtained by fixing the tube current at 40 µA and decreasing the FPD frame time. The detector signal at each exposure was estimated by averaging the pixel signal over a 10 x 10 pixel region in the center of the detector after offset subtraction. The response curve was quadratic at low exposures, linear at medium exposures, with a slight roll-off at high exposures as the FPD nears saturation. This behavior is typical for a detector based on CMOS active pixel sensors. The sensor measures a change in voltage corresponding to the signal charge at the pixel by using a source-follower FET (field effect transistor), which causes any non-linearity in the amplifier transfer curve to be superimposed onto gain response of the detector (68).

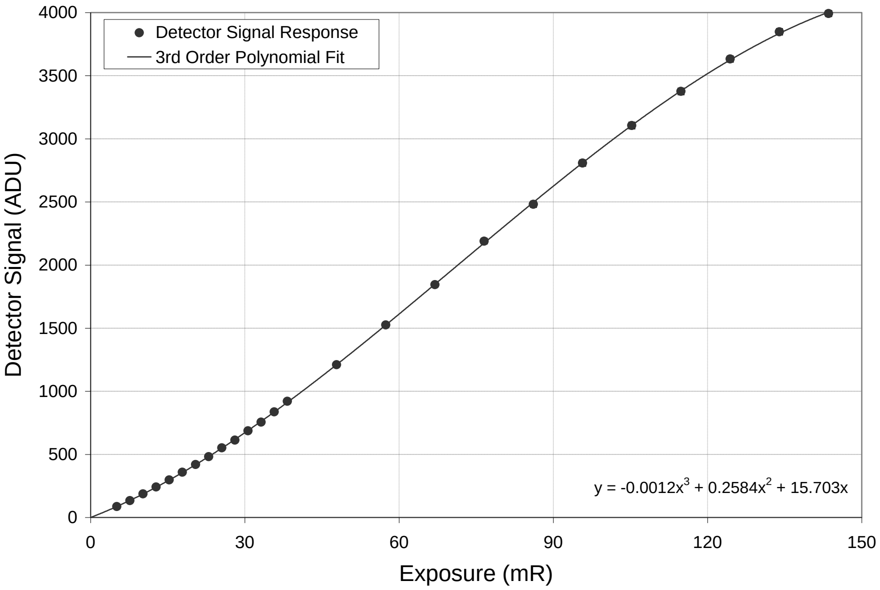

Figure 2.7. FPD response curve at 50 kVp and SDD = 400 mm. The response is non-linear. A 3rd order polynomial provides a good fit.

2.3.3 Gain Correction

Typical correction methods for digital image sensors employ a dark offset image and a flat field image to correct for variations in pixel to pixel sensitivity. The standard equation for such methods is:

$$I_C = \frac{I_{Raw} - I_{Offset}}{I_{Gain} - I_{Offset}} \times Avg\left(I_{Gain} - I_{Offset}\right) \tag{2.1}$$

where I_{Raw} is the uncorrected image, I_{Offset} is a “dark” image taken in the absence of X-rays, I_{Gain} is a uniformly irradiated frame, and I_C is the resulting corrected image. This first order correction works well for detectors with a linear response curve where only changes in the slope of the curve need to be corrected; however more sophisticated correction methods are needed for non-linear response curves. A 3rd order polynomial was a very good approximation of the response curve over the dynamic range of the detector, and was used to “linearize” the curve (Figure 2.8).

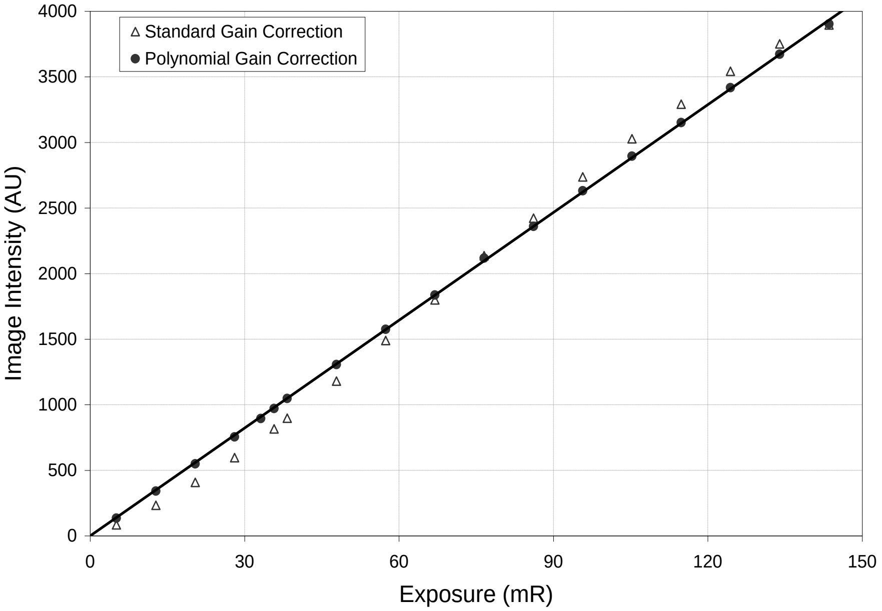

Figure 2.8. X-ray detector response curves after flat field correction and 3rd order polynomial gain correction.

The response of each pixel in the FPD using the 3rd order method is given by:

$$y_i = a_i x^3 + b_i x^2 + c_i x \tag{2.2}$$

where y_i is the response of the *i*th pixel and x is the input signal. The coefficients of the polynomial are determined for each pixel by acquiring at least four flat field images at four different exposures spanning the dynamic range of the FPD, and then calculating a least-squares cubic fit through the flat-field values (after offset correction) for each pixel. The ideal linearized pixel response is then approximated by setting y_i equal to the pixel signal in the uncorrected image (after offset correction) and solving the equation for x.

Disadvantages of this technique include an increase in calibration time due to the need to acquire at least 4 flat field exposures, as well as an increase in computation time required to fit the response curve for each pixel. Care must also be taken to ensure that the range of flat field images matches the range of exposure in the raw images, as extrapolation with polynomial functions could lead to irregular results. It should be noted that although this method is more prone to errors from dark current drift and inaccurate exposure control, noise was not significantly increased over 1st order correction methods, remaining smaller then the data points in Figure 2.8. Besides "linearizing" the FPD response curve this method also reduced the small gain variations between detector tiles called "tiling effect" inherent in tiled image sensors.

2.3.4 Spatial Resolution

The spatial resolution of the FPD was evaluated by determining the modulation transfer function (MTF). The MTF was measured using the angled edge technique as used by Samei *et al* (69). A thin stainless steel ruler (thickness of 0.4 mm), was imaged at the center of the detector at an angle of 0.60 ± 0.01 degrees at a tube current of 50 kVp. The angle of the ruler was determined by converting the grayscale image of the ruler to a binary image and performing a gradient operation to get a binary image of the edge transition. A Hough transform was then performed yielding the angle of the edge. The edge spread function (ESF) was then obtained by re-projecting the grayscale data of the original image along the direction of the estimated angle, resulting in a one-dimensional array of non-uniformly spaced discrete samples of the ESF. Following re-projection, the ESF data was re-binned into sub-pixel elements of width 4.8 μm (10 % of the pixel pitch) and smoothed using a Gaussian filter (Figure 2.9). The MTF was then obtained by taking the Fourier transform of the line spread function (LSF) which is the derivative of the ESF:

$$MTF(f) = FT\left[\frac{d}{dx}\left[ESF(x)\right]\right] \tag{2.3}$$

The resulting MTF is shown in Figure 2.10. The spatial frequency measured at 10 % MTF was approximately 8.6 cycles/mm. This value compares well with previous results published for this detector-scintillator combination (68, 70).

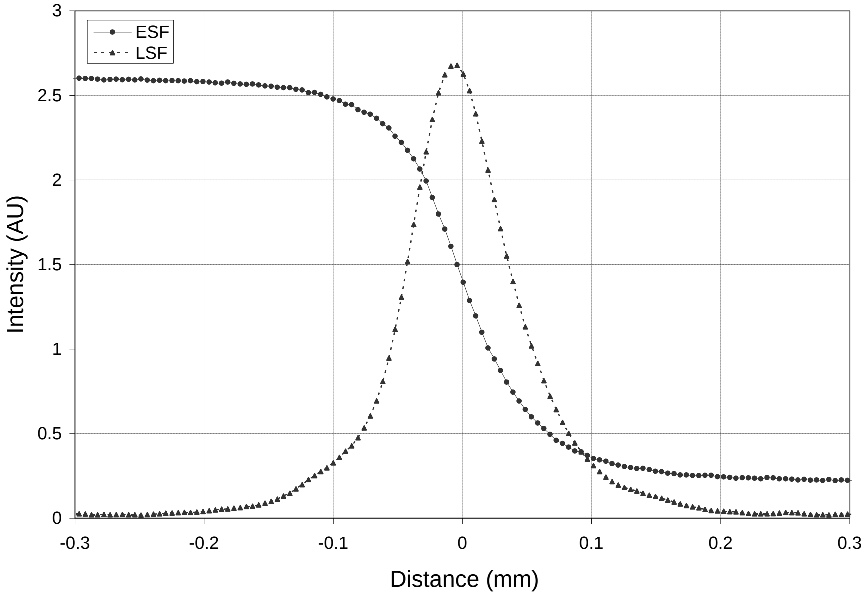

Figure 2.9. Edge spread function and line spread function obtained by re-projecting the image data along the edge direction and re-sampling to 0.1 sub pixel bins.

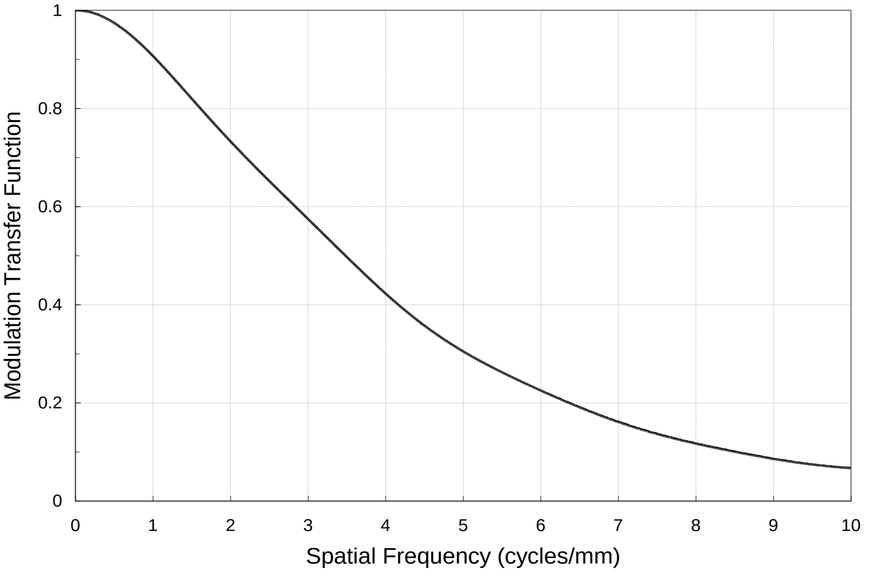

Figure 2.10. The MTF obtained from image of edge.

2.3.5 Noise Power Spectrum

The noise power spectrum (NPS) and detective quantum efficiency (DQE) of the FPD were measured using a technique similar to Dobbins *et al*. (71). The NPS was obtained by Fourier analysis of uniformly exposed images. Images were acquired under the same conditions as those used for the MTF measurements (50 kVp, 400 mm SDD). Eight consecutive images were taken at an exposure of 41 mR (3 second frame time, 120 μA) and gain correction was applied. The images were then split into four groups with two consecutive images in each and subtraction was performed. This was done to remove any background trends in the images which would distort the resulting NPS. Doing this caused the noise variances of the two images to add, so the resulting NPS was scaled by a factor of two. A 512 x 512 pixel region from the center of each image was then subdivided into smaller ROIs of 128 x 128 pixels each, resulting in a total of 64 regions.

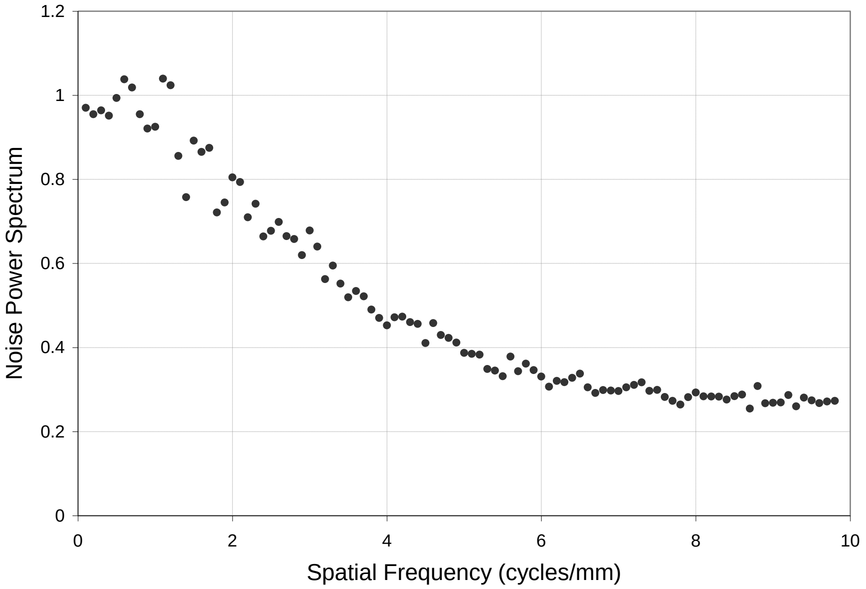

Figure 2.11. Noise power spectrum for the FPD measured at 50 kVp.

A 2D Fourier transform was applied to each region and the resulting spectra were averaged to obtain the overall 2D NPS. The 1D NPS was then obtained by averaging ± 4 horizontal lines of the 2D NPS (excluding the central axes) and is shown in Figure 2.11. The final formula for computing the normalized NPS is:

$$NPS(u,v) = \frac{\left\langle \left| FT(u,v) \right|^2 \right\rangle}{N_x N_y} \Delta_x \Delta_y \tag{2.4}$$

where $\left\langle \left| FT(u,v) \right|^2 \right\rangle$ is the average NPS from the 64 ROIs, N_x and N_y are the number of elements in the discrete Fourier transforms, and Δ_x and Δ_y are the pixel sizes in the x and y directions. When using this normalization method, the integral of the 2D NPS should be the same as the RMS variance of the pixel values in the image – this condition was verified for each ROI.

2.3.6 Detective Quantum Efficiency

The frequency dependent DQE was determined from the previously measured MTF and NPS according to the following formula:

$$DQE(f) = \frac{S^2 \times MTF(f)^2}{\Phi \times NPS(f)} \tag{2.5}$$

where MTF(f) is the measured pre-sampled modulation transfer function, NPS(f) is the measured noise power spectrum, S is the average signal from the image used to calculate the NPS, and Φ is the X-ray quantum flux incident on each detector pixel. The X-ray quantum flux was determined by simulating the output spectrum of the X-ray tube using a program called XCOMP5 (R. Nowotny, Inst. Biomed. Technik & Physik, University of Vienna, Austria). XCOMP5 allowed for the adjustment of absorbing materials in the X-ray path as well as anode angle of the tungsten target. The magnitude of the resulting quantum flux was then calibrated against exposure measurements made using a Farmer dosimeter. The final quantum flux was calculated to be 2990 photons/pixel/s. The resulting DQE is shown in Figure 2.12. The DQE of the FPD was approximately 0.45 at zero frequency. The results are comparable to the DQE measurements reported by the manufacture for this detector – screen combination (72).

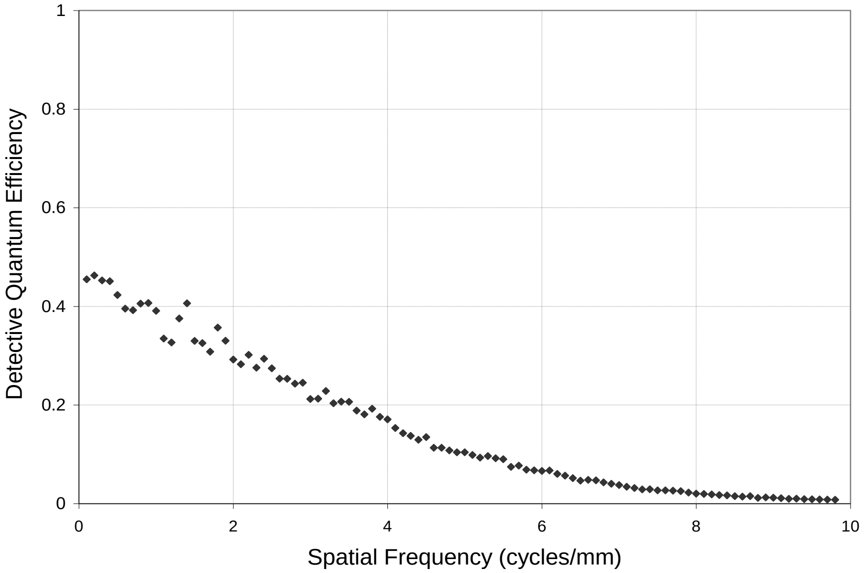

Figure 2.12. Detective quantum efficiency of FPD at an energy of 50 kVp.

2.4 X-ray CT Characterization

2.4.1 System Alignment

Image quality in computed tomography critically depends on the precise knowledge of the scan geometry of the acquisition system. In CBCT, using inaccurate parameters can result in severe image artifacts (73, 74). Since sufficiently accurate physical alignment of all imaging components is not always possible, calibration methods can be used to account for potential misalignments in scanner geometry. A calibration method developed by Noo *et al*. (75) was used for the calibration of the CBCT scanner.

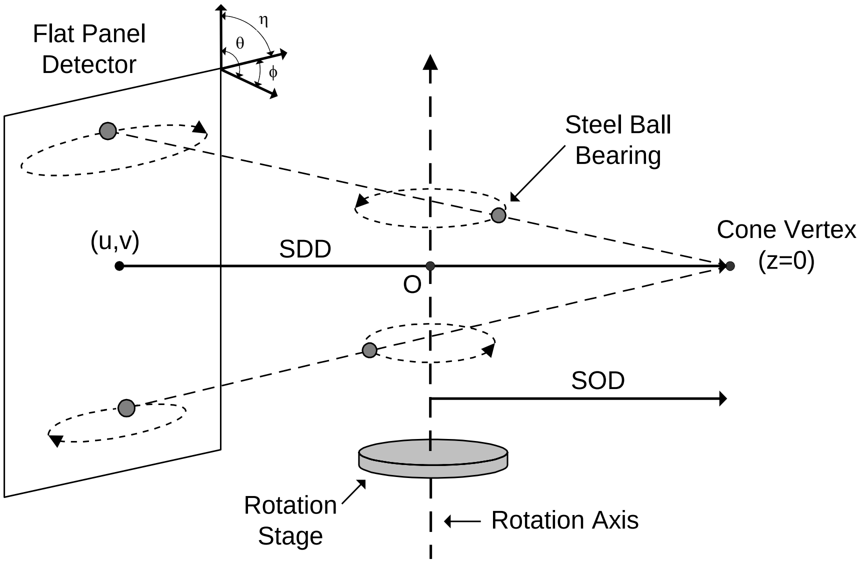

Figure 2.13. Diagram illustrating the scanner geometry and calibration phantom used for the calibration of the CBCT scanner. 2D projections of two point objects (stainless steel ball bearings) are used to calibrate the scanner. Each point object traces out an ellipse in the detector plane. Also shown are the seven parameters estimated during calibration – SOD, SDD, u, v, φ, θ and η.

The CBCT scanner is used to collect 12 projections of a calibration phantom consisting of two small stainless steel ball bearings (BBs). The projections are uniformly spaced over 360 degrees. Each BB traces out an ellipse in the detector plane during image acquisition. An illustration of the calibration phantom, imaging geometry, and calibration parameters is shown in Figure 2.13. Seven parameters are sufficient to calibrate the CBCT scanner in a circular scan geometry. These parameters are SOD, SDD, u, v, θ, φ, and η. The SOD is the distance from the cone vertex to the rotation axis (this line defines the vertex position as (SOD, 0, 0). SDD is the shortest distance from the vertex to the detector plane. The orthogonal projection of the cone vertex onto the detector plane is found at the point (u, v). The parameters θ, φ, and η describe the orientation of the FPD where θ is the tilt, φ is the slant and η is the skew of the FPD.

The projection data are used to determine the equation of the ellipses traced out by the two BBs. The ellipse equations, together with knowledge of the distance separating the two BBs, provide sufficient information to determine the calibration parameters. The calibration parameters are then entered into the reconstruction software during image reconstruction, eliminating any artifacts due to scanner misalignment.

2.4.2 Contrast Phantom

A contrast phantom has been created to examine the low contrast performance of the system (Figure 2.14). The phantom consists of eight plastic inserts with a diameter of 4 mm, whose physical densities are similar that of various soft tissues and bone. The inserts are immersed in a water bath made of a 28.6 mm diameter acrylic cylinder. The properties of the 8 inserts are shown in Table 1.1. The phantom was imaged at various doses at a tube voltage of 40 kVp, with 1 mm Al filtration. 360 projections were acquired over an angle of 360 degrees using a “step and shoot” data collection method. The SOD was set to 113 mm and the SDD was set to 162 mm.

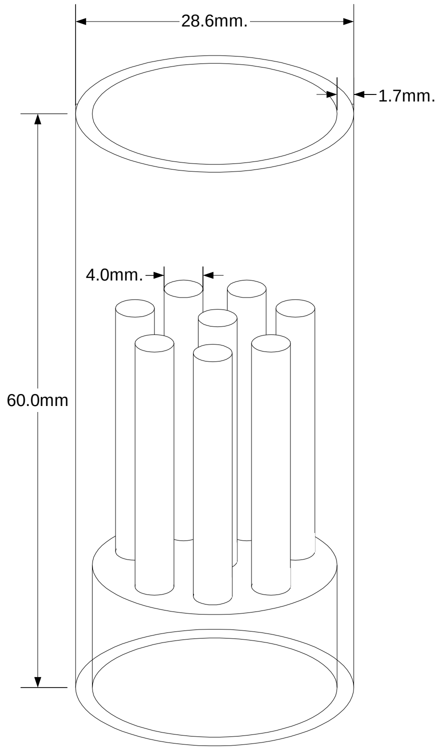

Figure 2.14. Schematic diagram of the contrast phantom. The phantom consists of an acrylic cylinder containing 8 plastic inserts. The physical properties of the inserts are shown in Table 1.1.

Table 1.1. Properties of plastic inserts used in the contrast phantom at 40 kVp. The densities are in units of g/cm^3, μ are the linear X-ray attenuation coefficients calculated from a NIST database (76), and the CT #'s are calculated from the linear X-ray attenuation coefficient attenuation coefficients.

Index	Material	Density	μ	CT #
E	Polyethylene (Low D)	0.91	0.207	-228.4
A	Polyethylene (High D)	0.96	0.218	-186.0
H	Polystyrene	1.05	0.229	-145.7
D	Acrylic	1.18	0.277	33.5
B	Polycarbonate	1.2	0.318	185.2
C	Nylon	1.14	0.302	124.7
G	Delrin	1.42	0.473	762.7
F	Teflon	2.14	1.194	3450

Figure 2.15 shows axial images of the contrast phantom at doses of 284, 142, 71 and 36 mGy. The data are presented as images of the linear X-ray attenuation coefficient and have not been converted into CT numbers. The noise increases as the dose is reduced and was found to be proportional to the square root of the dose delivered. The increasing noise makes it harder to distinguish some of the low contrast inserts below 71 mGy. In the 284 mGy image the acrylic insert, with a CT number of 33.5, is visible (as is the cylinder wall, also made of acrylic) but cannot be seen in the lowest dose image of 36 mGy.

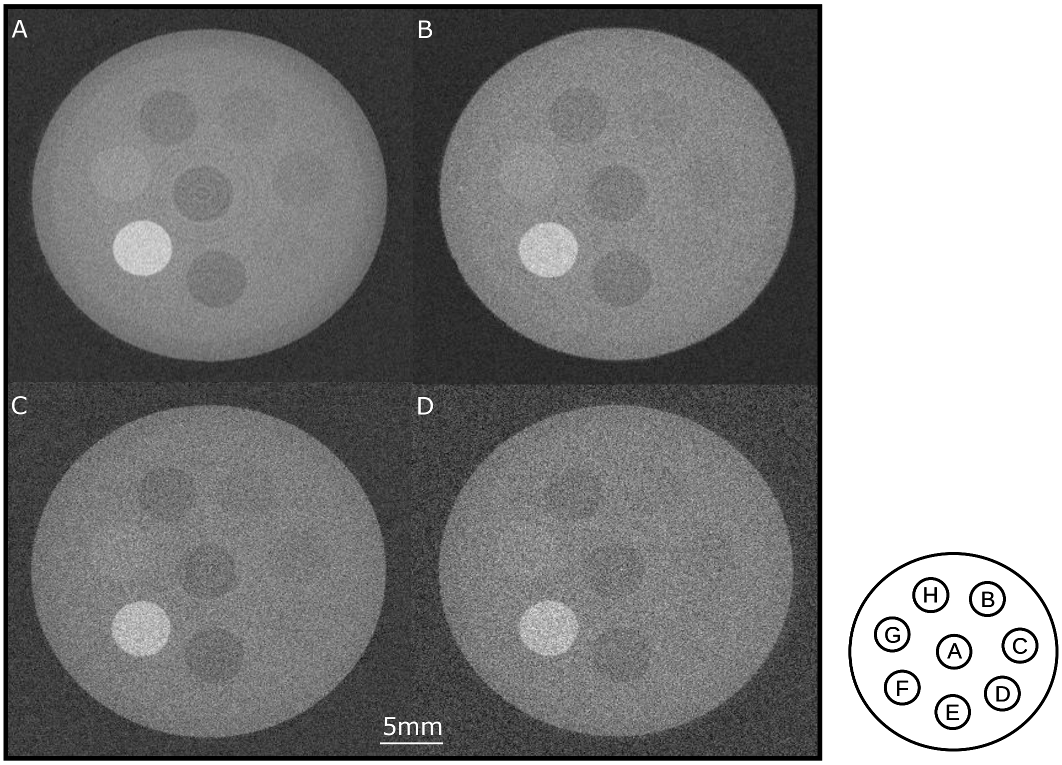

Figure 2.15. Axial images of the contrast phantom measured with doses of (a) 284mGy, (b) 142mGy, (c) 71mGy and (d) 36mGy. Each image is 512 x 512 pixels with a voxel size of 100 x 100 x 200μm.

2.4.3 Contrast-to-Noise Ratio

The noise in CT images is primarily due to the quantum noise inherent in photon detection and electronic noise in the projection data. Electronic noise is relatively constant, however quantum noise is related, in theory, to the number of photons counted, N and is inversely proportional to $\sqrt{N}$. The noise properties of the reconstructed contrast phantom images were evaluated by finding the contrast-to-noise ratio (CNR). The CNR is frequently used to characterize both the signal and noise properties of CT images and is defined as absolute contrast related to noise:

$$CNR = \frac{A - B}{\sqrt{\sigma_A^2 + \sigma_B^2}} \tag{2.6}$$

where A and B are the linear attenuation coefficients in contrast and background areas of the reconstructed CT image, while σ_A and σ_B are the corresponding standard deviations. The CNR is plotted as a function of total dose in Figure 2.16. The CNR was evaluated for two contrast regions; Teflon and low density polyethylene, over a 15 x 15 pixel region for both the contrast and background regions. The regression lines confirm that the CNR behaves as expected according to theory, where image noise is inversely proportional to $\sqrt{N}$.

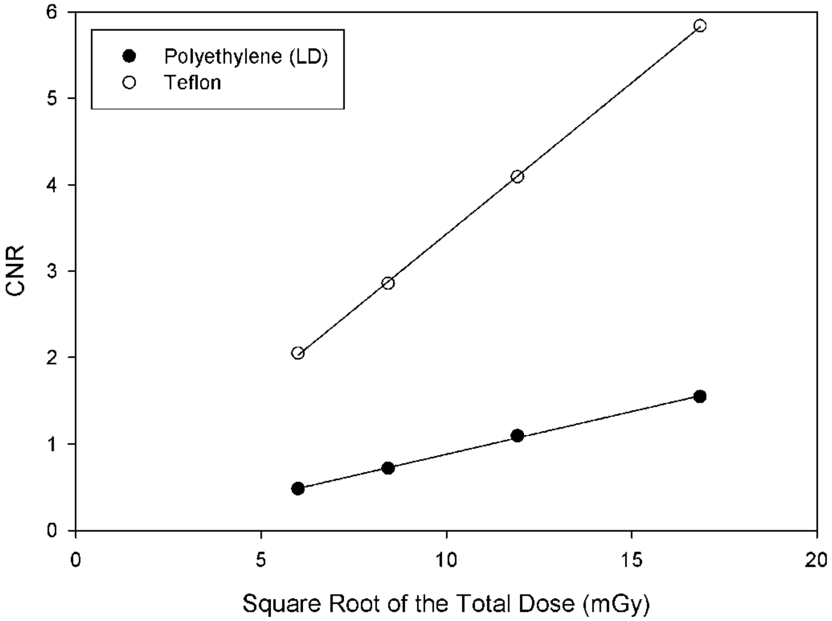

Figure 2.16. The contrast-to-noise ratio of the reconstructed contrast phantom images plotted versus total dose.

2.5 Anatomical Imaging

The overall perforamce of the CBCT scanner is demonstrated in Figure 2.17 with an axial image and 3D volume reconstruction of a postmortem mouse, as well as a sagital cross section of an *ex vivo* pig vertabra. These mouse images were acquired with the same acquisition parameters as the contrast phantom, but with a dose of 230 mGy. The images show great contrast between soft tissue and bone, however contrast between different soft tissues is very poor. Further optimization of the imaging parameters (total dose, source voltage, filtering) may yield some improvents in this area. The pig vertabrae image was acquired with similar acquisition parameters, but reconstructed on a finer grid of 80 x 80 x 100 µm. The fine structure of the trabecular bone is clearly visible in this image as is some residual soft tissue surrounding the bone. Some image artifacts are present in both images (as well as the contrast phatom images in Figure 2.15). Ring artifacts can be seen in both cases and streak artifacts can be observed in the mouse images.

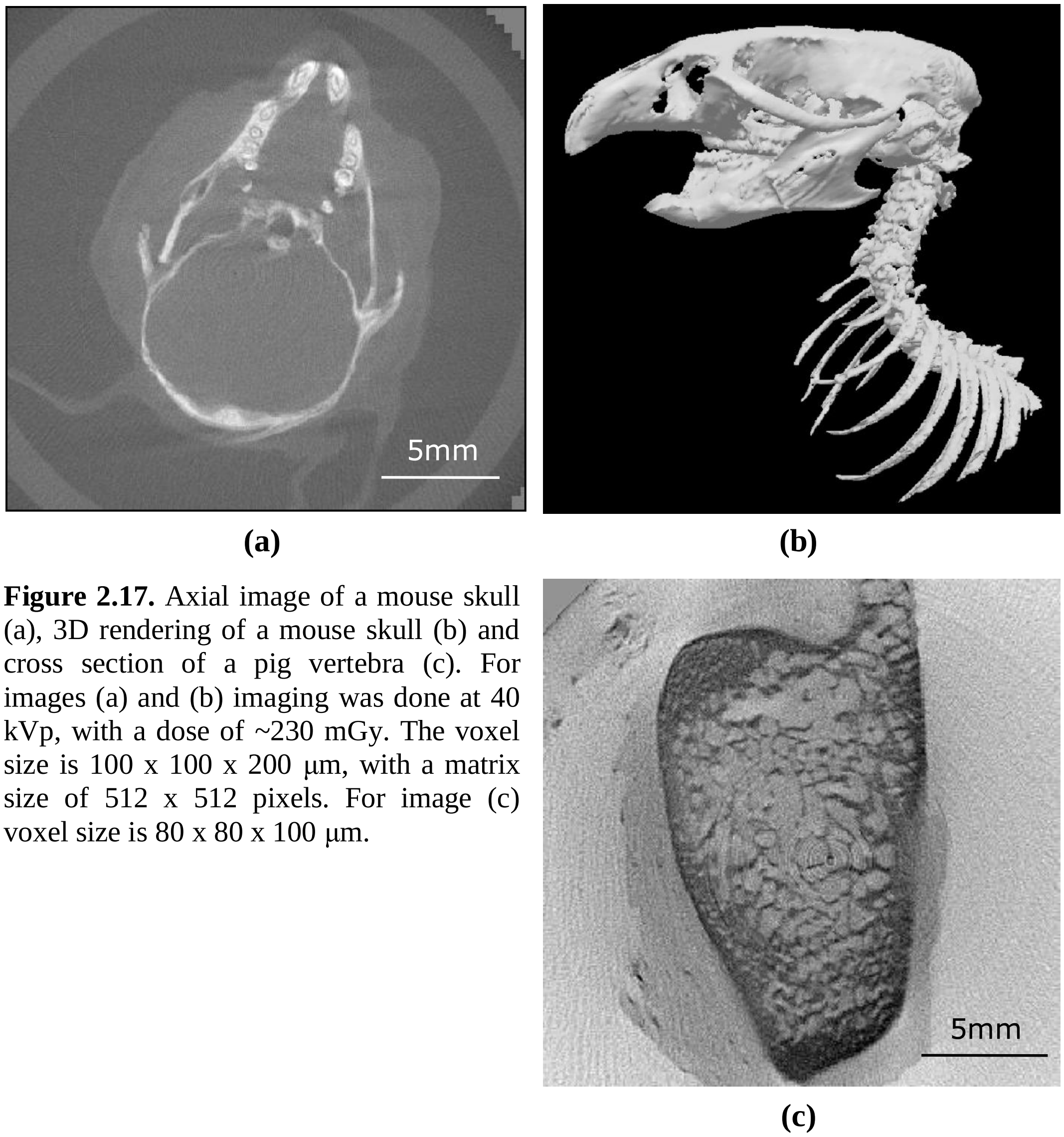

(a) (b)

(c)

Figure 2.17. Axial image of a mouse skull (a), 3D rendering of a mouse skull (b) and cross section of a pig vertebra (c). For images (a) and (b) imaging was done at 40 kVp, with a dose of ~230 mGy. The voxel size is 100 x 100 x 200 μm, with a matrix size of 512 x 512 pixels. For image (c) voxel size is 80 x 80 x 100 μm.

2.6 Concluding Remarks

The design and characterization of a cone beam X-ray CT scanner has been described. The bench top X-ray CT scanner is based on a large area flat panel X-ray detector, a micro-focus X-ray source and a high precision rotation stage. The imaging performance of the X-ray source and FPD is examined in detail. The detector response curve was found to be non-linear at both low and high exposures. The response curve was "linearized" by using a polynomial gain correction technique involving fitting the response of the detector with a 3rd order polynomial function. The modulation transfer function of the detector was measured at approximately 8.6 cycles/mm at 10% contrast by using the angled edge technique. Contrast phantom measurements demonstrate very good low dose contrast for soft tissue and bone, however soft tissue contrast is limited. Contrast-to-noise ratio measurements show that the CT scanner performance is quantum noise limited. Further performance characterization of the reconstructed CT images (e.g. resolution and imaging parameter optimization) may be required before any future *in vivo* experiments – these were not performed for this thesis as the images presented here were judged to be satisfactory for combination with the subsequent low resolution optical techniques and phantom experiments.

Chapter 3

Optical Materials Fabrication and Characterization

An important component for the development of any optical device or therapy is the availability of suitable “phantom” materials that effectively simulate the structural, functional, and molecular properties of human or animal tissues. These optical phantoms are used for a number of purposes including the simulation of light distributions in tissue, the calibration of optical devices, the recording of reference measurements, and for performing routine quality control (77, 78). The main design objective for these applications is precise control over the absorption and scattering properties; however, other characteristics such as ease of fabrication, cost, long-term stability, and the mechanical properties may also be important (77). This chapter describes the types of phantoms that were used during the development of the bioluminescence tomography system as well as their characterization.

3.1 Material Selection

Many different types of tissue-simulating phantoms have been developed for diverse purposes in fields including luminescence imaging (24, 44), near-infrared

(NIR) tomography (79), and photodynamic therapy (PDT) (80). The simplest are aqueous suspensions which usually consist of Intralipid (a lipid emulsion that is used clinically as an intravenously administered nutrient) and India ink (81). Liquid phantoms are extremely versatile as there is great freedom in the choice of scatterers and absorbers that can be used. Hundreds of studies have described liquid phantoms containing lipids, microspheres, titanium dioxide (TiO_2), blood, various inks, dyes and fluorophores (77). The main disadvantage of liquid phantoms is the difficulty of including heterogeneities. This has led to the development of various hydrogel-based phantoms such as gelatin (82), agar (83), and polyacrylamide (84), that can be formed into a variety of shapes and layers. Unfortunately, these phantoms have a short usable lifetime that is of the order of a few weeks.

Solid phantoms composed of rubbers or plastics have been described with greater long-term stability and shaping versatility (78). Phantoms made of epoxy resin (85), polyurethane (78), polyester (86), and silicone (87), have been described in the literature. Silicone has similar mechanical characteristics to tissue but epoxy resin, polyurethane and polyester are easier to machine. The choice of host material for solid phantoms is usually determined by the choice of absorbers and their stability in the chosen medium. Commonly used scatterers include metal oxides such as aluminum oxide and TiO_2, and microspheres.

Several variables contribute to the selection of the ideal phantom material for any specific application. For the development and characterization of the optical imaging capabilities of the multispectral bioluminescence tomography system, the goal was to make a durable phantom that mimicked the absorption properties of tissue over the emission spectrum of luciferase (500–700 nm (44, 45)), and that could be easily machined to include heterogeneities of various shapes and sizes.

3.1.1 Liquid Phantoms

The liquid phantoms used in the tissue simulating phantoms consisted of a lipid emulsion called Intralipid (IL 20% Pharmacia Corp.) which provided the scattering properties. The scattering properties of the solution are controlled by diluting the Intralipid with distilled water. Dyes were then added to increase the absorption coefficient of the solution. India ink is used as a broadband absorber with a flat absorption spectrum from 500–700 nm, and a very small scattering coefficient (88). Epolight 5457 and Epolight DT7-52A dyes (Epolin Inc., Newark, New Jersey) were also used in the liquid phantoms when a tissue-like spectrum was desired. The absorption coefficient of each dye in solution was linear with respect to concentration allowing for easy control of the optical properties of the solution.

3.1.2 Solid Phantoms

The solid material chosen for the tissue-simulating phantoms has three components: an epoxy resin, absorbing agents and a scattering agent. A two-part epoxy resin system (Araldite GY 502 resin, Aradur HY 837 hardener; Huntsman Advance Materials Inc., The Woodlands, Texas) was chosen for the host material. The epoxy resin was selected on the basis of previous experience in our lab with this material in the fabrication of broadband absorbing phantoms. The epoxy resin is formed by mixing the resin and hardener in a ratio of 100/26 by weight (100/30 by volume). The epoxy system has a pot life of approximately 30 min, allowing for sufficient time to add the absorbing and scattering agents and to degas the mixture. The resin hardens within 2 h at room temperature preventing any significant settling of the mixture, and can be demolded in 24 h. Generally a minimum of 48 h are required before the material is hard enough for machining, whereas complete curing requires up to 7 days.

Three dyes were evaluated for their ability to mimic the absorption characteristics of tissue from 500–700 nm: Epolight 5411, Epolight 5457 and Epolight DT7-52A (Epolin Inc., Newark, New Jersey). The dyes are intended for use in epoxy systems and are advertised as having high thermal stability and no fluorescence. It was confirmed that neither dye was fluorescent at excitation wavelengths of 550–650 nm. Epolight 5411 and Epolight 5457 are triphenylmethine-based dyes, having large absorption peaks close to 600 nm. Upon combination with the epoxy resin described above, the absorption spectra of both dyes shifted slightly to lower wavelengths, which resulted in absorption spectra similar to that of hemoglobin in tissue. Epolight DT7-52A is an anthraquinone dye whose absorption spectrum is stable upon incorporation into the epoxy resin. India ink was also used on occasion as a broadband absorber.

Titanium dioxide (Aldrich Chemical, Milwaukee, Wisconsin) with a particle size <5 µm was used as the scattering agent. Aluminum oxide was also tried but could not be added to the resin in sufficient quantities to mimic the scattering of tissue without aggregation occurring. This is because the refractive index of aluminum oxide (n=1.76) is closer to that of the epoxy resin (n=1.56) than is the refractive index of TiO_2 (n=2.50), such that larger concentrations are required.

3.2 Tissue Simulating Phantom Fabrication

The detailed fabrication process for the solid epoxy phantoms is described in Appendix A. In general the same procedure was used to make all the phantoms used for the characterization of the bioluminescence tomography system, adjusting the quantity and combination of dyes, scatterers and epoxy resin to obtain the required optical properties and volume.

In brief, all phantoms are made with stock solutions of each dye dissolved in ethanol for repeatability. The TiO_2 is also suspended in an ethanol solution to help ensure thorough mixing with the resin. Both the scatterers and dyes are added to the resin which was then degassed before addition of the hardener. Upon combination with the hardener the mixture is degassed once again and poured into a polystyrene mold. After degassing, the phantoms were left to cure in a water bath for 24 h before removal and 48 h prior to machining. Regions with different optical properties can then be added by filling machined cavities with liquid solution as described in section 3.1.1.

3.3 Phantom Characterization - Methods

The optical properties of the tissue-simulating phantoms were measured using a steady-state spatially resolved diffuse reflectance system described by Farrell *et al*. (89) and Hyde *et al*. (90). Briefly, a flat black multi-fiber probe (Fiberguide Industries, Sterling, New Jersey) consisting of a single source fiber and 25 collection fibers is used for illumination and light collection (100 µm fiber diameter, NA = 0.22). The probe face is placed in contact with the surface of the phantom, illuminating the sample surface from the source fiber using a filtered 100 W quartz-tungsten-halogen (QTH) broadband light source (Oriel Instruments, Stratford, Connecticut). Multiply scattered light is collected at 14 distances ranging from 1–10 mm from the source fiber. The light collected from the detection fibers is coupled into an imaging spectrometer (Kaiser Optical Systems, Ann Arbor, Michigan) and imaged onto a CCD (Princeton Instruments, Trenton, New Jersey). The light source was filtered to optimize signal between 500 and 700 nm. A schematic of the spatially resolved diffuse reflectance system is shown in Figure 3.1.

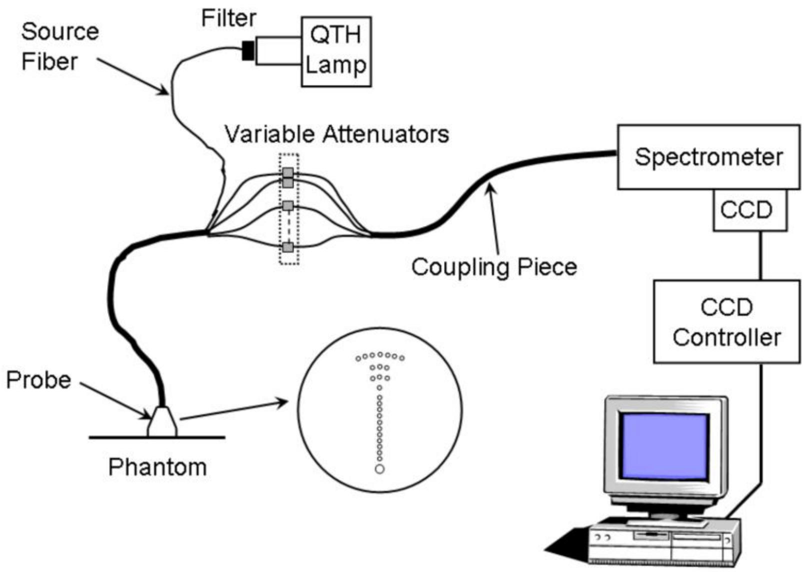

Figure 3.1. Schematic diagram of the steady-state spatially resolved diffuse reflectance system.

In order to obtain optical properties from the measurements, a reflectance model is required. The reflectance model describes the light re-emitted from the phantom surface as a function of the absorption and reduced scattering coefficients, the relative refractive index between the phantom and probe, and the source to detector distance. A Monte Carlo-based non-linear regression model in combination with a custom Matlab program was used to obtain the best possible estimates of the optical properties from the reflectance measurements as previously described (91, 92).

In general, the phantoms were measured before every experiment when possible, except for solid epoxy phantoms that could not be retested due to machining. Each phantom was measured at least five times at different locations on the surface resulting in at least five independent measurements of absorption and reduced scattering coefficients. The absorption and reduced scattering coefficients reported are the average of these measurements. A coupling fluid was used for all measurements on solid phantoms to minimize any artifacts due to index mismatches between the probe and phantom surface.

3.4 Phantom Characterization - Results

3.4.1 Probe Coupling Effects

The detection of diffuse light from solid materials requires caution because the quality of optical contact is dependent on factors that are difficult to quantify, such as the pressure exerted, surface irregularities and the refractive indices. The probe used for reflectance measurements is constructed of black plastic, so that its surface approximates a perfectly absorbing or matched boundary. The Monte Carlo model used for the fitting of absorption and scattering also assumes matched boundary conditions. This assumption has been shown valid for measurements of liquid phantoms and tissue where good coupling between the probe face and measurement surface can be achieved (90, 93). However when using solid phantoms, incomplete coupling between the probe and phantom surface due to surface irregularities can result in a large index mismatch due to air gaps between the two surfaces. A coupling fluid can be used to remove this air gap and restore the assumption of a matched boundary. However there is still the possibility of light channeling between the probe and phantom surface. Coupling effects were explored by measuring the optical properties of a phantom using coupling fluids with refractive index ranging from 1.33–1.56.

Steady-state diffuse reflectance spectra were measured using five different coupling fluids: water (n=1.33), 60% sucrose solution (n=1.44), vegetable oil (n=1.47), ethyl salycilate (n=1.52), and ethyl cinnamate (n=1.56).

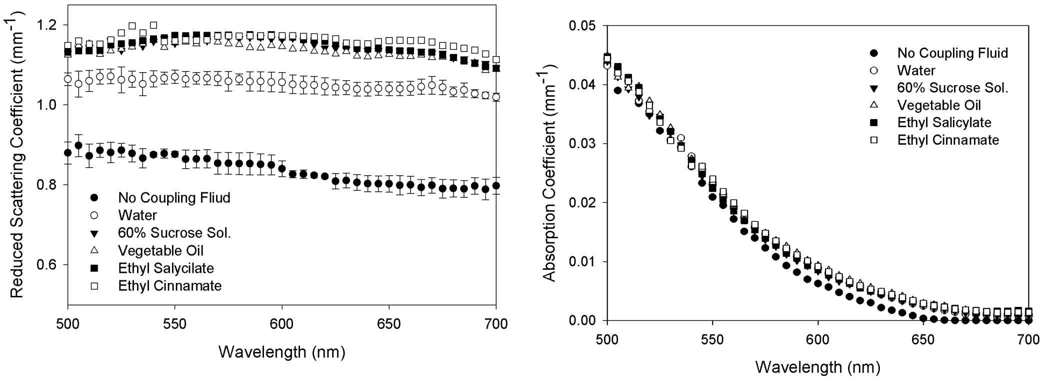

(a) **(b)**

Figure 3.2. The reduced scattering coefficient spectrum (a) and absorption coefficient spectrum (b) measured using five coupling fluids with different refractive indexes. The phantom contains 3.15 µL/L of Epolight 5411 dye. The error bars shown represent the standard deviation of five sets of reflectance measurements. Some error bars in (a) have been omitted for clarity. The error bars (not shown) in (b) are similar in magnitude to those shown in Figure 3.4. The refractive indices of the coupling fluids are as follows: water (n=1.33), 60% sucrose solution (n=1.44), vegetable oil (n=1.47), ethyl salycilate (n=1.52), and ethyl cinnamate (n=1.56).

The reduced scattering and absorption coefficients recovered using our reflectance model is shown in Figure 3.2. The recovered absorption coefficients for all the coupling fluids agree within the range of measurement uncertainty; however the absorption recovered using no coupling fluid is significantly lower for wavelengths above 600 nm. The measured reduced scattering coefficients show an even larger disagreement among coupling fluids, falling into three distinct groups. The average reduced scattering coefficient in the absence of a coupling fluid was ~0.82 mm^{-1}. The coupling fluids with refractive index below 1.47 (the approximate refractive index of the probe) resulted in average reduced scattering coefficients between 1.03–1.05 mm^{-1} (ethanol (n=1.36) and 40 % sucrose (n=1.40) were also used but results are not shown in Figure 3.2 for clarity). Finally, all coupling fluids with a refractive index between the probe and phantom material (n=1.47–1.56) resulted in average reduced scattering values between 1.14–1.16 mm^{-1}. Based on these results, vegetable oil with a refractive index of 1.47 was used as a coupling fluid for all measurements of solid phantom materials.

3.4.2 Liquid Phantom Properties

Several types of liquid phantoms were used throughout the development of the bioluminescence tomography system. These solutions can be used to fill the cavities that are machined into the solid epoxy resin phantoms, simulating regions of differing absorption and scattering properties. Figure 3.3a shows the absorption and scattering properties of an Intralipid solution with India ink as an absorber. The India ink solution has a broad absorption spectrum that can be combined with other dyes to simulate tissue-like absorption. A solution of India ink and Epolight DT7-52A is shown in Figure 3.3b. Also shown on this plot is the absorption spectrum of oxy-hemoglobin. The two absorption peaks of oxy-hemoglobin (576 and 542 nm) are very close to the Epolight dye (580 and 540nm).

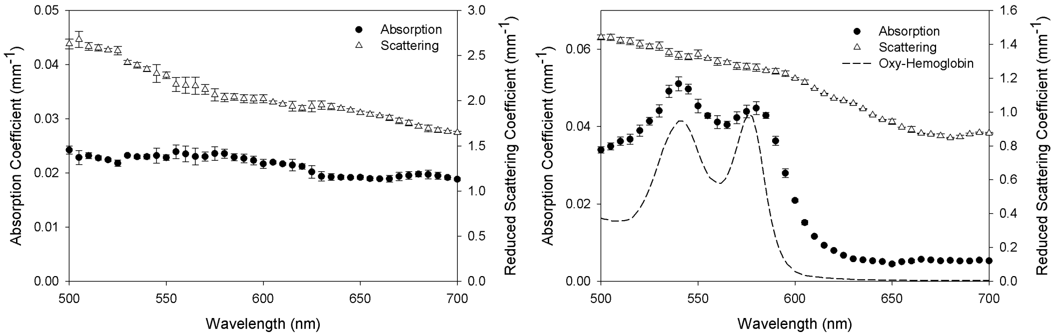

(a) **(b)**

Figure 3.3. The absorption coefficient and reduced scattering coefficient of liquid Intralipid phantoms made with (a) 1.5 % Intralipid and 3.3 µL/L of India ink, and (b) 1 % Intralipid, 8.3 µL/L India ink and 4.7 mg/L Epolight DT7-52A. Also plotted is the absorption spectrum of oxy-hemoglobin on an arbitrary scale (94).

3.4.3 Solid Phantom Properties

The optical properties of epoxy phantoms containing Epolight 5411 and 5457 dyes were investigated by fabricating two batches of phantoms (six for each dye) with increasing absorption, but the same reduced scattering coefficient. The optical properties were chosen to represent physiologically relevant values for absorption coefficients. The variation of the reduced scattering coefficient amongst the 12 phantoms is shown in Figure 3.4.

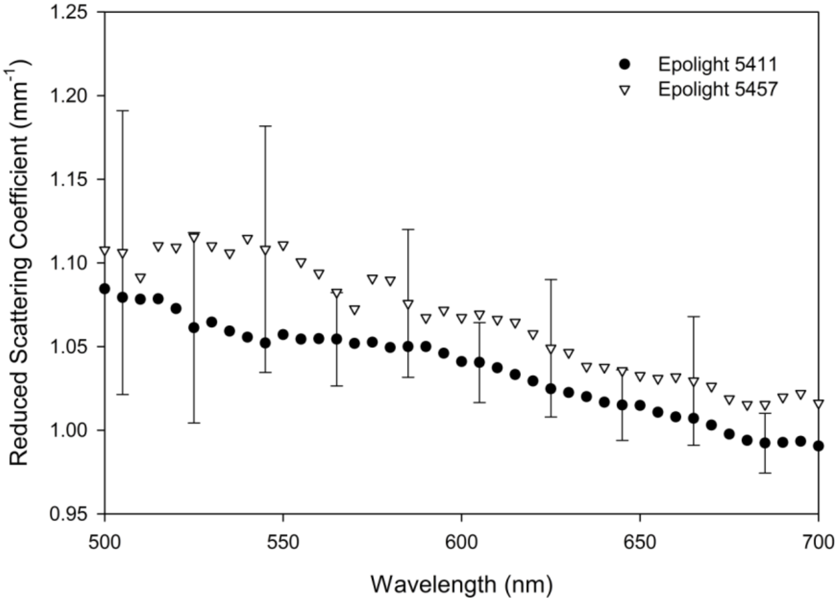

Figure 3.4. The reduced scattering spectrum for the two phantom batches made with Epolight 5411 and Epolight 5457 as absorbers. The six phantoms within each batch were made from the same mixture of resin and TiO_2. The error bars represent the standard deviation of the measured scattering coefficient within each phantom batch (for clarity, only representative error bars are plotted). The average difference in scattering between the two batches is ~3 % over the spectral range shown.

The reduced scattering coefficients differ between the two batches (Epolight 5411 and 5457) by an average of 3 % over the spectral range shown. The variability within each batch is similar in magnitude, with mean standard deviations of 3 and 5 % respectively over the same spectral range. This difference is an indication of the reproducibility of the tissue phantoms. As the six phantoms within each batch were made from resin containing an equal amount of TiO_2, the scattering coefficients within each batch should be identical. Great care was taken to stir the TiO_2 mixture to prevent settling and to minimize the inhomogeneities within each batch. Weighing errors during phantom fabrication were minimal with the largest error in all fabrication steps reaching 0.5 %. The most probable source of variability is due to the coupling effects at the probe to phantom surface as well as uncertainties in the Monte Carlo fitting.

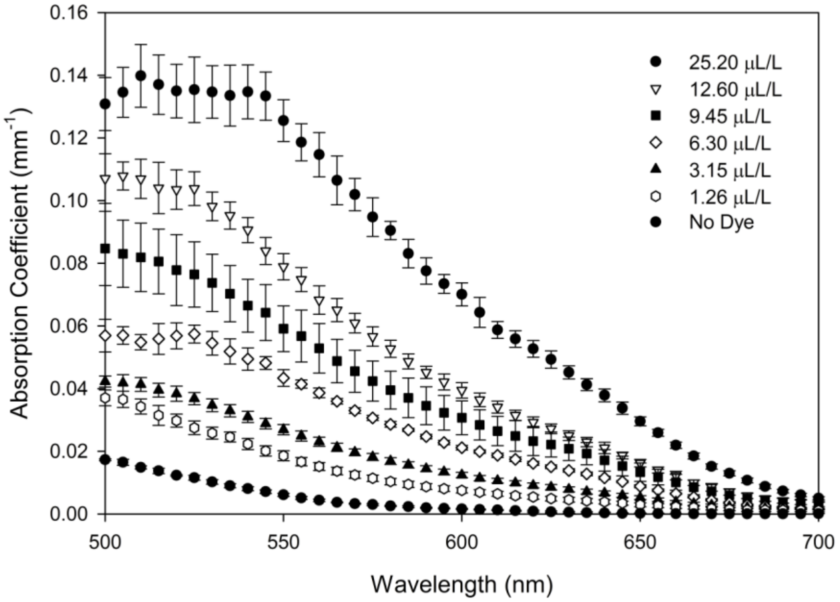

Figure 3.5. The absorption coefficient spectrum for the tissue phantoms made with Epolight 5411 at increasing concentrations. The error bars are the standard deviation of the results from five measurements of reflectance for each dye concentration. Vegetable oil with a refractive index of 1.47 was used as the coupling fluid.

The measured absorption coefficients for the Epolight 5411 and Epolight 5457 dye phantoms are shown in Figure 3.5 and Figure 3.6 respectively. The dyes have similar peak absorption coefficients at equal concentrations and both exhibit decreasing absorption above 550 nm. Epolight 5411 has peak absorption at or below 500 nm, with gradually decreasing absorption to 700 nm. The Epolight 5457 dye has an absorption peak at 570 nm, and absorption rapidly decreases to almost zero by 640 nm. The measured absorption coefficient of both dyes is linearly related to their concentrations over the entire spectral range investigated (within the epoxy resin phantoms). A plot of absorption coefficient versus dye concentration for Epolight 5411 and Epolight 5457 is shown in Figure 3.7.

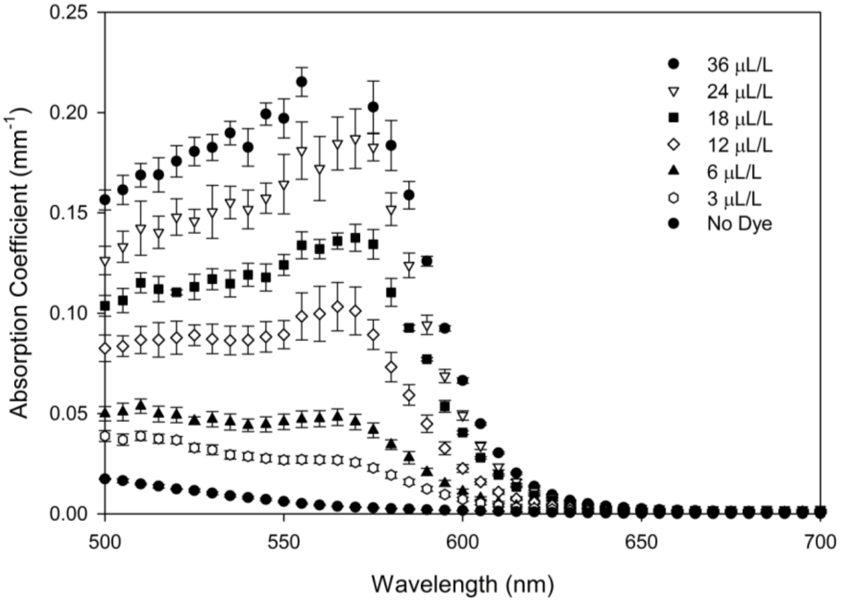

Figure 3.6. The absorption coefficient spectrum for the tissue phantoms made with Epolight 5457 at increasing concentrations. The error bars are the standard deviation of the results from five measurements of reflectance for each dye concentration. Vegetable oil with a refractive index of 1.47 was used as the coupling fluid.

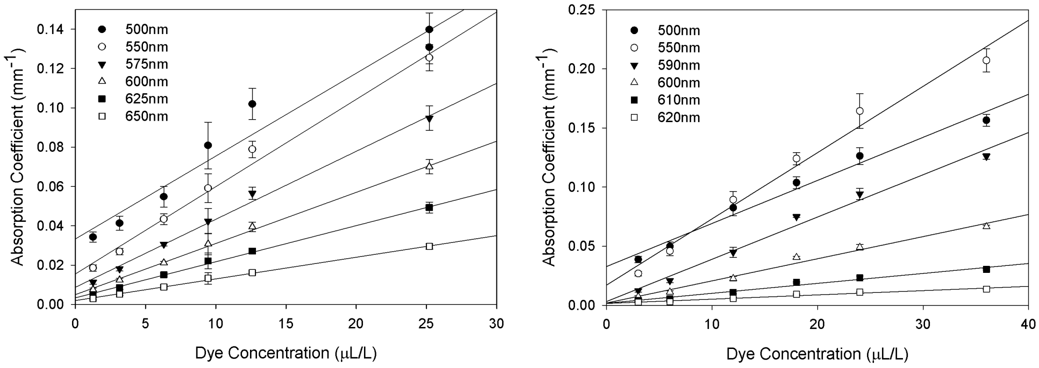

(a) **(b)**

Figure 3.7. The absorption coefficient as a function of dye concentration of tissue phantoms made with (a) Epolight 5411 and (b) Epolight 5457. The absorption coefficients are linearly dependent on dye concentration for both dyes over the entire spectral range shown. The regression lines do not pass through the origin due to the intrinsic absorption of the epoxy resin.

The absorption properties of a third dye, Epolight DT7-52A were also investigated as the manufacturer claims it is photostable. The spectrum of this dye does not change during the epoxy mixing process and does not exhibit any bleaching during the curing process. Figure 3.8 shows the absorption coefficient plotted versus wavelength for Epolight DT7-52A in the epoxy resin. The spectrum is almost identical to its spectrum in an Intralipid solution. The two absorption peaks are shifted slightly to higher wavelengths (585 and 545nm) and absorption drops to zero at 640 nm similar to that of Epolight 5457.

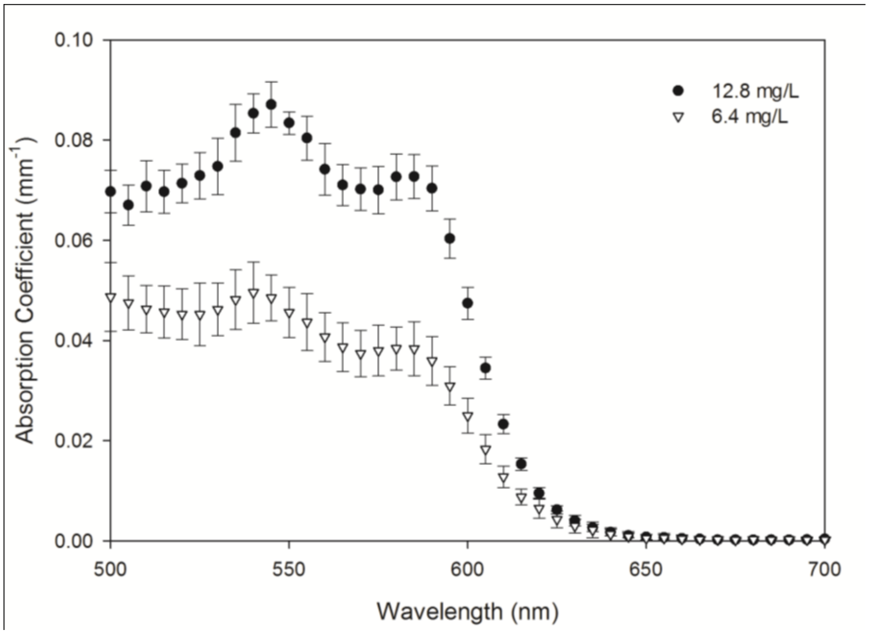

Figure 3.8. The absorption coefficient spectrum for the tissue phantoms made with Epolight DT7-52A. The error bars are the standard deviation of the results from five measurements of reflectance for each dye concentration. Vegetable oil with a refractive index of 1.47 was used as the coupling fluid.

3.4.4 Epoxy Phantom Stability

The optical stability of the tissue phantoms was studied for a period of up to 4 months after casting. The phantoms were stored at room temperature in a light tight container. Figure 3.9 shows the absorption coefficients for one phantom containing Epolight 5411 and another containing Epolight 5457 dye. There is a significant decrease in the absorption coefficients of both phantoms during the first few weeks however the bleaching slows significantly after curing for 3 months. There is also some evidence that the phantoms may be sensitive to prolonged exposure to ambient light, therefore long term storage in a light tight container in recommended. Phantoms made with Epolight DT7-52A were found to be more resistant to bleaching during the initial curing process and were also found to be more stable during storage.

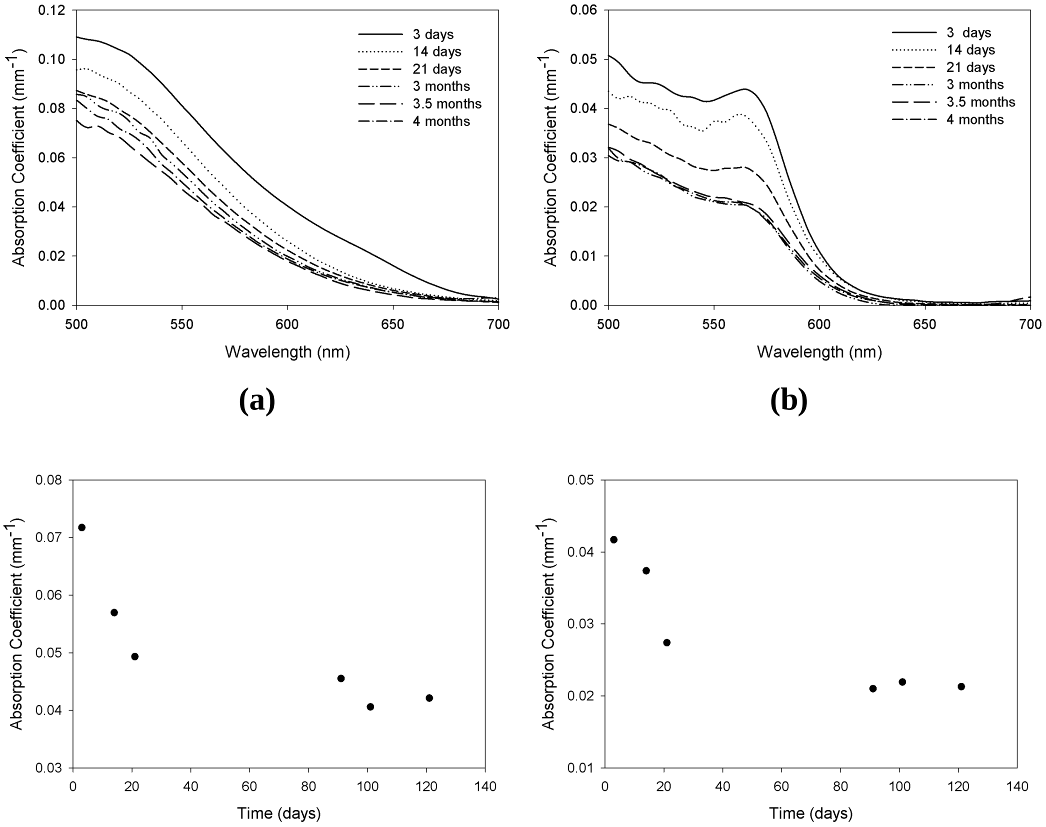

(a) **(b)**

(c) **(d)**

Figure 3.9. The absorption coefficients of the tissue phantoms measured over a period of 4 months from the time of fabrication. Representative examples of phantoms made with both Epolight 5411 ((a) and (c)) and Epolight 5457 ((b) and (d)) are shown. Figures (c) and (d) show the absorption coefficient vs. time at a wavelength of 550 nm.

3.4.5 Reflectance Spectra

The large absorption gradient in the Epolight 5457 phantoms is quite similar to the absorption gradient of hemoglobin in tissue from ~580 nm to ~630 nm. In fact, the color of many of the phantoms described above was subjectively very similar to that of Caucasian skin. A simple experiment was performed to qualitatively compare the diffuse reflectance spectra from the tissue phantoms to that of a human volunteer using an integrating sphere and a fiber optic spectrometer (SD2000, Ocean Optics, Dunedin, Florida). The measured diffuse reflectance spectra are shown in Figure 3.10. The total diffuse reflectance is higher for the tissue phantom material; however the spectral characteristics closely match that taken from the palm of a volunteer.

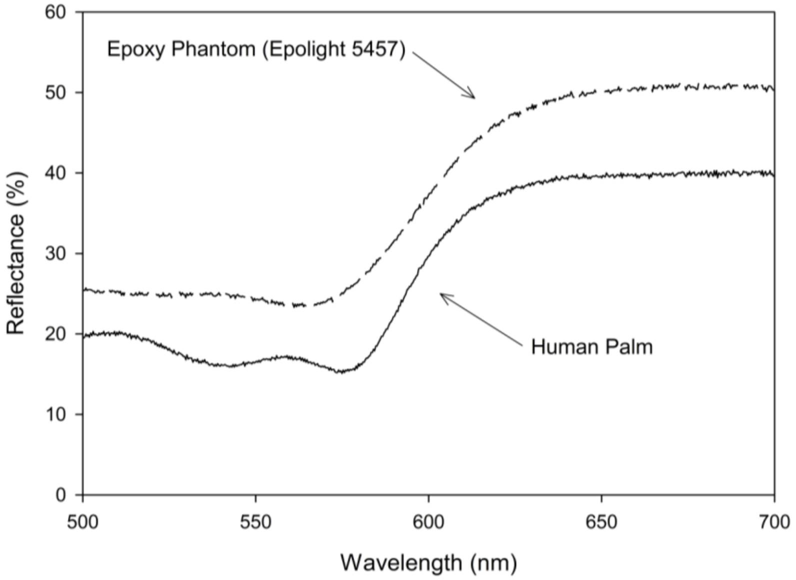

Figure 3.10. Diffuse reflectance spectra measured using an integrating sphere from the palm of a volunteer and the spectrum measured from one of the tissue phantoms made with Epolight 5457. The reflectance spectra are normalized to a 99% reflectance standard. The reflectance spectrum for the epoxy phantom is very similar to that for Caucasian skin. The addition of a broadband absorber such as India ink could provide even closer agreement.

3.5 Concluding Remarks

The optical properties of several different tissue-simulating phantoms have been investigated for use as test objects in the characterization of a multispectral bioluminescence tomography system. These test phantoms typically consist of a solid epoxy resin cylinder with machined cavities to contain liquids with differing optical properties. The liquid phantoms are easily reproducible, and stable with all dye combinations described above. They could be made before each experiment and stored for a couple of weeks under refrigeration. The solid epoxy phantoms require a few days to fabricate and machine and are stable after a curing period of 3 months. For these phantoms, Epolight DT7-52A was the best option due to its relative stability and closer match to tissue over the range of 500 to 700 nm.

Chapter 4

Diffuse Optical Tomography

In this chapter I describe the development and evaluation of an integrated DOT/X-ray CT system. The DOT system is used to recover accurate optical property distributions for use in the multispectral bioluminescence tomography system described in Chapter 5. The DOT system uses a non-contact CCD camera to acquire measurements of the surface emittance, and a finite element model of the propagation of light in tissue to recover the internal optical property distribution of a test subject. *A priori* spatial information from the X-ray CT is used to constrain the DOT reconstruction algorithm. The chapter contains a description of the inverse reconstruction algorithms used and the simulations and experiments conducted throughout the evaluation of the DOT system.

4.1 Reconstruction Algorithms

4.1.1 The Inverse Problem

The goal of the inverse problem is to recover the optical properties (μ_a, μ_s') at each node in the FE mesh using measurements of light fluence rate at the tissue surface. In NIRFAST (95), the inversion is achieved by using a modified Tikhonov minimization. The standard Tikhonov minimization function is given by:

$$\chi^2 = \overset{min}{\underset{\mu}{}} \left\{ \sum_{i=1}^{NM} \left(\Phi_i^M - \Phi_i^C \right)^2 + \lambda \sum_{j=1}^{NN} \left(\mu_j - \mu_0 \right)^2 \right\} \tag{4.1}$$

where the measured fluence at the tissue surface is represented by Φ^M, the calculated data using the forward model by Φ^C, NM is the total number of measurements obtained from the imaging device, and NN is the number of FEM nodes (the unknowns). λ is the Tikhonov regularization parameter, which is defined as the mean ratio of the variances of the measurement data and optical properties ($\lambda = \sigma_{\Phi^M}^2 / \sigma_\mu^2$) (96), and μ_0 is the initial estimate of the optical properties at j. It has been found that if the initial estimate, μ_0, is close to the actual optical property distribution, this term can be ignored (48).

The minimization with respect to μ in equation 4.1 involves setting the first-order derivative equal to zero $\partial \chi^2 / \partial \mu = 0$ and ignoring higher order terms. The first-order approximation is given by:

$$\left(\frac{\partial \Phi^C}{\partial \mu} \right)^T (\Phi^M - \Phi^C) - \lambda(\mu - \mu_0) = 0 \tag{4.2}$$

The derivative matrix $\partial\Phi^{C}/\partial\mu$ is known as the Jacobian matrix, *J*, and is also referred to as the weight or sensitivity matrix. Using this linear approximation of the problem, and solving it as an iterative Levenberg-Marquardt scheme gives:

$$\left(J^{T}J+\bar{\lambda}I\right)^{-1}J^{T}\delta\Phi=\delta\mu \qquad (4.3)$$

where $\delta\mu$ is the update for the optical properties and $\delta\Phi$ is the data-model mismatch at the current iteration, I is the identity matrix, and $\bar{\lambda}\equiv 2\lambda$. The Jacobian defines the relationship between changes in boundary data Φ^{C} resulting from small changes in optical properties. The structure of the Jacobian is reviewed by Dehghani *et al* in (95, 97). It consists of both amplitude and phase data for the frequency domain problem and defines how small changes in the optical properties at each node affect the amplitude and phase measurements at the surface. A frequency domain system makes use of both the phase and amplitude data, while a continuous wave system as described in this thesis uses only amplitude data by setting the phase component equal to zero. As a result of the missing phase data, reliable recovery of both absorption and scattering coefficients is no longer possible; however the effective attenuation coefficient, defined as $\mu_{eff}=\sqrt{3\mu_{a}(\mu_{a}+\mu_{s}')}$, can be recovered as will be shown.

In general, λ is implemented in a modified LM algorithm (98), where it is initialized as the variances ratio and is systematically reduced at each iteration (initially 10, reduced by a factor of $10^{0.25}$ and scaled by the maximum diagonal of $J^{T}J$). The reducing factor was determined empirically from simulations and phantom studies by Yalavarthy el al. and the initial value for λ is chosen according to the noise in the data (96). Another approach investigated here holds λ constant at each iteration; essentially repeating the single-step Tikhonov method until the stopping criterion is reached. The iterative procedure is repeated until the change in the minimization function (equation 4.1) is less than 2%.

4.1.2 Spatial Priors

It has been shown that significant improvement in the stability and accuracy of the reconstruction process can be obtained by including prior anatomical information from other imaging modalities (21, 23). Earlier studies have shown that optical contrast can be correlated to MR contrast (23, 99) and that structural MRI images can be used to reduce the number of unknown optical parameters to be recovered. Although X-ray CT offers relatively poor soft tissue contrast, it is much more cost effective and provides sufficient contrast between fat, musculature, and bone (the MR contrast exploited in earlier studies relies largely on fat contrast).

Two methods are explored here for incorporating the anatomical prior information into the DOT reconstruction problem. The first method is a parameter reduction approach, referred to as hard priors (97, 100). This technique constrains the optical properties within a segmented region to a single value, which introduces the potential for errors by imposing incorrect model assumptions due to inaccuracies in the prior information. Inaccurate prior information can result from inaccurate segmentation of X-ray CT images (registration or digitization errors) as well as mismatches between the regions of CT contrast and optical contrast. Another method for constraining the inverse problem, often described as soft priors, penalizes the variation within each region which is assumed to have the same properties by controlling regularization (23, 97). The soft priors' method does not impose a rigid constraint on the optical properties within each region. This reduces the biases that can be caused by the use of imperfect prior information.

4.1.3 Hard Spatial Priors

The FEM mesh is segmented by assigning all nodes within each region an appropriate label (e.g. background = 0, region 1 = 1 etc). In general, with structural segmentation into *n* regions, single values of absorption and scattering are reconstructed within each region. A matrix transformation is applied to *J*, such that:

$$\tilde{J} = JK \tag{4.4}$$

where the dimensions of $\tilde{J}$ are the number of measurements by the number of regions (NM x NR). *K* is called the *a priori* matrix:

$$K = \begin{array}{c} \begin{bmatrix} k_{1,1} & k_{1,2} & \cdots & k_{1,n} \\ k_{2,1} & k_{2,2} & \cdots & k_{2,n} \\ \vdots & \vdots & \ddots & \vdots \\ k_{j,1} & k_{j,2} & \cdots & k_{j,n} \end{bmatrix} \\ \begin{matrix} R_1 & R_2 & \cdots & R_n \end{matrix} \end{array}, \qquad \text{where } k_{\xi,\eta} = \left\{ \begin{matrix} 1, & \quad \xi \in R_\eta \\ 0, & \quad \xi \in R_\eta \end{matrix} \right\} \tag{4.5}$$

In effect a new Jacobian matrix, $\tilde{J}$ is produced where all elements from the columns corresponding to the same regions have been added together. The iterative algorithm now solves:

$$(\tilde{J}^T\tilde{J})^{-1}\tilde{J}^T\delta\Phi = \widetilde{\delta\mu} \tag{4.6}$$

where the dimensions of the solution update vector, $\widetilde{\delta\mu}$, are 2 × NR. During the update process, we apply:

$$\delta\mu = \widetilde{\delta\mu}K^{-1} \tag{4.7}$$

In general, regularization is not required in solving matrix equation 4.6 because NR << NM, however in the presence of noise, some regularization is added to attain a stable solution.

4.1.4 Soft Spatial Priors

In order to add spatial constraints to the minimization function, equation 4.3 is modified by adding a penalty term as follows:

$$\left(J^T J + \bar{\lambda} L^T L\right)^{-1} J^T \delta\Phi = \delta\mu \tag{4.8}$$

where $\bar{\lambda}$ is now the regularizing parameter for the spatial prior data, and L is the penalty matrix created from the X-ray CT derived spatial information. L is given by:

$$L_{ij} = \begin{cases} 0 & \text{if i and j are in not the same region} \\ -1/N & \text{if i and j are in the same region} \\ 1 & \text{if i = j} \end{cases} \tag{4.9}$$

where N is the number of finite element mesh nodes in a given region. The L matrix links all the nodes in a particular region such that a second differential operator is approximated within each region. This is similar to a total variation minimization approach allowing sharp boundaries to exist while providing flexibility to encode these boundaries from X-ray CT information. Each node in the FEM mesh is labeled according to the region, or tissue type, with which it is associated.

4.1.5 Spectral Reconstruction

When recovering the optical properties at multiple wavelengths, spectroscopic DOT information can also be used to recover the concentration of chromophores such as oxy- and deoxy-hemoglobin (19). For applications in multispectral BLT reconstructions of the optical properties need to be recovered at multiple wavelengths. Instead of reconstructing the optical properties at each wavelength separately, resulting in wild fluctuations of scattering and absorption properties from wavelength to wavelength (effective attenuation remains stable), constraints can be incorporated into the reconstruction directly.

The μ_s' spectrum of tissue has been shown to fit an empirical approximation to Mie scattering theory (101) given by:

$$\mu_s' = a\lambda^{-b} \tag{4.10}$$

where a is called the scatter amplitude, b is called the scatter power, and λ is the wavelength of light. Both the scattering power and amplitude depend on the scattering center size and number density and may reflect variations in tissue composition due to different cellular and structural sizes and densities (102). Typically, large scatterers have lower b and a values, whereas small scatterers have higher b and a values. Recovering the scatter amplitude and scatter power rather then μ_s' at each wavelength reduces the parameter space, improving the stability of the inverse problem and results in a realistic variation in μ_s' as a function of wavelength.

4.1.6 Reconstruction Basis

There are a number of different strategies for defining the reconstruction basis, including using a second finite element mesh or a Cartesian pixel basis (56). The choice of reconstruction basis allows for computational efficiency, which reduces the number of unknowns in the reconstruction algorithm. The forward problem requires that the volume of interest be subdivided into an adequate number of sub-domains to allow for sufficient resolution and accurate solutions of the calculated forward solutions while a reduction in the number of reconstructed unknowns decreases the ill-posedness of the inverse reconstruction algorithm. This is addressed by defining a separate reconstruction basis (different from the meshes used to generate the forward solutions), upon which the unknown parameters are updated. In this work a regularly spaced Cartesian pixel basis is used for the recovery of optical properties when using no spatial priors and soft spatial priors during reconstruction. In general the pixel basis used is a 30 by 30 grid unless otherwise noted. For the hard spatial prior reconstructions the reconstruction basis used was the same as the forward mesh.

4.2 Simulations

4.2.1 Source-Detector Geometry

A set of simulations was performed to examine the optimal strategy for collecting non-contact surface fluence measurements on the integrated X-ray CT/DOT system. A fan beam geometry mimicking the source detector geometry of X-ray CT was compared to a full 360 degree detector geometry. The source detector geometry was optimized by adjusting parameters such as the number of sources (4, 8, 16, 32), and the detector density (7, 13, 25, 49).

Simulations were performed using a 1785 node, 43 mm diameter circular mesh. Four anomalies with differing optical properties, each with a diameter of 5 mm were added to the mesh. One anomaly had a 50 % increase in scattering, another a 50 % increase in absorption, and two had 20 % increases in scattering and absorption. Figure 4.1 summarizes the optical properties used for each of the four regions. Forward data were generated with approximately 2 % added noise and reconstructions (without prior information) were performed using the NIRFAST software. During the reconstruction the regularization parameter λ was initially set to 10 and allowed to decrease during iteration.

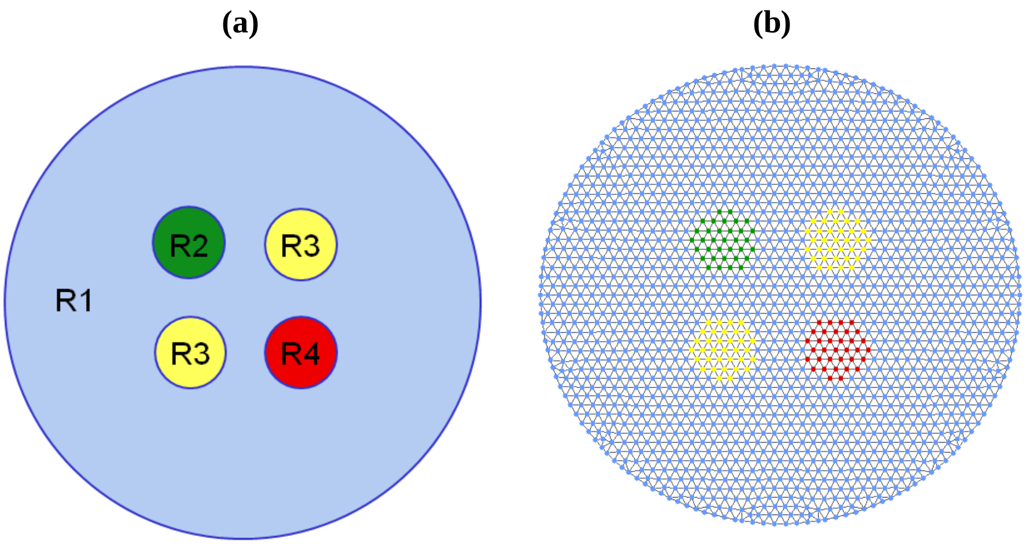

(c)

	Region 1	**Region 2**	**Region 3**	**Region 4**
μ_a (mm^{-1})	0.01	0.015	0.012	0.01
μ_s` (mm^{-1})	1	1	1.2	1.5
μ_{eff} (mm^{-1})	0.174	0.21	.209	0. 13

Figure 4.1. Optical properties for the forward mesh used to examine various source-detector combinations (a). The FEM mesh has 1785 nodes, 3418 elements, and 43 mm radius is in (b). Part (c) contains a summary of the optical properties of each region.

In traditional DOT experiments using optical fibers for surface fluence detection, fibers are arranged 360 degrees around the subject. However in the case of non-contact measurements, the imaging geometry limits the view to the side opposite the source. The effect of losing the 360 degree view was explored by comparing these reconstructions to a fan-beam geometry encompassing 135 degrees as shown in Figure 4.2. Empirically, the recovered effective attenuation maps are very similar to one another with a slight increase in variation of the background attenuation in the fan beam geometry. The RMS error of the 360 degree geometry was 2.76 %, while the error for the fan beam geometry was 2.95 %. All further simulations and experiments are performed using this fan beam source detector geometry.

Next, the optimal number of sources was examined. During imaging the number of source positions is easily altered by rotating the stage between views. For four sources the stage is rotated 90 degrees between images, for eight sources, it is rotated 45 degrees and so on. The results of the simulations are contained in Figure 4.3. In general, increasing the number of source positions yields a superior reconstruction of the effective attenuation at the expense of acquisition time. These results indicate that increasing the sources beyond 16 results in very limited improvements in the recovered optical property map.

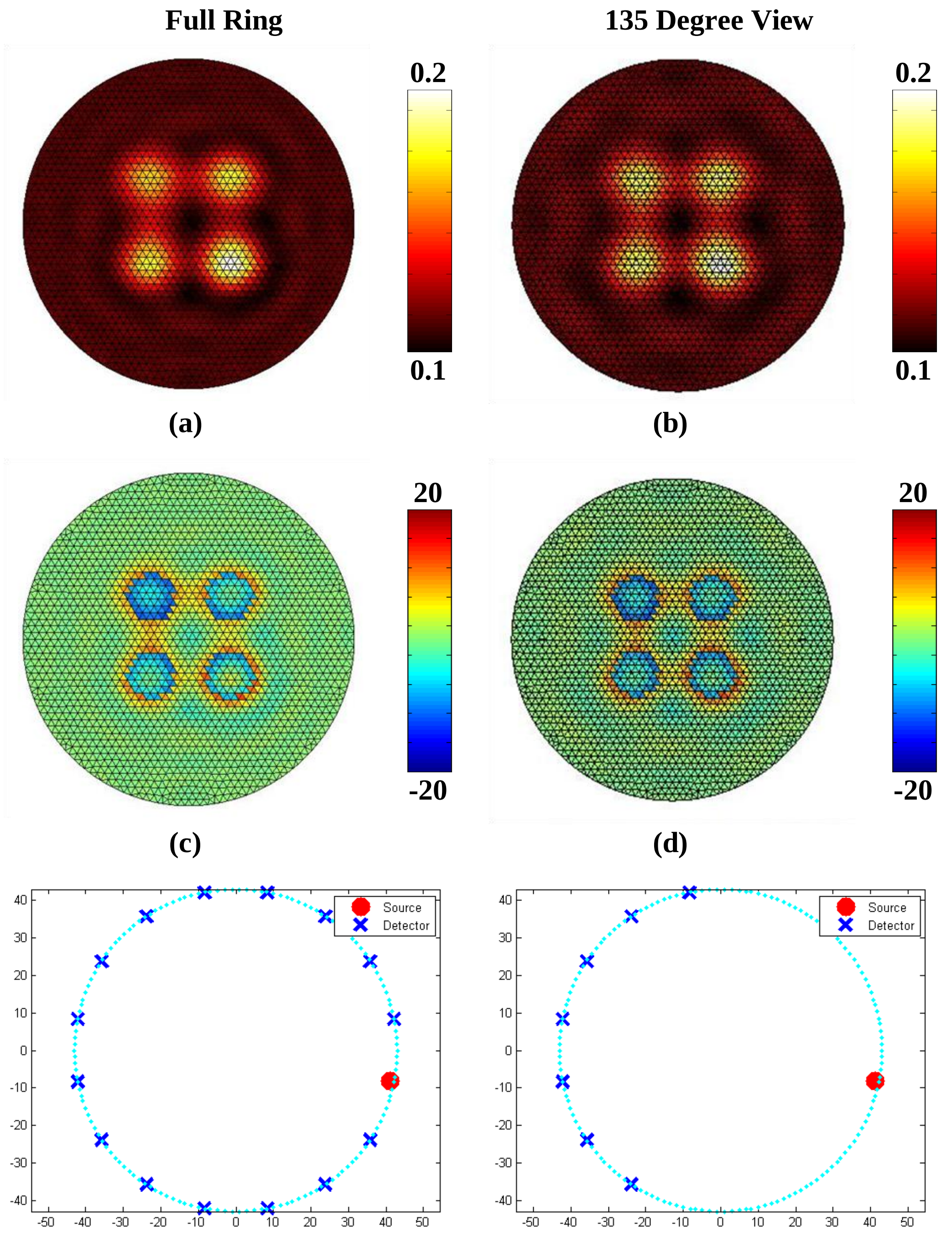

(a) (b)

(c) (d)

(e) (f)

Figure 4.2. The recovered effective attenuation (μ_{eff}) maps for the 360 degree and 135 degree geometries are found in (a) and (b) respectively. The corresponding percent error maps are shown in (c) and (d). Finally (e) and (f) show the source detector geometries used in each case. A total of 16 sources was used in each case.

	Effective Attenuation (μ_{eff})	**Percent Error**
4 Source Positions	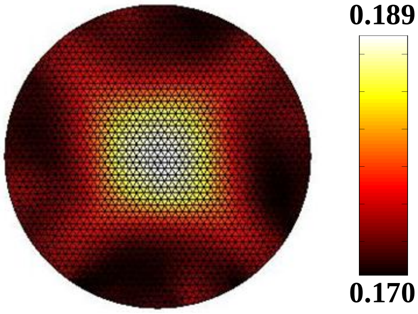	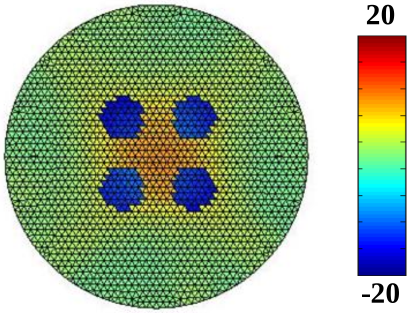
8 Source Positions	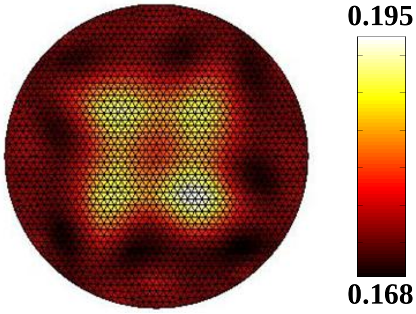	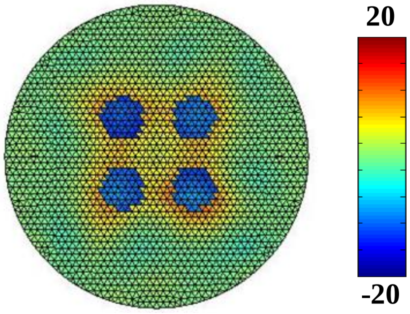
16 Source Positions	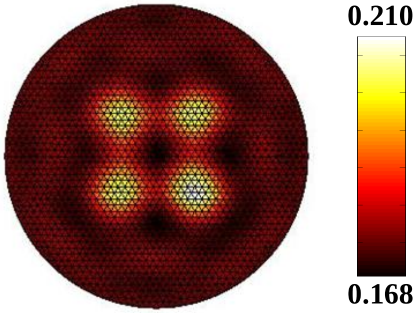	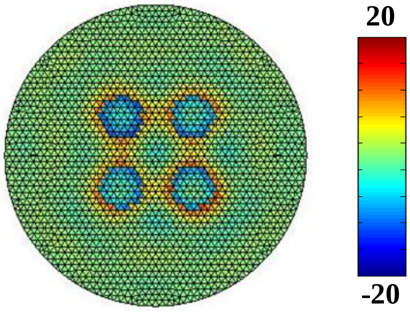
32 Source Positions	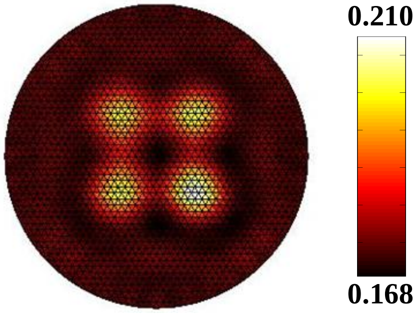	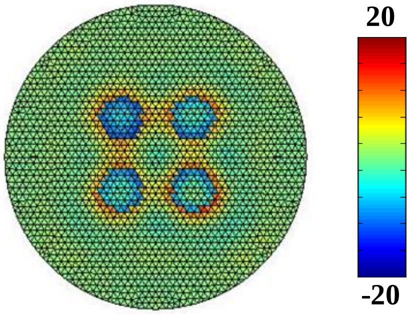

Figure 4.3. The results of simulations to determine the optimal source positions for DOT reconstructions in a fan beam geometry.

Lastly, the optimal detector density was investigated. Using a CCD detector for measurement allows for an almost arbitrary number of virtual detector locations to be used during reconstruction. A larger number of detectors is expected to improve the accuracy of the recovered optical properties, however the speed of the inverse algorithm is slowed, while the memory requirements increase dramatically. The results of the detector density simulations are shown in Figure 4.4. The detector density is increased by decreasing the angular spacing between detectors from 22.5 degrees to 2.8125 degrees. Empirically, the results show that the recovered optical property maps improve significantly up to 25 detectors while an increase to 49 yields almost identical results.

The results of the source-detector geometry simulations are summarized in Figure 4.5. The percent RMS error decreases with increasing detector density for simulations at all source positions. Similarly, the RMS error also decreases with increasing source position reaching a plateau at 16 sources. Based on these results a geometry of 16 source positions and 25 detectors was chosen for future experiments. It should be noted that these results are likely to change when the domain becomes more complex, such as when imaging the irregular surface of a mouse. Further optimization may be required for more complex cases.

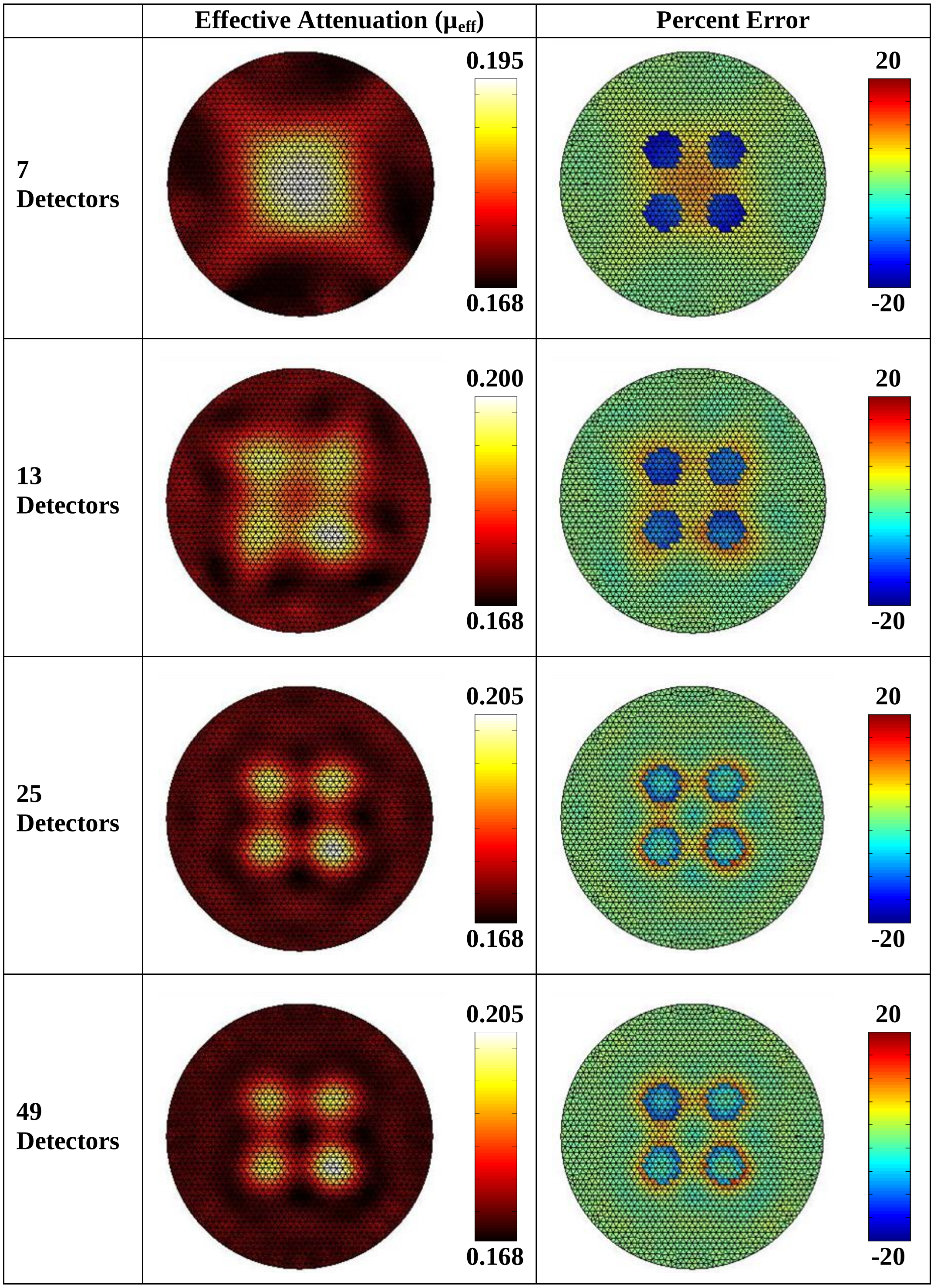

Figure 4.4. The effect of detector density on the recovered effective attenuation maps. Detectors were arranged in a 135 degree fan beam geometry, with decreasing angular separation.

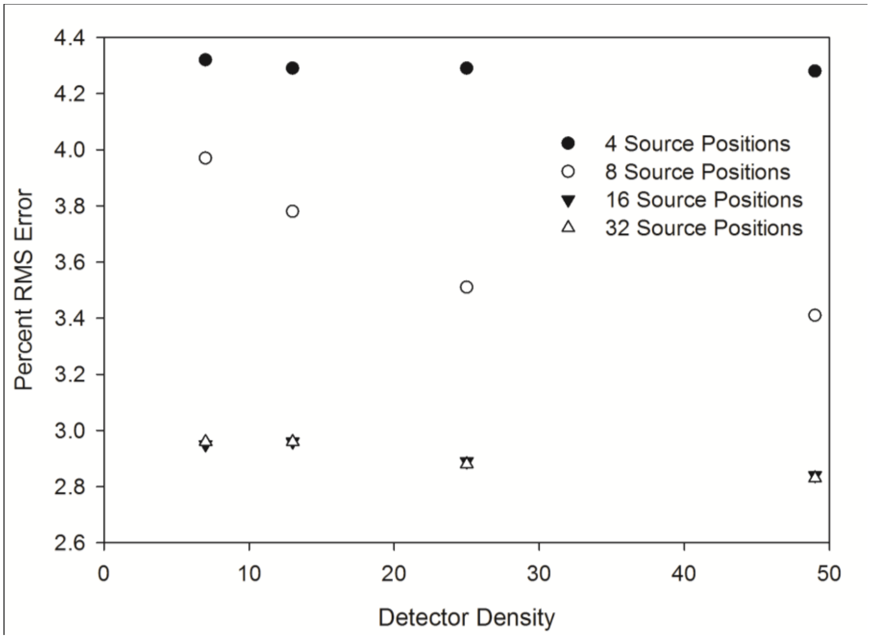

Figure 4.5. The percent RMS error for all source-detector geometry simulations described earlier. Based on these results an optimal configuration of 16 sources, and 25 detectors was chosen for future experiments.

4.2.2 The Effect of Errors in Spatial Priors

One of the main disadvantages of the hard spatial priors' reconstruction method is the potential of introducing errors when the *a priori* anatomical information does not correlate with optical contrast. For example, the mechanisms which lead to contrast in X-ray CT may not coincide with those that produce contrast in optical imaging. In addition, segmentation of the X-ray CT information can also introduce errors to the anatomical priors. The soft spatial priors method is not as susceptible to mismatches of the anatomical priors as it does not impose a rigid constraint on the reconstructed optical property maps. The ability of each of these algorithms to deal with inaccurate *a priori* information was tested by moving the assumed location of a 5 mm anomaly from the true location. This was tested using simulated data on a phantom identical to phantom #1 shown in Figure 4.14. The assumed location of the anomaly based on *a priori* information was shifted vertically in 1 mm steps, and reconstructed using both methods.

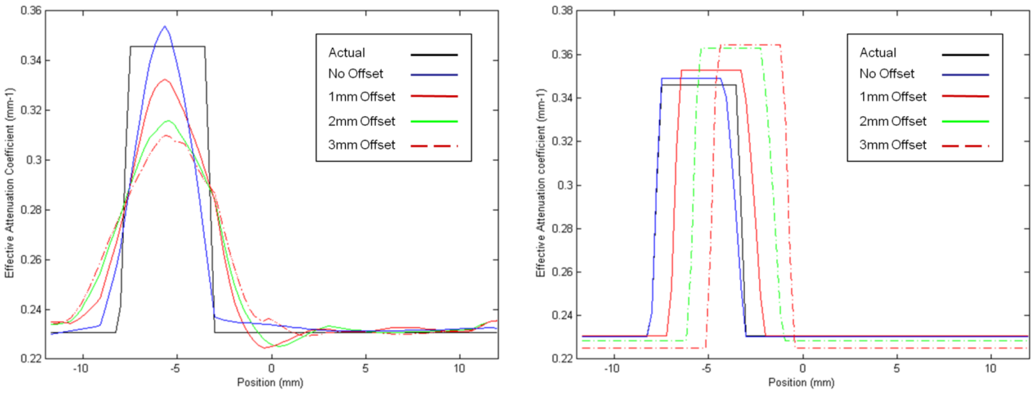

(a) **(b)**

Figure 4.6. Vertical profiles of the effective attenuation maps recovered using simulated forward data based on phantom #1 in **Figure 4.**14. The soft spatial method is found in (a), while the hard spatial method is found in (b) The assumed location of the anomaly is shifted incrementally by 1 mm in the vertical direction to represent mismatches between the assumed priors and the actual anomaly location.

The results are plotted in Figure 4.6. Vertical profiles of the reconstructed effective attenuation maps are shown for each shift in anomaly position. The soft spatial prior method results in accurate localization of the center of the anomaly up to an offset of 3mm. The recovered peak effective attenuation coefficient decreases steadily as the offset increases, while the background effective attenuation remains constant. As expected, the center of the anomaly is not recovered accurately with the hard spatial priors method; the center tracks with the assumed location of the anomaly. The effective attenuation of the anomaly itself increases with the *a priori* mismatch, while the background optical properties decrease slightly to compensate for the mismatch in boundary fluence. This data clearly demonstrates the advantages of the soft prior method when there is uncertainty in the spatial prior information. However, the hard prior method appears to be superior when the optical contrast is expected to match the *a priori* information, as in the case for test phantoms with distinct regions of uniform contrast.

4.3 Instrumentation

A schematic diagram of the integrated X-ray CT scanner and DOT system in shown in Figure 4.7a, and an image of the CCD camera is shown in Figure 4.7b. The optical imaging path was integrated into the shielded X-ray CT system with minimal modifications. A thermoelectrically cooled (-45 °C) CCD camera (DWN436-BV, Andor Technology), was added externally via an imaging port with a lead shielded sliding door with interlocks, and black fabric shield for external light rejection. The light source used for DOT imaging is a 635 nm diode laser (PRO Biophotonics) mounted externally and coupled into the enclosure via an optical fiber. A series of lenses is then used to focus the light source onto the subject surface with a 1.5 mm diameter spot size. Custom LabVIEW (National Instruments, Austin, TX) software programs were developed to allow automated control of the data acquisition with the system.

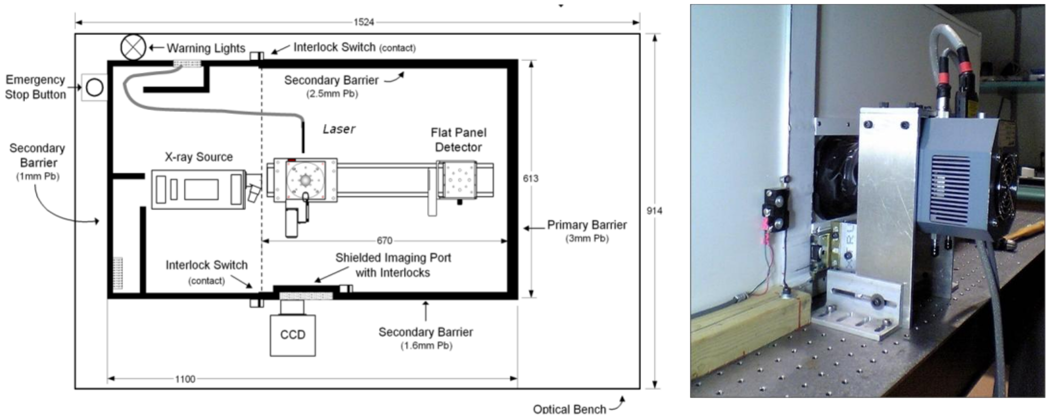

(a) **(b)**

Figure 4.7. Schematic diagram of the integrated DOT/X-ray CT system (a) and an image of the CCD camera attached via an imaging port on the lead shielded enclosure (b).

4.3.1 CCD Characterization

A thermoelectrically cooled CCD camera was used to acquire images of the surface emittance. The CCD used is a highly sensitive back-illuminated model with 2048 x 2048 pixels and 16 bit signal resolution. The CCD is coupled to a 50 mm Nikon lens with an 8 mm extension ring to decrease the focal distance of the lens. The primary sources of noise in a CCD camera are due to shot noise, readout noise, and dark noise. Shot noise is due to the statistical variation in the rate at which photons arrive at and interact with the CCD's semiconductor material. In general, CCD shot noise follows a Poisson distribution and is the dominant source of noise in most applications because it is a function of the intensity of the incident light. The exception however is in low light applications; in this scenario readout noise, or noise produced during the analog-to-digital conversion is dominant.

The dark current noise is due to thermally generated electrons within the semiconductor substrate. The dark current noise can be decreased by cooling the CCD and the repeatable constant signal portion can be subtracted from the image data. Typically, the noise performance of a CCD detector is characterized by the signal-to-noise ratio which can be calculated according to the formula, $SNR = \mu/\sigma$, where µ is the average counts per pixel, and σ is the standard deviation of the counts. Figure 4.8 shows the signal to noise ratio of the CCD as a function of temperature. Dark image subtraction was performed for all CCD measurements. The maximum signal to noise ratio is reached at a temperature of -30 ºC. Therefore all images have been acquired at a temperature of -45 ºC where readout noise dominates.

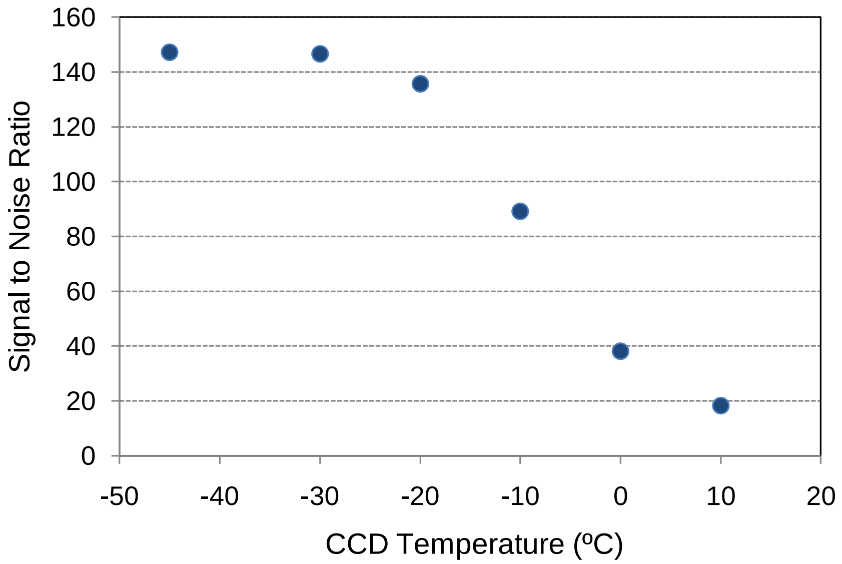

Figure 4.8. The signal-to-noise ratio of the CCD as a function of temperature. The data was collected by imaging the output of an integrating sphere with a power of 5 nW/cm2 and a 240 s integration time.

The signal-to-noise ratio was also measured as a function of exposure (see Figure 4.9). The integration time and light power were varied from 1 to 120 s and 1 to 10000 nW/cm^2 respectively. As expected, the SNR increases linearly with square of the exposure. These results indicate the importance of maximizing the detected signal and minimizing the integration time for all subsequent measurements.

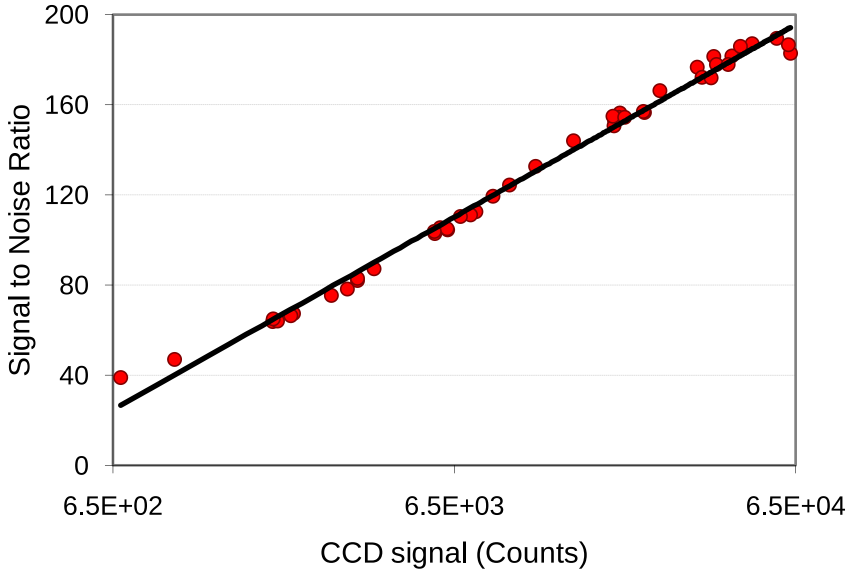

Figure 4.9. The signal-to-noise ratio as a function of signal for various combinations of integration time (1 to 120 s) and light fluence (1 to 10000 nW/cm^2).

Finally, the CCD was calibrated such that the detected signal could be related to incident power per unit area. Measurements were performed using an integrating sphere and a filtered light source at wavelengths ranging from 560 to 640 nm. The output port of the integrating sphere was positioned in the plane typically used for surface emittance measurements. The results in Figure 4.10 show that the CCD response is linear over 4 orders of magnitude in source power.

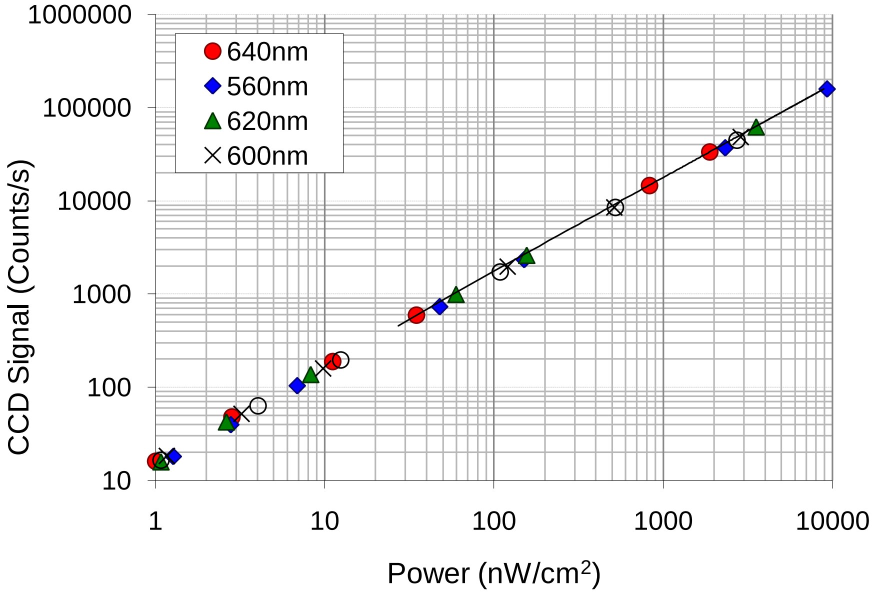

Figure 4.10. Absolute calibration curve of the CCD camera performed at multiple wavelengths. The power in nW/cm^2, was measured using a calibrated optical power meter (model 840, Newport Corp.) at the output port of the integrating sphere.

4.3.2 Data Collection

The surface data used for the DOT reconstructions was imaged onto the CCD camera after careful alignment of the CCD with the rotation stage and light source. The system is aligned such that the 635 nm laser source, rotation stage, and subject are all centered on the 2048 x 2048 pixel CCD. The image of the subject encompasses approximately the middle 10 % of the CCD, eliminating the distortions caused by the macro lens. The lens aperture was set to F/5.6 to maximize light collection efficiency, while maintaining a large enough depth of field to keep the subject surface in focus. A single image was acquired for each source position and the resulting images were processed in Matlab to extract the relevant virtual detector data used in NIRFAST. A typical raw CCD image is shown Figure 4.11a. Usual imaging times were 1 to 2 seconds.

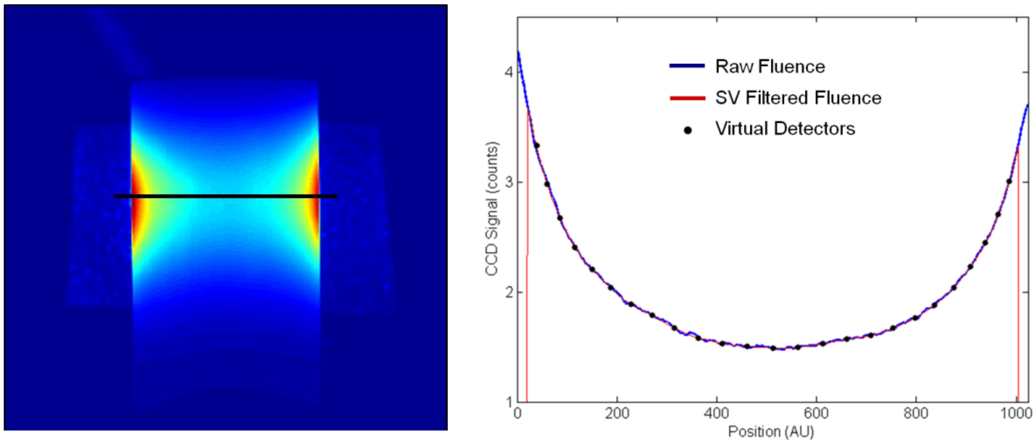

(a) **(b)**

Figure 4.11. The data collection procedure is summarized in this figure. (a) shows a raw CCD image collected from a cylindrical test phantom. The diode laser is focused on the opposite side of the cylindrical phantom as shown by the red dot in Figure 4.2f. A profile of the surface fluence is taken (depicted by the horizontal line here, and blue x's in Figure 4.2f) and processed to yield the virtual detector data (b).

The virtual detector data was extracted using a multi-step procedure shown in Figure 4.11. First, a 7 pixel wide horizontal slice of the raw CCD image was averaged resulting in a profile of boundary fluence through the subject. An edge finding routine is used to find the extreme left and right edges of the subject and used to center the profile data. The profile is then interpolated and filtered using a Savitzky-Golay filter (103) to remove noise in the surface fluence due to surface imperfections. The Detector locations are then extracted from the filtered profiles and calibrated using the data calibration procedure described in the next section.

4.3.3 Data Calibration

An important but under-appreciated step in an image reconstruction method is the calibration and other practical considerations necessary for the use of experimentally-acquired data. In our reconstruction algorithm, several unknowns such as source-strength, numerical imprecision due to finite mesh spacing, and data-model mismatch can lead to large artifacts in reconstruction if these effects are not properly accounted for.

The boundary fluence data obtained from a test phantom (heterogeneous) is calibrated relative to a homogenous reference phantom with known optical properties. The optical properties of the homogeneous reference phantom were measured on a steady-state diffuse reflectance system (89, 90). The phantom is composed of epoxy resin with India ink for absorption and titanium dioxide for scattering as described in detail in Chapter 3. The optical properties of the reference phantom are chosen to closely match the estimated global homogeneous optical properties of the test phantom as closely as possible.

The homogeneous reference phantom is imaged in the same geometry as the subject, but using fewer source positions (typically 8) yielding $\Phi^{i}_{meas(hom)}$. These eight measurements are then averaged to produce one measurement for the reference phantom:

$$\Phi_{mean(\text{hom})} = \frac{1}{NS}\sum_{i=1}^{NS} \Phi^{i}_{meas(hom)} \tag{4.11}$$

where NS is the number of sources, and *i* is the measurement number. Next, the expected boundary fluence of the reference phantom is calculated using the optical property values measured with the spatially resolved diffuse reflectance system, Φ^{i}_{calc}, and these value are averaged to reduce noise. The heterogeneous phantom is now measured yielding the measurement boundary fluence data $\Phi^{i}_{meas(het)}$. Two different calibration methods were tested. The first involves dividing the measured heterogeneous data, $\Phi^{i}_{meas(het)}$ by the measured homogenous data, $\Phi^{i}_{mean(hom)}$ data and scaling by the calculated fluence generated by the forward model, Φ^{i}_{calc} as follows:

$$\Phi_{cal}^{i} = \frac{\Phi_{meas(het)}^{i}}{\Phi_{mean(\mathrm{hom})}} \cdot \Phi_{calc(hom)}^{i} \tag{4.12}$$

The second method employed is reported by Kepshire *et al*. and is calculated as follows (104):

$$\Phi_{cal}^{i} = \frac{\dfrac{\Phi_{meas(het)}^{i}}{\max\left(\Phi_{meas(het)}^{i}\right) - \min\left(\Phi_{meas(het)}^{i}\right)}}{\dfrac{\Phi_{mean(\mathrm{hom})}}{\max\left(\Phi_{mean(\mathrm{hom})}\right) - \min\left(\Phi_{mean(\mathrm{hom})}\right)}} \cdot \Phi_{calc(hom)}^{i} \tag{4.13}$$

Each of these calibration methods was tested by comparing the resulting calibrated heterogeneous data to the expected boundary fluence calculated in NIRFAST. In this case the true optical properties of the test phantom and the anomalies within the phantom were measured using steady-state spatially resolved diffuse reflectance. These measured values were then input into the forward model to arrive at the simulated fluence curve. The "ratio" calibration method from equation 4.12 does not match the expected boundary fluence values very well. The "dynamic range" method of equation 4.13 results in a better fit to the expected simulated values. Following the data calibration procedure, Φ_{cal}^{i}, is ready to be used directly in the inverse reconstruction algorithm.

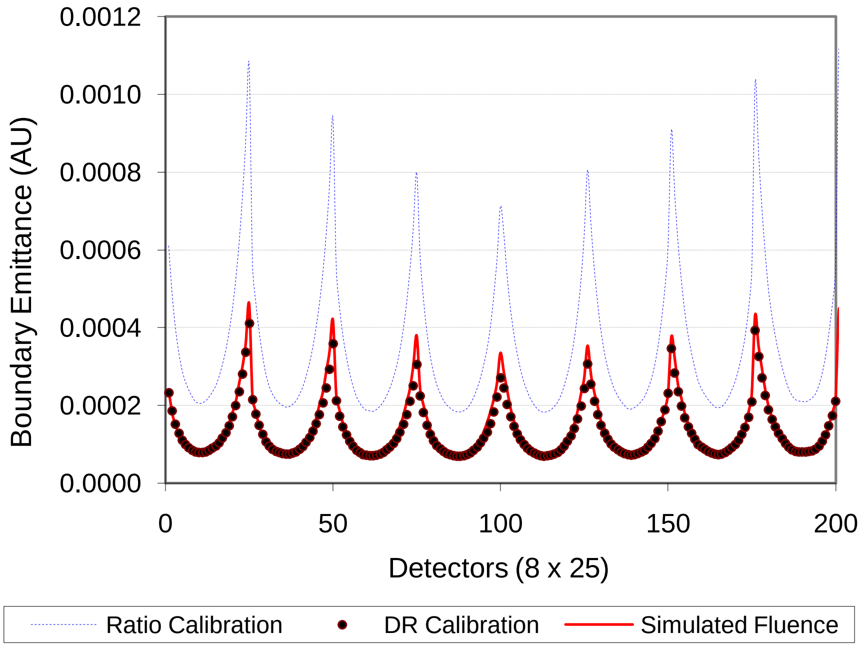

Figure 4.12. Comparison of the two data calibration methods. The "ideal" boundary emittance simulated by NIRFAST is depicted by the solid curve at 25 detector locations and 8 views for a total of 200 data points. The calibrated experimental boundary data are depicted by the dashed curve (4.12) and the solid dots (4.13).

4.3.4 Initial Guess

The image reconstruction algorithm starts from an estimated set of optical properties that are iteratively updated based on the difference between the calculated forward data and measured boundary fluence data. If the initial estimate of the optical properties is far from the actual optical properties of the heterogeneous object being imaged, the convergence of the algorithm is significantly slowed and can even lead to erroneous reconstructions. The initial optical property estimate is determined by finding an estimate of the "bulk" or "homogeneous" optical properties that best match the measured heterogeneous data. This is accomplished by using an iterative algorithm beginning with μ_a = 0.01 mm^{-1} and μ_s' = 1 mm^{-1} and incrementally increasing or decreasing each value by 0.5 % until the difference between the homogenous estimate and measured heterogeneous boundary data is minimized.

4.3.5 Mesh Generation

Simple two dimensional FEM meshes are readily generated by the NIRFAST software package, however these meshes do not contain any *a priori* region information. While region information could be added to these meshes using segmented CT data, the boundaries of the segmented regions are not likely to match the geometrical distribution of nodes in the FEM mesh. A customized program was written in Matlab to create accurate 2D FEM meshes from X-ray CT images. The program features an interactive segmentation component as well as an FEM generator created by Shewchuk (105). An illustration of the mesh generation procedure is shown in Figure 4.13. The CT data are co-registered to the optical data by acquiring the optical and X-ray data sequentially without moving the subject.

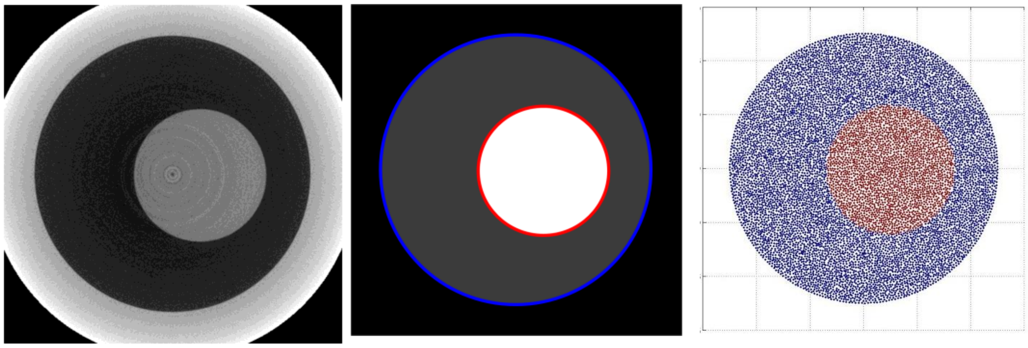

(a) **(b)** **(c)**

Figure 4.13. The FEM mesh generation procedure. (a) shows a raw X-ray CT slice prior to segmentation. (b) contains a segmented image depicting the two segmented regions and (c) shows the nodes of the FEM mesh generated by the meshing algorithm .

4.4 Experiments

4.4.1 DOT Reconstruction Method Evaluation

A set of experiments was performed to examine the optimal strategy for incorporating the *a priori* anatomical information into the DOT reconstruction algorithm. Four different strategies have been explored. The first two methods do not use any spatial priors at all but explore the two different minimization schemes presented in section 4.1. Reconstructions were performed using the modified Levenberg-Marquardt (LM) method where the regularization parameter, λ, is reduced during each iteration. The second non-spatial prior method uses the single-step Tikhonov method where λ is fixed at its initialized value for all iterations. The final two methods used are the hard spatial priors and soft spatial priors methods described earlier.

The experiments were performed using a set of cylindrical tissue simulating phantoms with a diameter of 25 mm. The phantoms were composed of epoxy resin (Araldite GY502 & Aradur 837, Huntsman Corp.), India ink and titanium dioxide. Anomalies were added by machining cylindrical cavities in the epoxy resin and filling the voids with a liquid Intralipid (IL 20% Pharmacia Corp.) solution containing India ink to alter the absorption properties. The optical properties of each phantom, including the epoxy resin and Intralipid solutions were measured using the previously described steady-state spatially resolved reflectance system.

Phantom with four geometries were fabricated for these experiments. The first phantom contained a single anomaly with a diameter of 5 mm, with increased absorption and scattering coefficients. The second phantom contained two 5 mm anomalies, one of which had a 100 % increase in absorption above background and the other, a 100 % increase in scattering. The third phantom was composed of one large region of increased scattering and absorption, while the last phantom was identical, except for the addition of a third region, 5 mm in diameter, with decreased scattering and absorption inside the larger region. The configuration of each phantom is shown in Figure 4.14a and the optical properties of each region are summarized in Figure 4.14b. For this set of experiments the reference phantom was a homogeneous cylindrical phantom, 25 mm in diameter, with μ_a = 0.011 mm^{-1} and μ_s' = 1.6 mm^{-1}.

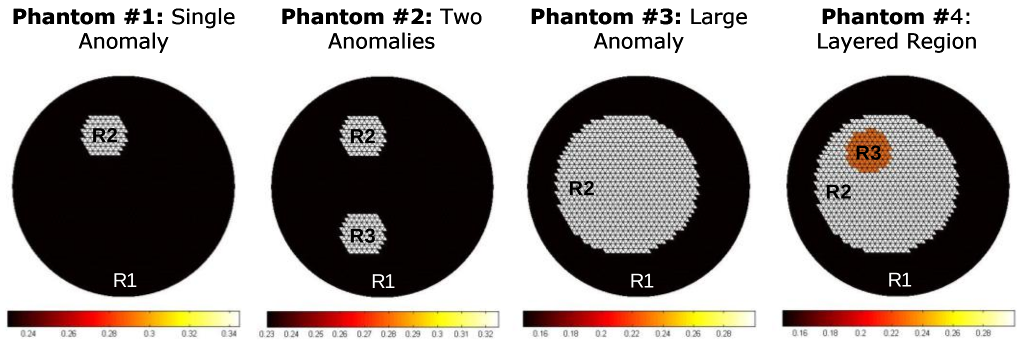

(a)

	Phantom #1			Phantom #2			Phantom #3			Phantom #4		
	μ_a	μ_s'	μ_{eff}	μ_a	μ_s'	μ_{eff}	μ_a	μ_s'	μ_{eff}	μ_a	μ_s'	μ_{eff}
Region 1	0.011	1.60	0.23	0.011	1.60	0.23	.0075	0.98	0.15	.0075	0.98	0.15
Region 2	0.017	2.41	0.35	0.022	1.60	0.33	0.015	1.96	0.30	0.015	1.96	0.30
Region 3	-	-	-	0.011	3.19	0.33	-	-	-	0.011	1.60	0.23

(b)

Figure 4.14. Target optical properties for the four test phantoms. (a) shows the spatial distribution of the regions in each phantom, while the table in part (b) summarizes the optical properties of each region.

For these reconstructions the FEM meshes were generated using the uniform meshing algorithm contained in the NIRFAST software package. The FEM mesh consisted of 1785 nodes and 3419 elements with uniform nodal density. The *a priori* spatial information was added manually based on the known geometry of each test phantom. The imaging geometry consisted of 25 virtual detectors, arranged in a 135 degree fan beam geometry as described earlier, and 16 sources positions were used. The initial bulk homogeneous guess of optical properties was calculated using the methods described in section 4.3.5. The regularization parameter was set to 10, and the reconstruction basis was a 50 x 50 uniform Cartesian grid. Reconstructions were iterated until the difference between the forward data and the reconstructed data did not improve by more than 2% when compared with the previous iteration. Figure 4.15 shows reconstructed images of the four test phantoms using the four different reconstruction techniques. Profiles of the effective attenuation coefficient for each phantom are shown in Figure 4.16, while the percent root-mean-squared (RMS) error of the reconstruction is depicted in Figure 4.17.

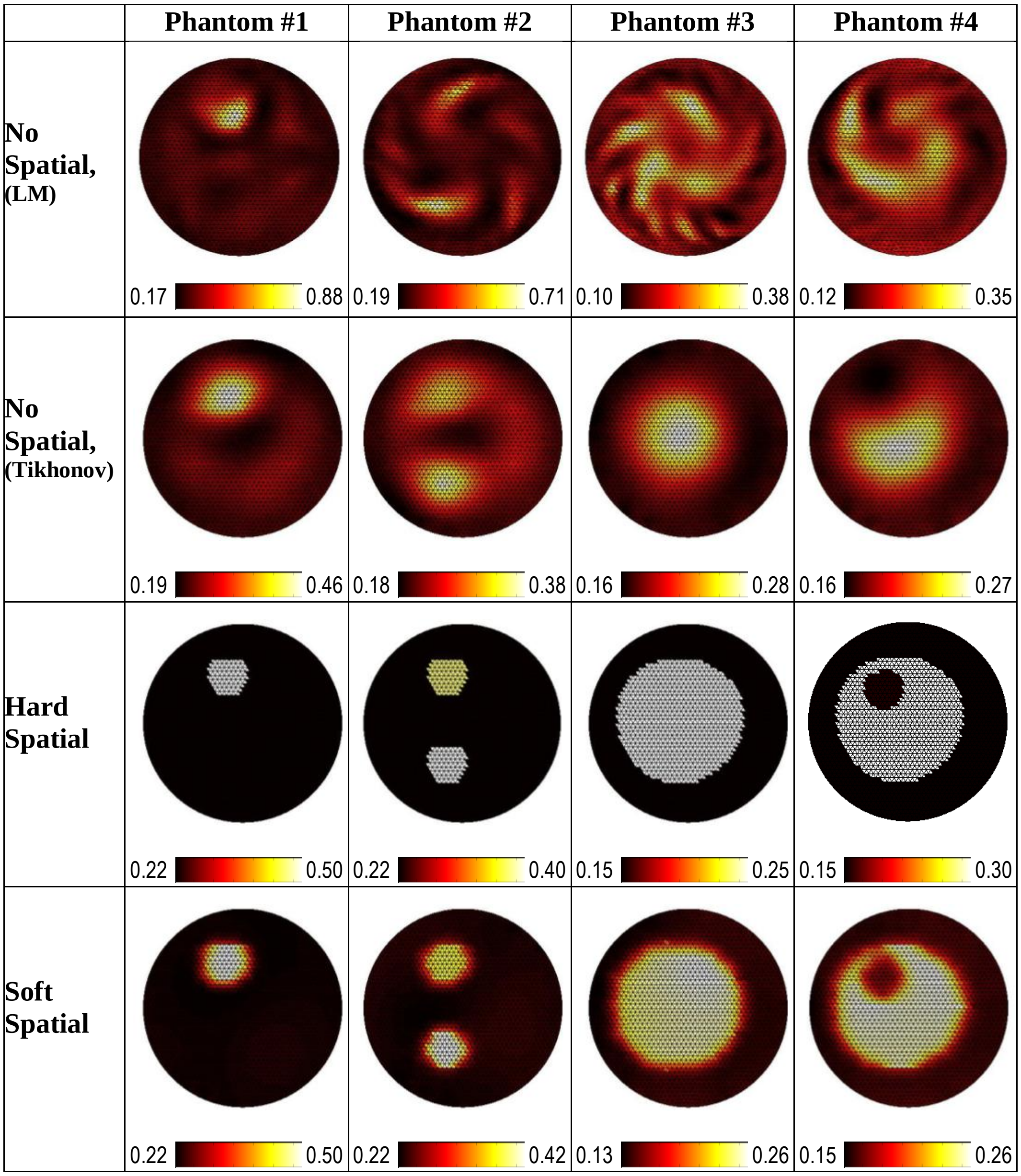

Figure 4.15. Reconstructed images of the effective attenuation coefficient in the four test phantoms using the four different reconstruction techniques.

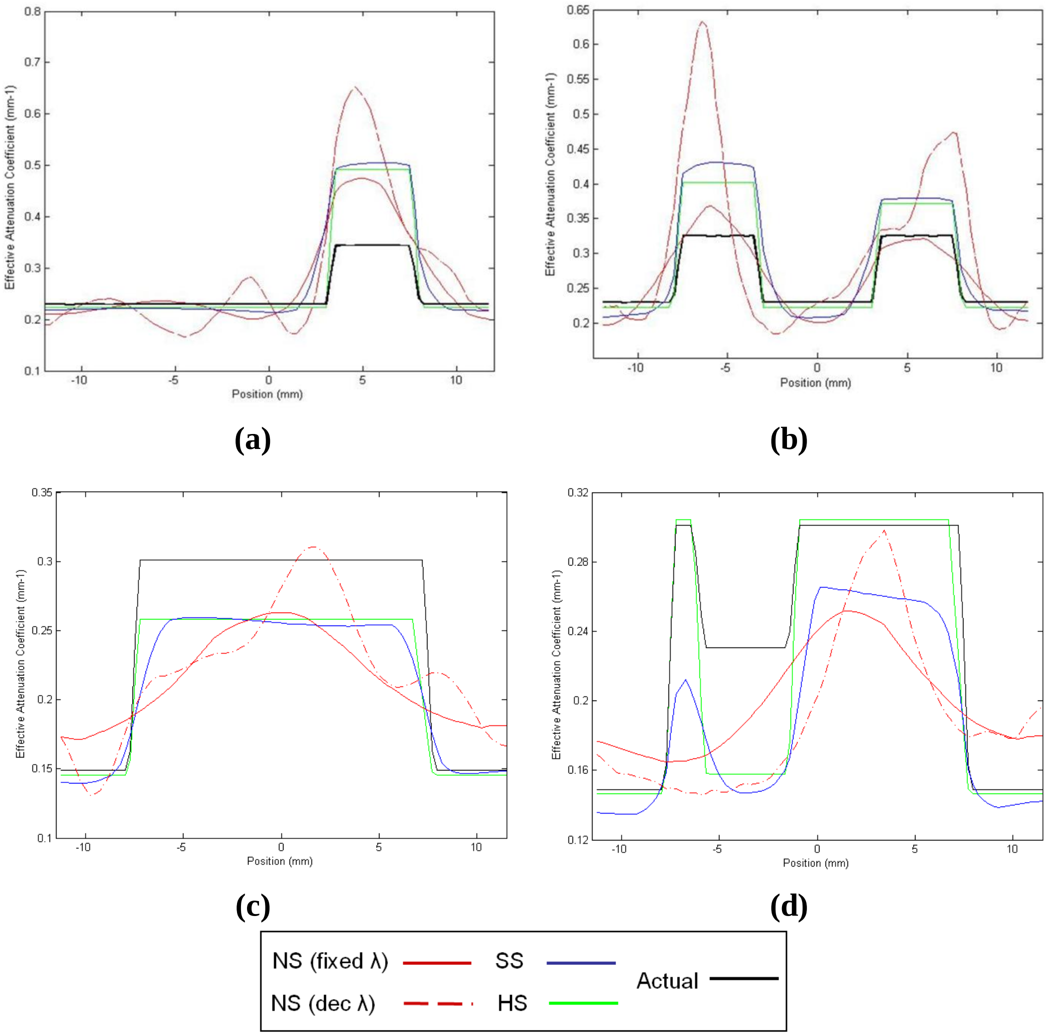

(a) (b)

(c) (d)

Figure 4.16. Profiles of the effective attenuation coefficient are shown for each test phantom. (a) contains a vertical profile through the center of the single anomaly in phantom #1. (b) is a vertical profile through the center of both anomalies in phantom #2 (same geometry as (a)). (c) contains the vertical profile through the center of region 2 of phantom #3, while (d) shows the identical profile in phantom #4. The reconstruction methods are labeled as follows: NS (fixed λ) – single-step Tikhonov, NS (dec λ) – modified Levenberg-Marquardt, SS – soft spatial method, HS – hard spatial method, and Actual – measured from steady-state spatially resolved diffuse reflectance.

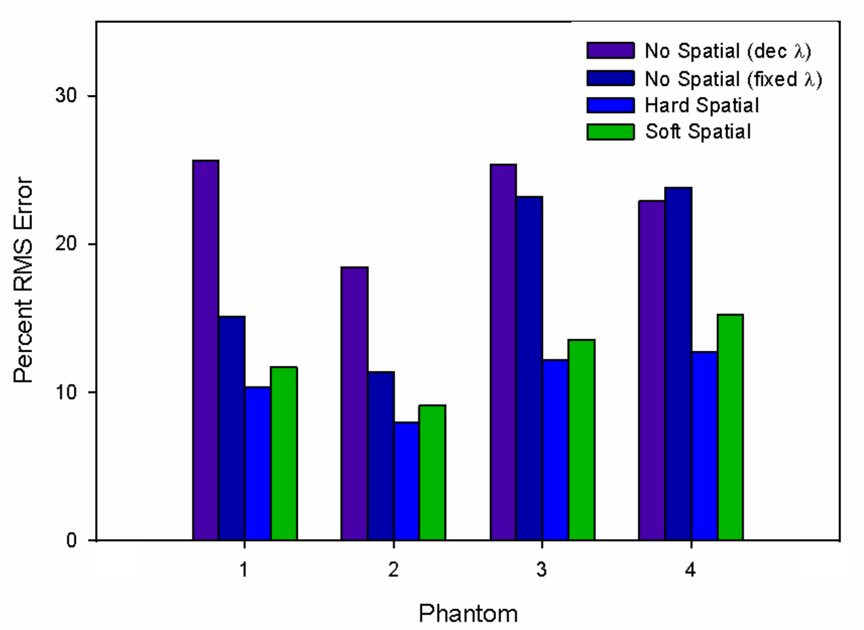

Figure 4.17. The total percent RMS errors of the recovered effective attenuation maps.

The results show that the spatial priors improve the reconstructed image quality dramatically. The hard and soft priors methods generate smoother images resulting in smaller standard deviations from the true effective attenuation values as compared to the reconstruction that do not incorporate any spatial prior information. Visually, the repeated single-step Tikhonov iterative technique results in smoother images than the modified LM method. This is due to the decreasing regularization parameter in the LM method. As λ decreases during iteration, the algorithm is forced to place more trust in the measured data, resulting in an amplification of any errors present in those data. The modified LM method suffers from large spiral-like artifacts which dominate the reconstructed images. Only phantom #1 with the single anomaly bears a resemblance to the actual optical property distribution. The Tikhonov technique results in images that are visually close to the actual optical property distributions, but still contain non-uniform background optical properties. As expected, the hard spatial priors method results in uniform recovery of the effective attenuation coefficient within each region by design. Visually, all the hard prior images are very similar to the actual optical property distributions, and match the absolute values closely. The only obvious deviation from the actual values is seen in the recovery of the 5 mm anomaly in phantom 4 where the effective attenuation is considerably underestimated. The soft spatial prior method also results in visually accurate recovery of the optical property distribution, but without the sharp boundaries between regions of different optical properties.

Further information can be gained by looking at Figure 4.16, which contains profiles of the images taken through the center of the anomalies of each phantom. Here we can see that there is a tendency to overestimate the effective attenuation coefficient of the anomalies in the first two phantoms, while the larger regions found in phantoms 3, and 4 are significantly underestimated by all methods except the hard priors method in phantom 4. In phantom 1, the anomaly peak effective attenuation is overestimated by 85 % by the LM algorithm, while the Tikhonov, hard prior, and soft prior methods do significantly better at 37 %, 40 % and 43 % respectively. The background values are recovered accurately for both spatial priors methods, while the LM and Tikhonov methods exhibit oscillation in the background values. The results are very similar for phantom 2. In this case the effective attenuation of the anomalies is also overestimated by all reconstruction methods; however the magnitude of the overestimation is lower for the Tikhonov and spatial prior methods. Also of note here is the more accurate recovery of the attenuation of the purely absorbing anomaly as compared with the purely scattering anomaly. The effect has been seen earlier in the simulations found in section 1.2 and seems to be an inherent property of the reconstruction algorithm to deal with changes in absorption more accurately than scattering.

The large anomaly found in phantom 3 is recovered more accurately than the previous two cases. This time the effective attenuation coefficient is underestimated by approximately 15 % by all algorithms except the modified LM method. The limitation of all four algorithms is illustrated in phantom 4. Here, region 2 is recovered within 15 % using the LM and soft prior method, whereas the hard spatial priors method and Tikhonov method are both within a few percent of the actual effective attenuation. The significant result here is the recovery of the 5 mm anomaly within region 2. The effective attenuation of the anomaly is underestimated by ~50 % by all reconstruction methods. This seems to be an inherent limitation of the techniques presented here. The algorithms do not perform as well in layered domains containing regions of lower attenuation.

Figure 4.17 provides an effective mean of summarizing the results presented here. The trends in the percent RMS errors mirror the visual observations made using the images in Figure 4.15, and the profiles in Figure 4.16. Examining the RMSE of the test fields confirmed that the Tikhonov method outperformed the modified LM method in almost all test cases. However, both imaging algorithms had difficulty with the layered domain, which was also the most realistic test field, and RMSE errors were relatively high for these images.

Overall the two methods employing the a priori spatial information performed better than the algorithms not using spatial priors. The hard prior methods resulted in the most accurate recovery of the effective attenuation distribution in all test phantoms. An additional advantage of the hard prior technique was the increased speed of convergence due to the reduced number of free parameters in the reconstruction algorithm.

There are several sources of error in these experiments that should be minimized in future experiments. These include alignment inaccuracies between the FEM meshes used for the reconstruction and the physical orientation of the phantom during imaging. These errors can be minimized by using actual X-ray CT priors during mesh generation, as is done in Chapter 5. Another major source of error is the reference phantom that is used to calibrate the experimental data. Data calibration is an essential step; however any errors in the determination of the optical properties of the reference phantom can result in inaccurate data calibration and subsequently inaccuracies in the recovered images. Also, any inhomogeneities in the reference phantom will also result in inaccurate data calibration. Possible solutions are to use an alternative method to measure the optical properties of the reference phantom, and using a phantom with more uniform optical properties. Ideally the calibration step would be performed using the DOT system itself via an absolute calibration of the source used for DOT. Other research using frequency domain systems employ this self calibration technique (48), which is much easier to implement when phase data are also available.

4.4.2 Spectral Reconstruction

An experiment was performed to examine the ability of the spectral reconstruction algorithm to recover consistent estimates of the scattering coefficient. A problem with reconstructions of the optical properties at independent wavelengths is that the lack of phase information results in varying ratios between the absorption and scattering coefficients that are not reflective of physical conditions. The details of the optical properties and geometry of the phantom used here is described in detail in Chapter 5 (Figures 5.6 and 5.7). Briefly, an epoxy phantom, 25 mm in diameter, with a single anomaly was imaged using identical conditions to section 4.4.1. The forward mesh consisted of 9560 nodes and 18835 elements. The reconstruction basis was a 50 x 50 grid of uniform Cartesian Grid. The spectral algorithm was implemented using the soft spatial priors method and the optical properties reported are the average of all the background nodes in the phantom at each wavelength.

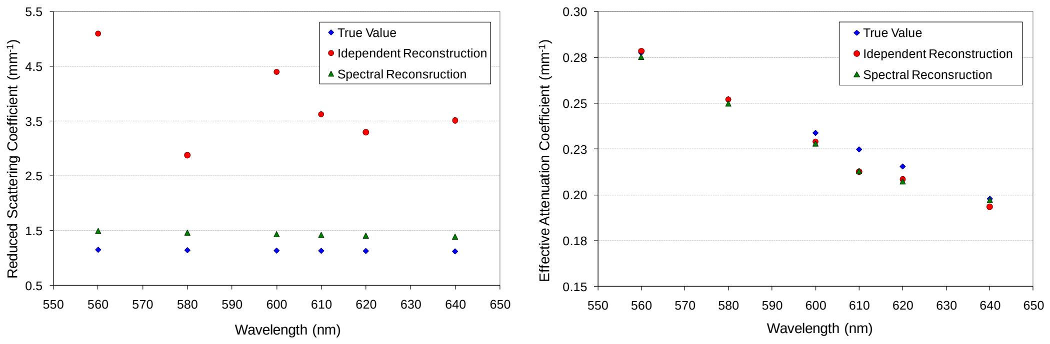

(a) **(b)**

Figure 4.18. Reconstructed optical properties at multiple wavelengths (560, 580, 600, 610, 620, and 640nm) using an independent reconstruction algorithm and spectral reconstruction algorithm. (a) shows the scattering coefficient as a function of wavelength, while (b) contains the effective attenuation coefficients.

The results show a dramatic improvement in the consistency of the scattering coefficients. Independent recovery of the optical properties resulted in scattering coefficients varying over a large range from 2.7 mm^{-1} to 4.2 mm^{-1}. The scattering coefficients recovered using the spectrally constrained algorithm track much more closely with the true values measured using spatially resolved diffuse reflectance, while the effective attenuation coefficients remain almost identical to the unconstrained reconstructions. The effective attenuation recovered using both methods matches well with the true values.

4.5 Concluding Remarks

An integrated DOT/X-ray CT system has been constructed and characterized. The DOT system uses a non-contact CCD camera to acquire surface fluence measurements, and a finite element model of the propagation of light in tissue to recover the internal optical property distribution of a test subject. *A priori* spatial information from the X-ray CT is used to constrain the DOT reconstruction algorithm. A set of simulations was used to determine the optimal source detector geometry for the DOT system. Four image reconstruction algorithms were evaluated for their ability to recover the effective attenuation coefficient of a series of test phantoms. Two of the algorithms (a modified LM method, and a single-step Tikhonov method) did not use any *a priori* spatial information. Two other algorithms (hard priors and soft priors) used *a priori* structural information to constrain the reconstruction process. In addition, a spectrally constrained algorithm was described that is useful for multi-wavelength reconstructions.

The results indicate that the inclusion of spatial priors improves the reconstructed image quality dramatically. The hard priors and soft priors methods result in similar recovered optical property distributions, but the soft priors case is more resilient to imperfect *a priori* information. The spectrally constrained algorithm was successful at removing the fluctuations in reconstructed scattering properties of non-spectrally constrained methods.

Chapter 5

Multispectral Bioluminescence Tomography

This chapter describes the development and evaluation of an integrated BLT/DOT/X-ray CT system. The BLT system is used to estimate bioluminescence distributions, while using *a priori* background optical properties recovered using the DOT system described in Chapter 4. This chapter contains a description of a multispectral bioluminescence reconstruction algorithm based on a finite element model of light propagation in tissue. The accuracy of the proposed bioluminescence reconstruction algorithm is demonstrated and validated using simulated and experimental multispectral measurements. The optimal strategy for incorporating the *a priori* background optical property distribution from the DOT system is examined using a set of experiments with a tissue-simulating phantom and simulated bioluminescence source.

5.1 Reconstruction Algorithm

The inverse problem in BLT is very similar to DOT in that it requires a suitable forward model for the propagation of light in tissue. For the purposes of BLT, the diffusion equation reviewed in Chapter 1 is re-formulated to yield (44):

$$-\nabla \cdot \kappa(\mathrm{r})\nabla\Phi(r) + \mu_a\Phi(r) = B(r) \tag{5.1}$$

where *B(r)* is an internal bioluminescence source, $\Phi(r)$ is the photon fluence at position r, and $\kappa(r)$ is the diffusion coefficient defined as $\kappa(r) = 1/3(\mu_s' + \mu_a)$.

The fluence rate data are represented by an operator which is linear with respect to the bioluminescence source. The absorption and scattering coefficients can be assigned or can be determined from separate measurements and reconstructions via the DOT system. The BLT image reconstruction problem is now established as a solution to the minimization of:

$$\hat{\chi} = \min_{\mu_a,\kappa}\|(\mathrm{y} - \mathrm{F}[\mathrm{B}(\mathrm{r})])\| \tag{5.2}$$

where *y* are the measured boundary data, *F*[*B*(*r*)] are the data calculated from equation 5.1 with an estimate of the internal bioluminescence, and $\| \; \|$ is the weighted L2 norm, which represents the square root of the sum of the squared elements. The recovery of the internal bioluminescence distribution is an ill-posed problem much like recovery of optical coefficients in DOT. In the absence of any *a priori* information on *B(r)*, both the source strength and spatial distribution must be determined. However, an advantage in the BLT formulation is that the measured parameter, the photon fluence rate, is linear with *B*(r). Thus, the problem can be solved by constructing the image of the bioluminescence source as a sum of basis distributions whose weights are estimated from the measured boundary data (44). The linearity of the bioluminescence model can be utilized by creating a set of independent basis solutions for the source:

$$B = \sum_{i=1}^{N} a_i b_i \tag{5.3}$$

where the coefficients a_i are the weight functions for multiple unit sources b_i at each node i in the model containing a total number of nodes N. The size of $b(r)$ is reduced by defining a separate reconstruction basis (as in the inverse DOT problem), upon which the unknown parameters are updated. A regularly spaced Cartesian pixel basis is used for the recovery of source strength and position. Substituting equation 5.3 into equation 5.2 and solving for a using a least-squares approach results in a single-step linear expression:

$$a = W^T(WW^T + \lambda I)^{-1} y \tag{5.4}$$

where W is a sensitivity matrix containing the solution of equation 5.1 for all possible source positions, y are the measured boundary data, λ is a regularization parameter, and I is the identity matrix. Although the Hessian matrix WW^T is invertible, the use of the regularization parameter, λ, becomes necessary in the presence of noise. The magnitude of the regularization parameter can have a profound effect on the recovered bioluminescence distribution. For simulations, λ set to 0.01 % of the maximum of the diagonal of the Hessian matrix provided optimal results. However, for experimental data, the ideal λ for one set of measurements was often not the best choice for another set. Thus, for experimental data, the reconstructions were performed using a range of regularization parameters and the source distribution having the lowest projection error (χ^2 in equation 5.2) was saved.

Upon inversion of equation 5.4, some of the weight coefficients (a_i), result in negative values which are not physically relevant to the reconstruction problem. The weight coefficients are restricted to positive values by iteratively solving equation 5.4 and eliminating nodes from the permitted source distribution having weights less than a predetermined value. This method is similar to algorithms described by Dehghani *et al*. (106) and Kuo *et al*. (107). The iteration proceeds until all weight coefficients are greater than the set value which is some percent of the peak source strength. In this work the cutoff value for the weight coefficients was set at 10 % of the maximum source strength at each iteration. This value was found to give the best balance between the convergence of the algorithm and realistic source distributions. In general, larger values resulted in better rejection of ring artifacts, and faster convergence, but were more prone to result in inaccurate source positions.

The single wavelength solution of the BLT problem is non-unique. Typical single wavelength solutions result in a superficial source distribution along the boundary (44). A solution to the non-uniqueness is to use boundary data from multiple wavelengths to constrain the possible bioluminescence distribution. Multi-wavelength BLT combines data sets measured from the same domain containing the same bioluminescence distribution over a range of usable wavelengths such that:

$$\mathrm{a} = \widetilde{\mathrm{W}}^{\mathrm{T}}\left(\widetilde{\mathrm{W}}\widetilde{\mathrm{W}}^{\mathrm{T}} + \lambda\mathrm{I}\right)^{-1}\tilde{\mathrm{y}} \tag{5.5}$$

where $\widetilde{W} = [W_{\lambda 1}; W_{\lambda 2}; W_{\lambda 3}; \cdots; W_{\lambda n}]$ are the weight matrices of all *n* wavelengths and $\tilde{y} = \lfloor y_{\lambda 1}; y_{\lambda 2}; y_{\lambda 3}; \cdots; y_{\lambda n} \rfloor$ is the corresponding measured boundary data for all wavelengths. The solution a is a weight vector corresponding to the number of unknowns that define the bioluminescence source distribution.

5.2 Simulations

5.2.1 Multispectral Simulations

To demonstrate the non-uniqueness of the BLT image reconstruction problem a 2D reconstruction of a centrally located bioluminescence source (radius = 2 mm, strength = 3.32) is shown in Figure 5.1. The simulations were performed on a homogeneous 2D circular mesh with a radius of 12.5 mm, and 3974 nodes. The internal bioluminescence was reconstructed from simulated boundary data at 64 detector positions spaced equally around the external boundary of the mesh. Forward data were generated at two wavelengths with 2 % noise; wavelength 1 has μ_a = 0.01 mm^{-1} and μ_s' = 1 mm^{-1}, and wavelength 2 has μ_a = 0.02 mm^{-1} and μ_s' = 1.2 mm^{-1} for the optical properties at all points in the object.

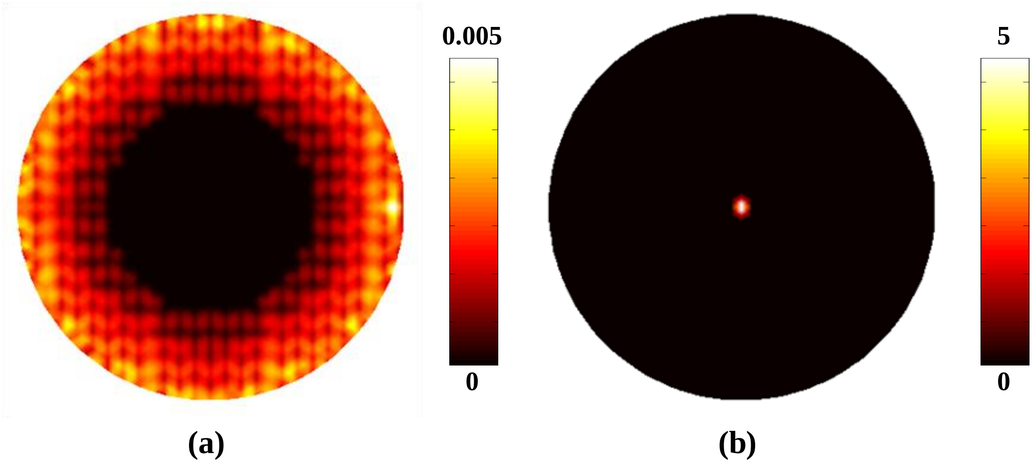

Figure 5.1. Reconstructed images of bioluminescence using (a) a single wavelength and (b) two wavelengths with 2 % added noise. The actual bioluminescence source is located in the center of the mesh, with a radius of 1mm and total strength of 3.3. Both BLT reconstructions were performed assuming perfect knowledge of the absorption and scattering coefficients.

Figure 5.1a shows a typical result for a single wavelength reconstruction, where it is evident that the source is recovered as a very superficial blur along the mesh boundary. Images reconstructed for the other individual wavelengths exhibit similar characteristics. The addition of a second set of boundary data at a different wavelength dramatically improves the accuracy of the reconstructed image. The source distribution reconstructed using two wavelengths in Figure 5.1b is exactly at the original target location while the source power is recovered to within 0.5 %. The improved multispectral image can be explained as follows. The photons emitted at the longer wavelengths undergo less attenuation than photons emitted at shorter wavelengths in tissue, resulting in a spectrum which depends on the depth of the bioluminescence source. The additional depth information provided by multispectral measurements results in improved depth reconstruction compared to single wavelength measurements. Incorporating additional data sets beyond two wavelengths further improves both the quantitative and qualitative accuracy of the reconstructed images in the presence of additional noise and experimental errors.

5.2.2 Effective Attenuation in BLT

The effect of variations in the ratio between the absorption coefficient and scattering coefficient on the BLT reconstruction is explored here. The DOT system and reconstruction algorithms described in Chapter 5 are effective at recovering accurate effective attenuation coefficients only, due to the continuous wave nature of the imaging system. The effects of scattering and absorption cannot be reliably separated and, as a result, the recovered absorption and scattering coefficients are not likely to match their true values. This can result in inaccurate recovery of internal source distributions, as the emittance is affected by the relative values of μ_a and μ_s' while holding the effective attenuation steady. Figure 5.2 shows the effect on the boundary flux in a homogeneous circular mesh, with a central source. As the absorption coefficient is increased, the boundary flux increases linearly despite the fixed effective attenuation. Fortunately, the effect on the boundary flux is small relative to changes in the effective attenuation coefficient itself. A 30 % error in absorption is equivalent to an approximately 10 % error in the effective attenuation coefficient.

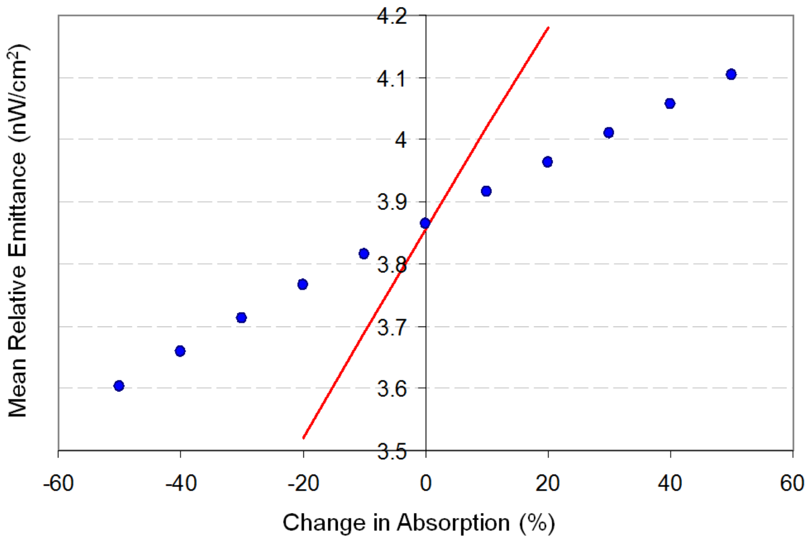

Figure 5.2. Variation in emittance versus changes in the absorption coefficient. The emittance from a homogeneous phantom containing a centrally located source is plotted as a function of changing absorption whilst holding the effective attenuation constant (dots). The solid line represents the change in emittance as a function of the change in effective attenuation.

While significantly smaller than the effects caused by changes in the effective attenuation, those due to the relative values of absorption and scattering still have the potential to negatively affect the recovery of internal source distributions. Simulations were performed using a 2D circular phantom as shown in Figure 5.4f with optical properties shown in Figure 5.4g at two wavelengths. A source with radius 0.5 mm and power of 1.5 nW/cm^2 was placed at the center of region 2 (x = -5mm, y = 0 mm). The boundary data were corrupted with 2 % noise. The effective attenuation at each wavelength and each region was held constant while the absorption coefficient was changed from -50 % of the true value to +50 % of the true value in steps of 10%. The results are contained in Figure 5.3.

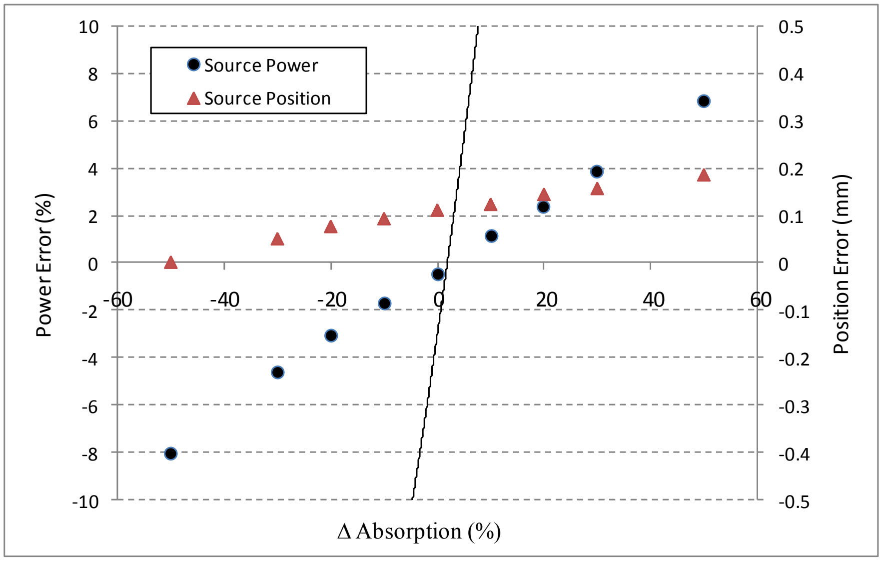

Figure 5.3. The effect of errors in background optical properties on BLT source recovery. The effect of changes in the absorption coefficient on source power and position are plotted while holding μ_{eff} constant. The black regression line plots source power error as a function of changing effective attenuation.

The best recovery of the source power occurred at ~0 % change in absorption as expected while the true optical properties produced an error of 0.1 mm in source position. The error in source position using the true optical properties is most likely due to discretization errors in the FEM mesh. Source power was recovered to within 8 % for the worst case of -50 % absorption, while the source location changed by a maximum of ± 0.1 mm. The errors in the source power with changing effective attenuation were much more dramatic as shown by the regression line in Figure 5.3. The results are encouraging as the errors in absorption from the spectral DOT reconstructions described in Chapter 4 rarely exceed 50 %, while an error of just a few percent in the effective attenuation coefficient result in similar deviations. Thus, the errors in the effective attenuation coefficient are the dominant source of error in the BLT source recovery.

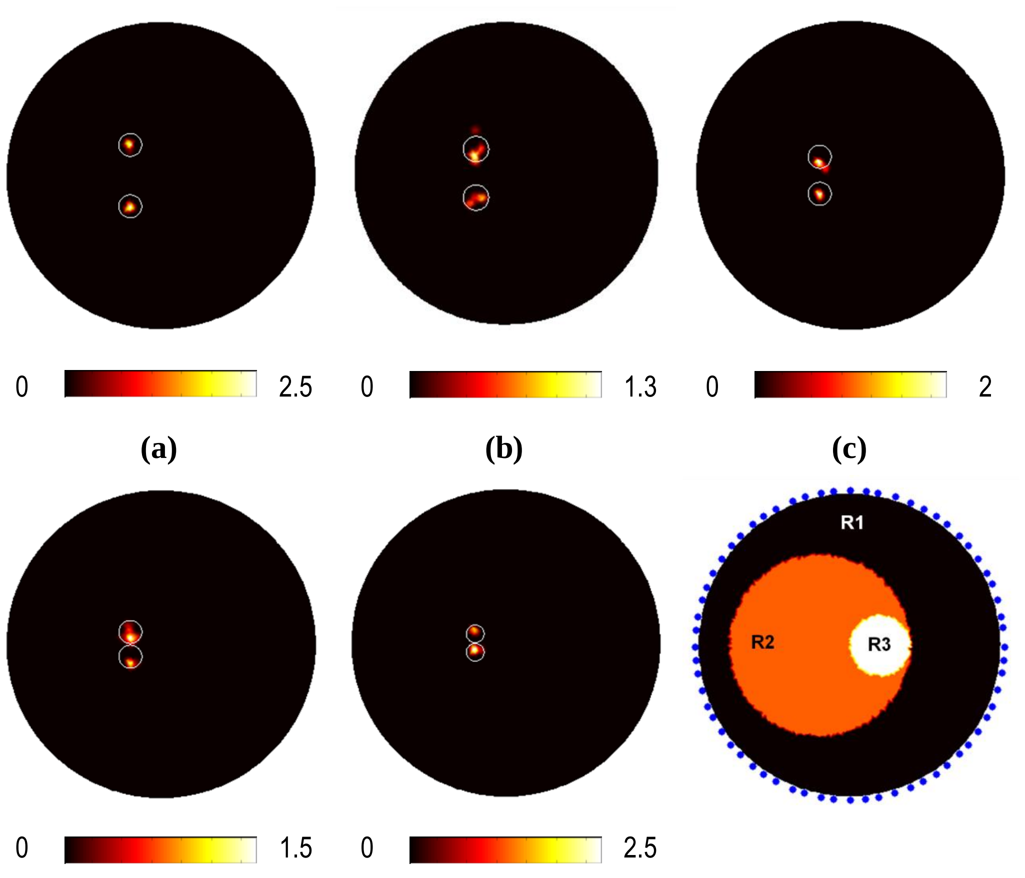

(a) (b) (c)

(d) (e) (f)

	Wavelength #1			Wavelength #2		
	μ_a	μ_s'	μ_{eff}	μ_a	μ_s'	μ_{eff}
Region 1	0.020	1.1	0.259	0.010	1.0	0.174
Region 2	0.025	2.0	0.390	0.020	1.5	0.302
Region 3	0.040	2.5	0.552	0.010	2.4	0.269

(g)

Figure 5.4. Reconstructed images of the bioluminescence sources at separations of (a) 5 mm, (b) 4 mm, (c) 3 mm, (d) 2 mm, and (e) 1.5 mm. (f) contains a model of the FEM mesh used including the distinct regions and detector locations, while (g) contains the optical properties in each region at both wavelengths used for reconstruction. The sources are 1 mm in diameter and their true locations are depicted by circles with a diameter of 2 mm (1.5 mm in (e)).

5.2.3 Source Resolution

The spatial resolution performance of the BLT algorithm was testing using a high resolution FEM mesh as shown in Figure 5.4f. The mesh has a diameter of 25 mm and contains three regions with optical properties shown in Figure 5.4g. The forward data were generated at two wavelengths on a fine forward mesh with 9560 nodes, 18835 elements, 64 uniformly spaced detectors, and 2 % added noise. The sources with radius 0.5 mm, were located at x = -2.5 mm from the center and centered vertically with separation distances of 5, 4, 3, 2, and 1.5 mm. The total source powers varied slightly in each case due to slight differences in the local mesh geometry. The regularization parameter was set to 0.025 % of the maximum of the diagonal of the Hessian, and sources less than 10 % of the source maximum were rejected at each iteration. The results are shown in Figure 5.4.

The results indicate that the two sources can be distinguished down to a separation of 1.5 mm. At distances smaller than 1.5 mm the 1 mm diameter sources would be in contact due to the spacing of the nodes in the FEM mesh. The locations of each source were correctly recovered in all cases to within 0.5 mm. The total power of the reconstructed sources was also recovered to within 4 % in each case; however the total power of each individual source varied. There was a tendency for the algorithm to overestimate the power of the upper source while equally underestimating the power of the lower source. The over estimations were 1 %, 20 %, 26 %, 36 %, and 10 % at 5 mm to 1.5 mm separation distances respectively. The total powers of the reconstructed sources were calculated by integrating the source density over a region enclosing the non-zero values of the source strengths. The recovered source distributions were very sensitive to the choice of regularization factor. For these results, the regularization parameter that produced the lowest projection error was chosen in each case; however, for sources closer than 3 mm, several values resulted in a minimum projection error.

In these cases the distribution that best represents the true source locations are shown.

5.3 Instrumentation

The instrumentation for the BLT system is very similar to the previously described DOT/X-ray CT system. Two changes have been made to the setup described earlier – a new light source has been added to allow for multispectral imaging, and the light delivery method has been changed in order to simulate an internal bioluminescence source. The 635 nm diode laser is replaced with a 100 W filtered QTH light source (Oriel 68880). The source is coupled into a filter wheel with a set of 10 nm bandpass filters (560, 580, 600, 610, 620 and 640 nm, Thorlabs), which is in turn coupled into a 1 mm optical fiber. The spectrum of the light source at each of the six wavelengths is shown in Figure 5.5. The optical fiber is connected to a cylindrical light diffusing fiber with a length of 5 cm and diameter of 1.5 mm (DCYL 250, Diomed Inc.). The filtered light source effectively simulates the spectrum available for *in vivo* bioluminescence imaging (550 nm to 650 nm) while also covering the wavelength region of highly varying optical properties of the tissue simulating phantoms used for testing. This wavelength range also coincides with the region in tissue where the absorption due to hemoglobin decreases dramatically. It is this change in optical properties between successive wavelengths that provides the necessary change in photon transport to constrain the aforementioned BLT algorithm.

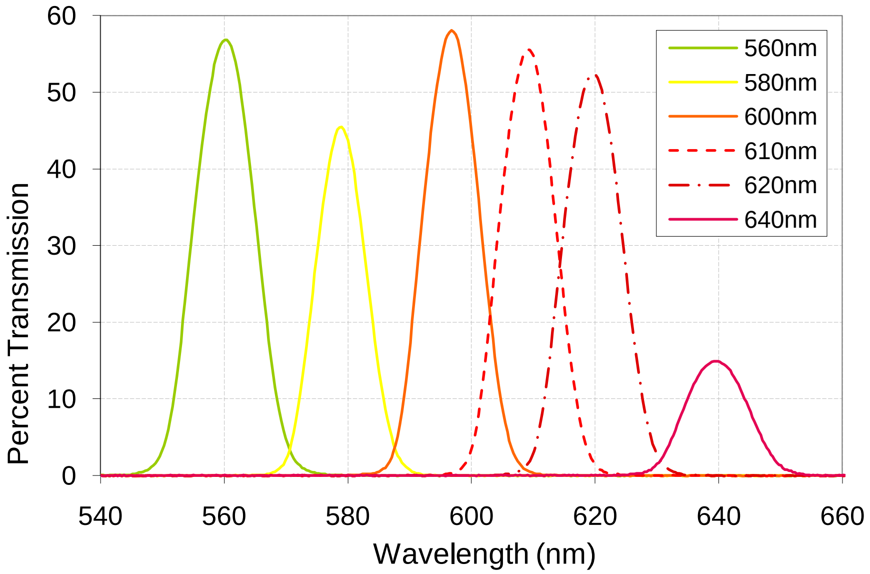

Figure 5.5. The spectrum of the filtered QTH light source at the six wavelengths used for BLT experiments.

5.3.1 Data Collection and Calibration

Data collection and calibration are similar to the methods employed in the DOT system, thus only the relevant changes will be discussed here. The boundary data are collected in an identical fashion to the DOT data in Chapter 4. The boundary flux is imaged onto a CCD camera, and custom Matlab software is used to map the boundary flux to the virtual detector in the NIRFAST FEM model. For BLT, a series of 64 uniformly spaced detectors is used. The data for a full 360 degree view of the subject are acquired by taking 4 images at 90 degree intervals. Integration times vary depending on the depth of the source, but generally range from 10 to 120 s. The large increase in integration time relative to the measurements in Chapter 4 is a result of the low power emitted from the filtered QTH source. Noise is reduced by cooling the CCD to -45 ºC.

Data calibration is necessary in BLT in order to determine the absolute source power and the source strength at each wavelength. The simplest method to calibrate the BLT data is to use a reference phantom with homogeneous optical properties as described in Chapter 4. The optical properties of the reference phantom are determined independently using steady-state spatially resolved diffuse reflectance. The cylindrical diffusing fiber is inserted into the center of the reference phantom and imaged in the same geometry as the unknown test source (4 images with 90 degrees angular spacing). The data are scaled using equation 4.12, in Chapter 4. The disadvantage of using this calibration method is that any inconsistencies and errors in the reference phantom optical properties will be reflected in the subsequently recovered source strengths.

A more robust calibration method would involve an absolute calibration of the light source used to simulate bioluminescence. This would require an accurate, absolute characterization of the cylindrical diffusing fiber at all angles and wavelengths. The boundary flux at the surface of the subject would also need to be corrected as our model of light propagation provides the boundary flux on the internal surface of the subject, not the flux that leaves and is imaged on the CCD. This complication is removed during the reference calibration with a homogeneous phantom.

The FEM mesh used in BLT is identical to the mesh used for the DOT experiments, but contains an additional field that specifies the source strength at each node in the mesh. The X-ray CT spatial priors are encoded in the recovered optical property maps from DOT experiments.

5.4 Experiments

A set of experiments was performed to demonstrate and validate the BLT reconstruction algorithm described earlier. The experiments also examine the optimal strategy for incorporating the *a priori* optical property distributions recovered from DOT into the BLT reconstruction. Multispectral DOT and BLT measurements were performed at five wavelengths using a single "bioluminescence" source placed in a tissue-simulating phantom. The cylindrical tissue-simulating phantom of 25 mm diameter and 100 mm height was composed of epoxy resin (Araldite GY502 & Aradur 837, Huntsman Corp.), India ink and titanium dioxide (region 1). A large cylindrical cavity with a diameter of 12 mm was filled with a liquid Intralipid (IL 20% Pharmacia Corp.) solution containing Epolight DT7-52A dye for absorption (region 2). The dye was chosen to mimic the optical properties of tissue over the spectral range of bioluminescence emission. The optical properties of the phantom are shown in Figure 5.6 and the phantom geometry is depicted in Figure 5.7. A single cylindrical diffusing fiber is used to simulate a 2D source of bioluminescence within the epoxy tissue-simulating phantom as shown in Figure 5.7c. The diffusing fiber has a diameter of 1.5 mm and is placed in the phantom at five locations separated by 2.5 mm.

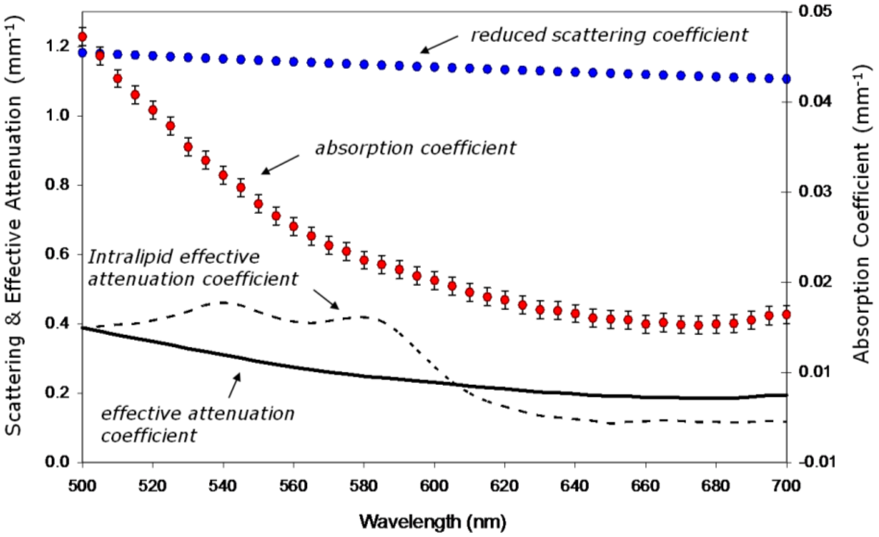

Figure 5.6. The optical properties of the tissue-simulating phantom used for the BLT experiments. The scattering, absorption and effective attenuation coefficients are shown for region 1, and the effective attenuation for region 2 (Intralipid solution) is shown.

The FEM mesh used for the DOT experiments was generated using segmented CT images of the phantom obtained from the integrated X-ray CT scanner. The FEM mesh consisted of 9560 nodes and 18835 triangular elements. The imaging geometry consisted of 25 virtual detectors, arranged in a 135 degree fan beam geometry and 16 source positions. Measurements were made at 560, 580, 600, 610, 620, and 640 nm. Images of the effective attenuation coefficient at each wavelength were reconstructed simultaneously using three spectrally constrained reconstruction algorithms described in Chapter 4. The three algorithms differ in their use of the X-ray CT spatial prior data; 1) repeated single-step Tikhonov method with no spatial priors, 2) hard spatial priors, and 3) soft spatial priors. The initial bulk homogeneous guess of optical properties was calculated using the methods described in section 4.3.5. The regularization parameter was set to 10, and the reconstruction basis was a 40 x 40 uniform Cartesian grid. Reconstructions were iterated until the difference between the forward data and the reconstructed data did not improve by more than 2 %.

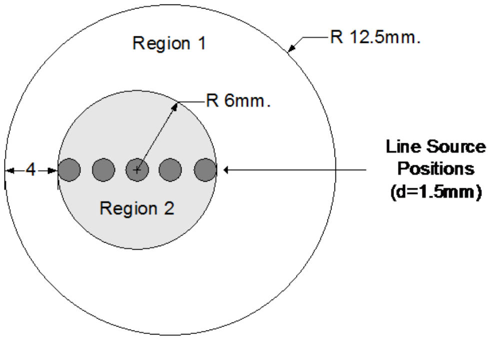

(a)

	X (mm)	Y (mm)
Position 1	0.46	7.50
Position 2	0.41	5.09
Position 3	0.26	2.54
Position 4	0.12	0.25
Position 5	0.07	-2.18

(b)

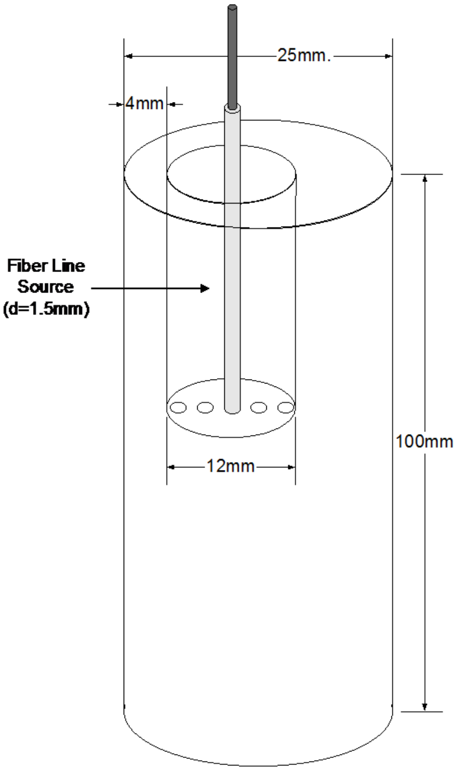

(c)

Figure 5.7. Geometry of the tissue-simulating phantom, (a) cross section view, and (c) 3D view. A large cylindrical cavity is machined, into which a cylindrical diffusing fiber of 1.5 mm diameter is inserted at the positions shown to simulate internal sources of bioluminescence. The actual source locations in the optical imaging plane determined from X-ray CT are shown in (b). Note: the cross section view in (a) is rotated CCW 90 degrees from the positions reported in (b).

The optical properties recovered from DOT were used as background optical properties in the BLT reconstructions. The BLT data were collected using 64 virtual detectors spaced uniformly around the tissue-simulating phantom at each wavelength and each source position as shown in Figure 5.4f. BLT images were reconstructed on a uniformly spaced 50 x 50 grid. The regularization parameter was reconstructed over the range of 0.1 to 0.0001 %, and the result with the lowest projection error was saved. Sources less than 10 % of the source maximum were rejected at each iteration and all six wavelengths were used for each reconstruction.

5.4.1 Source Power

The total power delivered by the cylindrical diffusing fiber was determined by using boundary measurements in a calibration phantom described earlier. The absolute calibration of the CCD camera described in Chapter 4 was used with an FE mesh of the calibration phantom with known optical properties to simulate the emittance of the 1.5 mm source located in the center of the homogeneous phantom. The source power was measured to be 205.3, 136.0, 242.5, 185.9, 148.1, and 34.0 nW/cm^2 at 560, 580, 600, 610, 620, and 640 nm respectively. These values qualitatively match the areas under the transmission curves plotted in Figure 5.5. The values are presented here for completeness, in practice the source power at each wavelength is removed from the BLT reconstruction during the data calibration step.

5.4.2 DOT Results and Discussion

The results of the optical property reconstructions are shown in Figure 5.8. The effective attenuation coefficient was reconstructed using three spectrally constrained reconstruction algorithms, a single-step Tikhonov method with no spatial priors, a hard priors method and a soft priors method. The true optical properties were determined independently using a steady-state spatially resolved reflectance system. The values plotted in Figure 5.8 are average effective attenuation coefficients for each distinct region in the phantom.

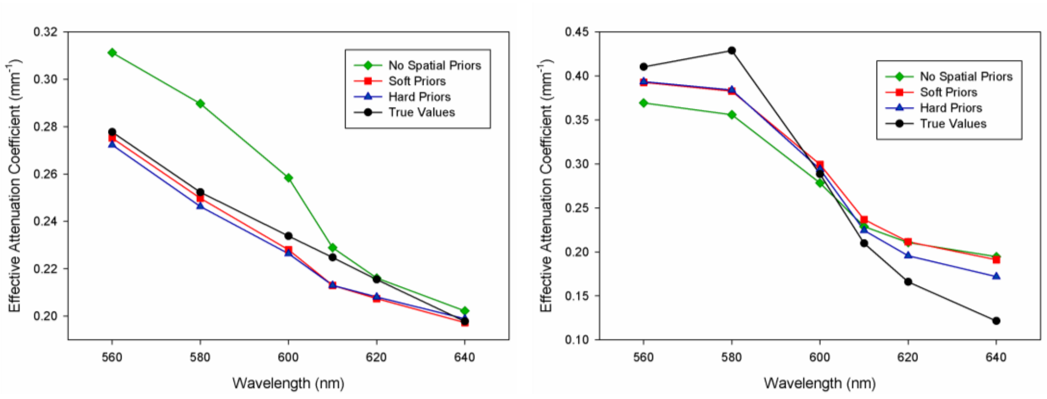

(a) **(b)**

Figure 5.8. The average effective attenuation reconstructed using three DOT reconstruction algorithms. In (a), the effective attenuation coefficient for region 1 in Figure 5.7 is depicted at each wavelength, while (b) contains the results for region 2.

The reconstruction methods using the structural *a priori* information improved the accuracy of the recovered effective attenuation coefficient at all wavelengths. The hard spatial prior method resulted in the most accurate recovery of the average effective attenuation coefficient in both regions of the tissue-simulating phantom. The average soft priors method values are very close to the hard priors values, however significant spatial variations from the mean values are present within each region (images not shown). However, the soft prior method resulted in more accurate recovery of the scattering coefficient (~ 30 % at each wavelength) versus the hard prior method where deviations as large at 70 % are present. The non-spatial Tikhonov method resulted in large standard deviations from the mean values, while average values differ by as much as 40 % from the true values. Also of note is the underestimation of the optical coefficients at 560 and 580 nm and overestimation of the values at 620 and 640 nm in region 2. This can be attributed to errors in the boundary flux at these wavelengths, which may be due to several factors. There can be errors in the determination of the “true” optical properties of the reference phantom (due to inhomogeneities from settling of the ink and TiO_2 particles within the epoxy resin - the optical properties are measured in a bulk resin sample, not at the exact location used for DOT). These variations may also be present within the tissue-simulating test phantom itself yielding inaccurate boundary data.

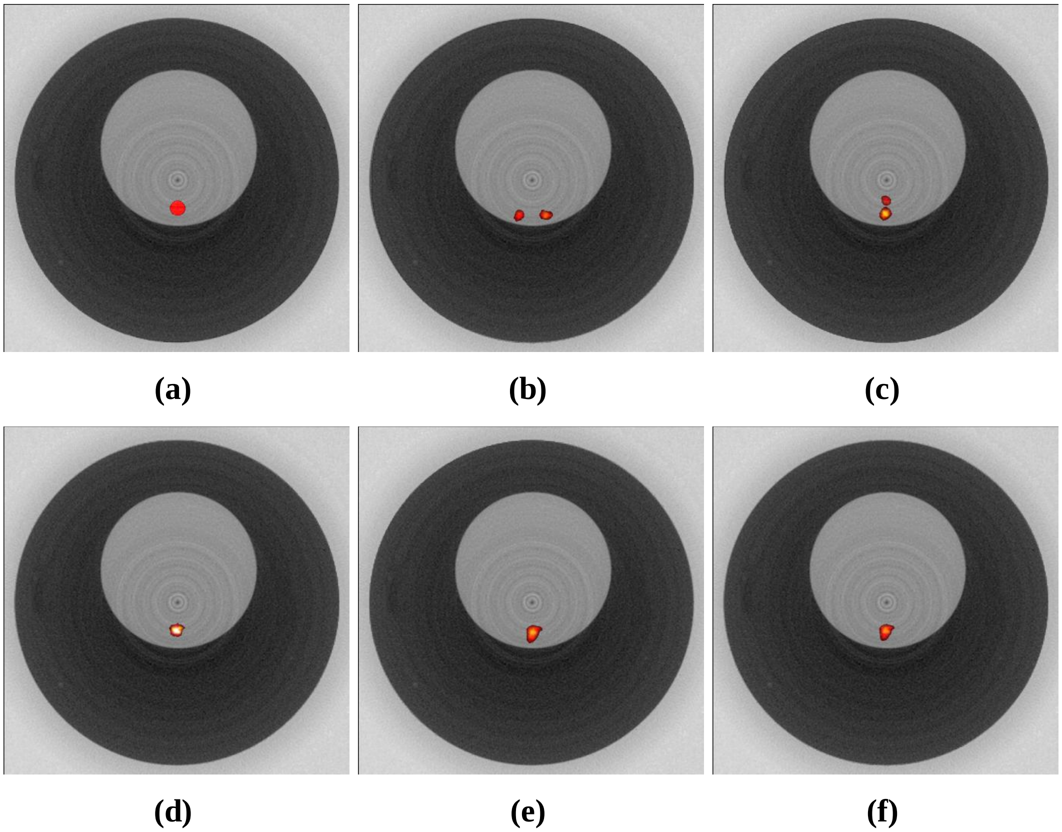

Figure 5.9. Reconstructed images of bioluminescence for a source with 1.5 mm diameter located at position “5” overlaid on a cross sectional X-ray CT image. (a) shows the true source location within the phantom. The five reconstructed images are as follows: (b) “true” effective attenuation values, (c) homogeneous background values, (d) non-spatial Tikhonov method, (e) soft spatial prior method, and (f) hard spatial prior method.

5.4.3 BLT Results and Discussion

The accuracy of the BLT reconstruction algorithm was examined using five different sets of optical property maps. The first set of optical properties is determined from a separate steady-state spatially resolved reflectance system. The optical properties obtained from this system are considered to be the “true” optical properties of the phantom. The second set of background optical properties used was a homogeneous effective attenuation distribution set to the “true” value of region 1 of the tissue simulating phantom. This set of optical properties represents an ideal estimate of the bulk tissue optical properties with no knowledge of the internal changes in absorption or scattering properties via some other *a priori* measurement technique. The final three sets of background optical properties are from the three spectral DOT reconstructions mentioned above. A representative set of reconstructed bioluminescence images is shown in Figure 5.9 for source position 5.

The images indicate that the use of *a priori* background optical property maps significantly improve the accuracy of the size and position of the internal bioluminescence source located at position 5, in the test phantom. All three DOT methods recover an accurate source position and location upon visual inspection, while the homogeneous and “true” background values result in two sources centered on the true source location. The inaccurate distribution of the homogeneous background method is not unexpected as this method provides no prior knowledge of the internal anomaly. The erroneous distribution using the “true” value is a peculiar result as this method would be expected to yield the most accurate images. This error might be attributed to inaccuracies in the tissue-simulating test phantom due to inhomogeneities in the epoxy material. In the case of such discrepancies the *a priori* DOT background optical properties are expected to perform better as they account for these inaccuracies by direct measurements of boundary data in the inhomogeneous regions. The total source power errors for each method were 16.5, 24.5, 40.9, 34.2, and 13.7 % for the “true” background properties, homogeneous properties, no spatial prior method, soft spatial method, and hard spatial method respectively. The hard spatial prior reconstruction method yields the most accurate source strength recovery.

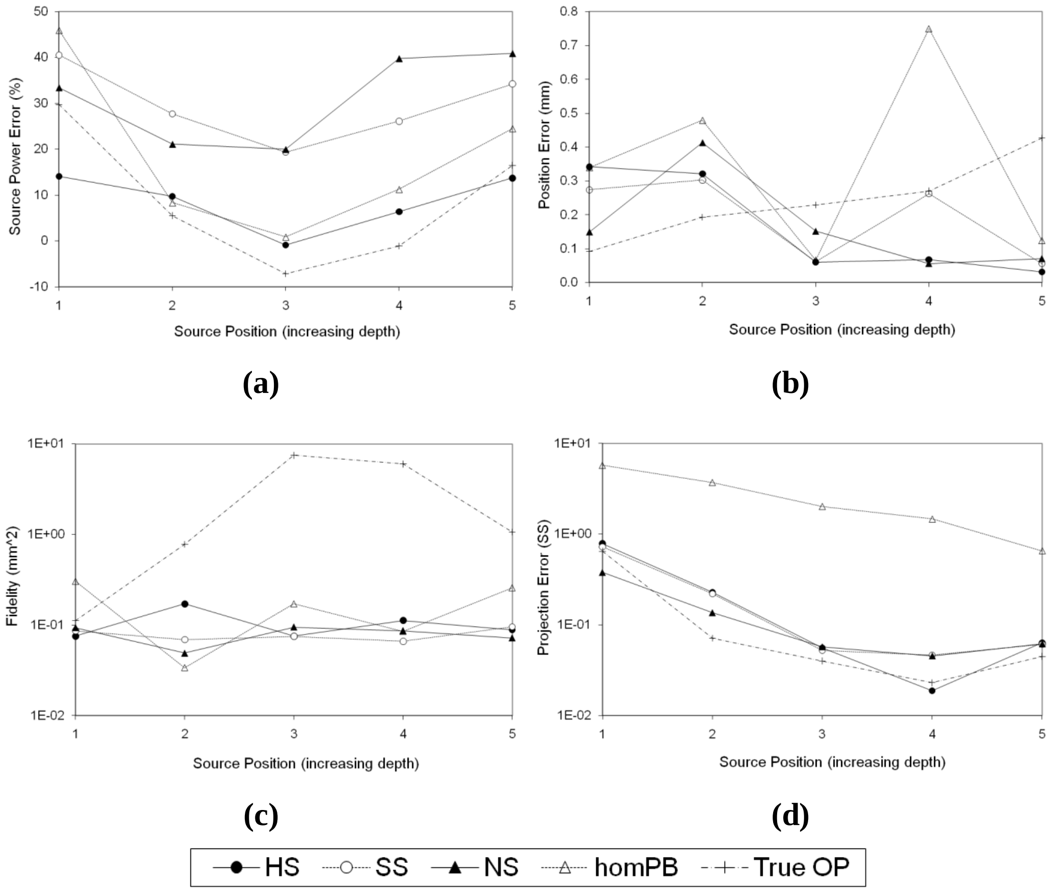

Figure 5.10. The results of bioluminescence reconstruction at all five source positions. (a) depicts the source power error at each source position. (b) contains the error in source position. (c) shows the source fidelity, a measure of the accuracy of the source shape. In (d) the projection error of each reconstruction is shown.

Figure 5.10 contains the results of all five source positions using each of the five reconstruction methods analyzed in terms of source power error, source position error, source fidelity and projection error. The total source power is calculated by integrating the source density over a region that encloses the non-zero values of the source distribution. The total source power was calculated most accurately by the “true” background optical property method and the hard spatial priors method for all source positions. There is an overall trend towards more accurate source strength recovery at position 3, with higher errors toward the phantom center and outer boundary. A possible reason for this trend is the distance of this source from any internal and external boundaries of the phantom. The diffusion approximation is known to provide inaccurate results close to regions with changing refractive index. The outer boundaries are corrected in NIRFAST, however the current model does not account for the index mismatch at the internal boundaries between the two phantom regions (region 1, RI ~ 1.55, region 2, RI ~1.39).

The source position error is calculated by determining the shift in the center of mass of the recovered source relative to the true source center of mass. There was no significant difference in the source position reconstruction among the different reconstruction methods, or the different source positions. The source position error was an average of ~0.2 mm for all methods, which corresponds to half the separation between nodes in the Cartesian grid used for reconstruction. The source fidelity depicted in Figure 5.10c is a measure of the accuracy and quality of the source shape. It is calculated as a second moment of the source strength at each node relative to the source center of mass:

$$\mathrm{Fidelity} = \sum_{\mathrm{i}=1}^{\mathrm{NN}} \mathrm{a_i r_i^2} \qquad (5.6)$$

where, NN are the total number of node in the FEM mesh, a_i are the source weights at each mesh and r_i is the distance from the source at position i to the source center of mass. Compact circular sources result in low fidelity values, while large sources, ring artifacts and multiple sources result in higher values of fidelity. Fidelity values below 0.1 were considered to be faithful to the true source distribution. All reconstruction methods except the “true” background properties result in acceptable source fidelity. The true background values have very large fidelity values indicating failure of the BLT reconstructions. Once again may be due to inhomogeneities present in the tests phantom or the refractive index mismatches at the region boundaries that are not accounted for using this method. Figure 5.10d contains the projection errors calculated for each reconstruction method. In general, the projection errors decrease as the source depth increases. The large values for the homogeneous optical property background assumption indicate a complete failure of the BLT algorithm to recover a faithful source distribution.

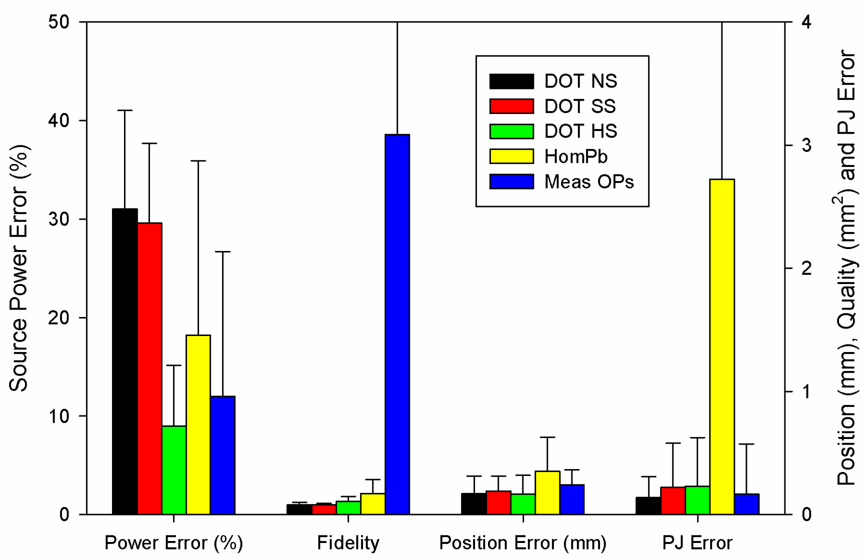

Figure 5.11. Summary of the accuracy of the recovered bioluminescence images for each reconstruction method. Each bar represents the average value over all five source position, while the error bars indicate the standard deviation in each value.

A summary of the results is shown in Figure 5.11. The average source power error, fidelity, position error and projection error for each reconstruction method is plotted. The figure provides a convenient overall synopsis of the performance of each method. The most accurate source power is recovered using the hard spatial prior method (9 %), followed closely by the “true” optical properties (12 %). The overall source fidelity values are comparable for all methods except the “true” background values, where a very large average fidelity indicates that inaccurate source distributions are obtained with this method. The source position error and projection error averages do not reveal any information not seen in Figure 5.10.

The importance of accurate optical property distributions in multispectral bioluminescence tomography has been demonstrated in the previous set of experiments. The accuracy of the reconstructed source strength and distribution depends heavily on the choice of background optical properties. The hard spatial prior method was found to provide the best overall recovery of total source strength, position, and fidelity at all source depths up to 12.5 mm. The results are similar to other studies which have also shown that using accuracte background optical properties for BLT results in a significant improvement in source recovery (24, 29, 30). Also revealed is a flaw in the current calibration method, where inhomogeneities in the reference and test phantoms can result in large inaccuracies in the recovered bioluminescence images. The calibration can be corrected by using an alternate phantom material or a more robust calibration method described in section 5.3.1.

5.5 Concluding remarks

An integrated multispectral BLT/DOT/X-ray CT system has been constructed and characterized. The BLT system uses a non-contact CCD camera to acquire surface emittance measurements and a reconstruction algorithm based on a FEM model of light propagation to recover the internal distribution of bioluminescence. The accuracy of the proposed bioluminescence reconstruction algorithm was demonstrated and validated using simulated and experimental data. The non-uniqueness of the BLT reconstruction problem was shown using simulations at single wavelengths. Multispectral measurements were shown to provide an accurate method for estimating the depth of a bioluminescence source due to the wavelength dependent attenuation of tissue. Inaccurate estimations of absorption and scattering were shown to have a relatively small effect on the recovered source distributions relative to errors in the bulk effective attenuation. The spatial resolution of the BLT algorithm was demonstrated down to a source separation of

1.5 mm. Experimental measurements have been presented which explore the importance of accurate estimates of background optical properties in BLT. Five methods were examined for incorporating background optical properties into the BLT. The hard spatial prior method was found to provide the best overall recovery of total source strength, position, and fidelity at all source depths up to 12.5 mm. The total source strength was recovered to within 8 %, while the source position was recovered to within 0.16 mm. No significant depth dependence was found using either method up to a depth of 12.5 mm. While presented here for bioluminescence reconstruction, the current imaging setup and reconstruction algorithms can be applied to fluorescence tomography with minimal modifications (108).

Some challenges remain to be solved, including the optimization of a more robust data calibration method. The incorporation of 3D measurements and more accurate numerical models based on the radiative transport equation also have the potential to improve the recovery of internal bioluminescence sources. These transport models are more accurate in small animals at the wavelengths used for bioluminescence imaging (24, 109). In this work, the hard spatial prior method provided the best recovered images, however this may not be the case in more complex geometries found *in vivo*. Further studies need to be performed to examine the optimal BLT reconstruction method for these geometries in 3D.

Chapter 6

Conclusions and Future Work

6.1 Conclusions

This thesis describes the design, construction, and characterization of an integrated multispectral BLT/DOT/X-ray CT imaging system. The system addresses many of the inherent problems encountered in planar bioluminescence imaging techniques, allowing for the recovery of more accurate and quantitative bioluminescence data. The integrated X-ray CT scanner provides anatomical information which aids in the visualization and localization of the recovered bioluminescence distributions and also helps to constrain the inverse reconstruction in the DOT system. The system accounts for the propagation of light through tissue by using the diffusion approximation to model light transport in tissue. DOT is used to recover accurate optical property distributions that are used in tomographic reconstructions of bioluminescent sources. Lastly, the BLT component makes use of multispectral emission information to constrain the BLT reconstruction.

In Chapter 2 the design and characterization of a cone beam X-ray CT portion of the system is described. The bench top X-ray CT scanner is based on a flat panel X-ray detector coupled to a gadolinium oxysulfide scintillator, a micro-focus X-ray source and a high precision rotation stage. The imaging performance of the X-ray source and FPD is examined in detail, including gain correction methods, system alignment techniques and contrast performance. The detector response curve was found to be non-linear at both low and high exposures. The response curve was "linearized" by using fitting the response of the detector with a 3rd order polynomial function. The modulation transfer function of the detector was measured at approximately 8.6 cycles/mm at 10% contrast by using the angled edge technique. Contrast phantom measurements demonstrate very good low dose contrast for soft tissue and bone, however soft tissue contrast is limited. Contrast-to-noise ratio measurements show that the CT scanner performance is quantum noise limited.

An important component for the development of the multispectral BLT system was the availability of suitable phantom materials that effectively simulate the structural and functional properties of human or animal tissue. Chapter 3 described the fabrication and characterization of the tissue-simulating phantoms that were used during the development of the BLT system. The optical properties of liquid and solid epoxy-based phantoms were investigated by measurements on a steady-state spatially resolved diffuse reflectance system. Several dyes were examined for their ability to mimic the absorption properties of tissue over the emission spectrum of luciferase (500–700 nm). These test phantoms were composed of a solid epoxy resin cylinder with machined cavities filled with liquids to simulate regions of differing optical properties. The liquid phantoms were easily reproducible and stable with all the dye combinations tested. They could be made before each experiment and stored for two weeks under refrigeration. The solid epoxy phantoms required a few days to fabricate and machine but their optical properties changed during the first few weeks after manufacture but stabilized 3 months after fabrication. For these phantoms, Epolight DT7-52A dye was the best option due to its relatively better stability and closer match to tissue over the range of 500 to 700 nm.

Chapter 4 described the development and evaluation of the integrated DOT/X-ray CT system and explored the optimal strategy for integrating the *a priori* X-ray CT data into the DOT reconstruction algorithm. A set of simulations were used to determine the optimal source detector geometry for the DOT system. Four image reconstruction algorithms were evaluated for their ability to recover the effective attenuation coefficients of a series of test phantoms. Two of the algorithms (a modified LM method, and a single-step Tikhonov method) did not use any *a priori* spatial information. Two other algorithms (hard priors and soft priors) used *a priori* structural information to constrain the reconstruction process. In addition, a spectrally constrained algorithm was investigated for use in multi-wavelength reconstructions. The inclusion of spatial priors improved the reconstructed image quality dramatically. The hard and soft priors methods resulted in similar recovered optical property distributions with RMS errors ranging from 8 % to 15 % in a series of test phantoms versus the errors with no spatial priors that ranged from 11 % to 26 %. The soft priors method was more resilient to imperfect *a priori* information. A 3 mm offset in the true location of an anomaly resulted in 12 % error in the effective attenuation coefficient, while the correct center position was maintained. The spectrally constrained algorithm was successful at removing the fluctuations in reconstructed scattering properties with wavelength characteristic of non-spectrally constrained methods with no change in the recovered effective attenuation coefficient.

The final chapter of this thesis described the design and evaluation of the multispectral bioluminescence tomography component of the system. The multispectral BLT system was used to recover accurate bioluminescence distributions in test phantoms using *a priori* background optical properties recovered from DOT. The accuracy of a proposed bioluminescence reconstruction algorithm was demonstrated and validated using simulated and experimental data. Multispectral measurements were shown to provide an accurate method for estimating the depth of a bioluminescence source due to the wavelength dependent attenuation of tissue. Inaccurate estimations of absorption and scattering (with correct effective attenuation) were shown to have a relatively small effect on the recovered source distributions relative to errors in the bulk effective attenuation. The spatial resolution of the BLT reconstruction algorithm was demonstrated down to a source separation of 1.5 mm. Experimental measurements have been presented which explore the importance of accurate estimates of background optical properties in BLT. Five methods were examined for incorporating background optical properties into the BLT. The hard spatial prior method was found to provide the best overall recovery of total source strength, position, and fidelity at all source depths up to 12.5 mm. The total source strength was recovered to within 8 %, while the source position was recovered to within 0.16 mm. No significant depth dependence was found using either method up to a depth of 12.5 mm. While presented here for bioluminescence reconstruction, the current imaging setup and reconstruction algorithms can be applied to other problems such a fluorescence tomography with minimal modifications.

6.2 Future Directions

This thesis described the successful design and characterization of an integrated multispectral BLT/DOT/X-ray CT system. Several challenges and optimizations remain to be investigated which can lead to multiple future research directions:

6.2.1 3D Imaging

The simulations and experiments presented in this thesis were performed in two dimensions to minimize the data collection and computational requirements but BLT is inherently a three dimensional problem. The instrumentation and algorithms presented in the thesis are ready for 3D data acquisition and reconstruction with very minimal modifications. Future work should focus on finding a suitable 3D segmentation and mesh generation routine, and optimizing the sources and detector locations for 3D DOT and BLT measurements. A series of phantom studies similar to those presented in this thesis need to be conducted using suitable 3D tissue-simulating phantoms and bioluminescence sources. The 3D phantoms could be constructed of multiple layers of epoxy material with distinct optical properties in each region. Three dimensional anomalies could be added by machining them to shape before assembly of the complete phantom. A method for eliminating air pockets and gaps due to inaccurate mating of phantom components would need to be developed. Suitable internal sources for 3D imaging include isotropic optical fibers or a capsule filled with a luciferase reagent solution.

6.2.2 Algorithm Development

The accurate simulation of light transport in tissue is a vital component in BLT reconstruction. To date, most light propagation models are based on the diffusion approximation to the radiative transport equation. While accurate in regions where scattering dominates absorption, the assumptions of the diffusion approximation begin to break down at shorter wavelengths and in domains containing small source-detector distances (110). With the rapid increase in computing power, several groups have been developing higher order approximations to the RTE with great success (24, 111, 112). These forward models provide even more accurate simulations of light transport in tissue, particularly at wavelengths were the diffusion approximation is no longer valid.

In addition to improvements in the forward model, the inverse reconstruction algorithms also have room for optimization. Currently there are a large number of research groups developing their own inverse algorithms in DOT and BLT. Each of these algorithms have their advantages and disadvantages, but there is potential for further improvements to the algorithms used in this thesis. Of note is an algorithm developed in our lab by Naser *et al*. were it was shown that an accurate recovery of both scattering and absorption coefficients is possible with the current CW measurement methods used in this thesis (46).

While the current work focused on bioluminescence tomography exclusively, the current instrumentation and algorithms can also be applied to fluorescence tomography. The inverse problem in florescence tomography is slightly more complex due to the need to model the forward propagation of the excitation light, but the larger signal available makes it useful for many applications where bioluminescence experiments are not possible.

6.2.3 Data Collection and Calibration

Further improvements can be made to the multispectral BLT system by increasing the data collection efficiency and the data calibration method. The current detection setup captures only a 135 degree field of view for each image on the CCD. A system of mirrors could be implemented to capture the boundary flux emitted over a much larger area of the subject. The increase in the available boundary data in DOT would help to further constrain the DOT algorithm.. In BLT the mirror system would decrease the required imaging time by cutting the required “views” for 360 degree coverage of the subject to as few a one (versus 4 used presently).

The data calibration procedure is currently the most significant source of error for both the DOT and BLT data acquisition steps in this thesis. Any errors in the determination of the optical properties of the reference phantom can result in inaccurate data calibration and subsequent inaccuracies in the recovered effective attenuation maps and internal source powers. Also, any inhomogeneities in the reference phantom can also result in inaccurate data calibration. Several solutions can be implemented in future work including the use an alternative method to measure the optical properties of the reference phantom, or using a phantom with more uniform optical properties (113). Another solution is to perform the calibration step using the BLT system itself via an absolute calibration of the source. This would require an accurate, absolute characterization of the cylindrical diffusing fiber (or other source in 3D) at all angles and wavelengths (114, 115). The boundary flux at the surface of the subject would also need to be corrected as the current model of light transport provides the emittance on the internal surface of the subject, not the emittance that leaves and is imaged on the CCD.

6.2.4 *In vivo* Experiments

As mentioned in Chapter 2, the X-ray CT system has limited soft tissue contrast which raises question as to its usefulness for constraining the optical imaging during *in vivo* experiments. In the current phantom work the *a priori* contrast information provided by the CT was shown to significantly increase the accuracy of the optical property distributions and internal bioluminescence source distributions. The efficacy of this method needs to be examined *in vivo*, where X-ray CT contrast may not be sufficient to differentiate important anatomical boundaries. The main assumption that regions segmented on the basis of X-ray attenuation correspond to regions of similar optical properties also needs to be examined in more detail. Despite these challenges, the information obtained from X-ray CT is still useful for obtaining surface contour information and could be used to warp a standard model of mouse anatomy onto the subject.

Another obstacle that needs to be overcome before fully 3D *in vivo* experiments are performed is an algorithm to compensate for the varied boundary emittance from a complex surface detected on the CCD camera. The experiments in this thesis used a reference phantom with the same geometry as the test phantoms to cancel the variations of boundary fluence with surface contours; however this will not be the case *in vivo*. The surface contour information provided by the X-ray CT can be used to correct for this effect as formulated by Ripoll and Ntziachristos (116).

Finally the imaging performance of the integrated multispectral BLT system will need to be more comprehensively characterized using a series of *in vivo* experiments. The accuracy of the recovered optical property maps will need to be examined, as well as the optimal incorporation of these maps into the BLT reconstruction algorithm. For BLT the quantitative accuracy and resolution performance of the BLT distributions needs to be characterized and optimized. A series of experiments should be performed to assess the ability of the system to recover sources of various strengths and sizes at different locations within the subject to identify the optimal applications for *in vivo* experiments. Initially the experiments could be conducted post mortem, using isotropic optical fibers inserted into various regions within the rodent at a range of source powers. The post mortem experiments could then be followed up by injecting living animals with cell lines that have been engineered to express luciferase, optimizing parameters including dose, imaging time, and sensitivity etc.

Appendix A – Epoxy Phantom Fabrication Procedure

The following describes the procedure used to make a series of tissue phantoms used to determine the absorption characteristics of Epolight 5411 and Epolight 5457 dyes when cured in an epoxy resin system. Thirteen phantoms were fabricated, six for each absorbing dye at various concentrations, and one phantom containing only TiO_2. The phantoms were constructed in two separate batches, one for each absorbing dye. The reduced scattering coefficient was fixed for all phantoms.

Stock solutions of the two powdered dyes were made in ethanol with concentrations of 0.8 mg/mL of Epolight 5411 and 1 mg/mL of Epolight 5457. All phantoms were then prepared from these stock solutions with the dye concentration quoted in microliters of stock dye solution per liter of epoxy resin (µL/L). The TiO_2 was also suspended in an ethanol solution to help ensure thorough mixing with the resin. In practice 4 mL of ethanol per gram of TiO_2 was enough to completely suspend the TiO_2 with minimal aggregation. Since both the dye and the TiO_2 are added to the resin from ethanol solutions, care must be taken to limit the amount of ethanol that is added. Large volumes of ethanol dilute the epoxy mixture and can affect the desired optical properties and curing time. The total quantity of ethanol used was minimized and generally was less than 2% of the total phantom volume.

Cylindrical phantoms with diameters of 5 cm and heights of 6 cm were cast using 125 mL of epoxy resin per phantom. The quantities of resin and hardener were determined by weight, with each phantom containing 108.9 g of resin and 28.3 g of hardener. Both the scatterers and dyes were added to the resin which was then degassed before addition of the hardener. In order to keep the scattering properties consistent for each dye series, 3.1 g of TiO_2 in 12 mL of ethanol was mixed with 679.4 g of resin. This resin solution was then split six ways before adding differing concentrations of dye. A pipette was used to add accurate quantities of stock dye solution and then the mixture was stirred with a glass rod until the dye was completely dispersed. Both dye mixtures had a light blue color when mixed in the resin.

The process of stirring introduces bubbles into the epoxy resin and it was necessary to degas the mixture prior to curing. Each phantom mixture was degassed in a desiccator for 10 min prior to the addition of the hardener and once again for 6 min after adding the hardener and pouring into a polystyrene mold. The polystyrene facilitated easy removal of the cured epoxy resin, even without the use of a mold release compound. After the addition of the hardener which had a slight orange tint, both dye mixtures underwent a dramatic color change. The Epolight 5411 mixture turned pale pink, while the Epolight 5457 mixture changed to a slightly darker pink at similar concentrations. This effect was due to a shift in the absorption peak of both dyes to a lower wavelength.

After degassing, the phantoms were left to cure in a water bath for 24 h. The water bath was used to lower the maximum temperature reached during the exothermic curing process. At least 48 h were required to harden the epoxy so that it could be machined. The top surface of each phantom was leveled using a lathe. Wet sandpaper was used to polish the surface by hand with increasing grit number, finishing with 600 grit sandpaper until all visible surface scratches had been removed.

References

(1) Beckmann N, Cannet C, Rausch M, Kneuer R, Gremlich HU. In Vivo Mouse Imaging and Spectroscopy in Drug Discovery. In: Borsook D, Beccera LR, Bullmore E, Hargreaves RJ, eds. Imaging in CNS Drug Discovery and Development Springer New York, 2009:229-250.

(2) Pomper MG. Translational molecular imaging for cancer. *Cancer Imaging* 2005;5 Spec No A:S16-S26.

(3) Kaijzel EL, van der Pluijm G, Löwik WGMC. Whole-Body Optical Imaging in Animal Models to Assess Cancer Development and Progression. *Clinical Cancer Research* 2007 Jun 15;13:3490-3497.

(4) Malakoff D. The rise of the mouse, biomedicine's model mammal. *Science* 2000 Apr 14;288:248-253.

(5) Zanzonico P. Noninvasive Imaging for Supporting Basic Research. In: Kiessling F, Pichler BJ, eds. Small Animal Imaging Springer Berlin Heidelberg, 2011:3-16.

(6) Kang JH, Chung JK. Molecular-genetic imaging based on reporter gene expression. *J Nucl Med* 2008 Jun;49 Suppl 2:164S-179S.

(7) Troy T, Jekic-McMullen D, Sambucetti L, Rice B. Quantitative comparison of the sensitivity of detection of fluorescent and bioluminescent reporters in animal models. *Mol Imaging* 2004 Jan;3:9-23.

(8) Winkeler A, Sena-Esteves M, Paulis LEM, et al. Switching on the Lights for Gene Therapy. *PLoS ONE* 2007;2:e528.

(9) Massoud TF, Paulmurugan R, De A, Ray P, Gambhir SS. Reporter gene imaging of protein-protein interactions in living subjects. *Current Opinion in Biotechnology* 2007 Feb;18:31-37.

(10) De A, Gambhir SS. Noninvasive imaging of protein-ûprotein interactions from live cells and living subjects using bioluminescence resonance energy transfer. *The FASEB Journal* 2005 Dec 1;19:2017-2019.

(11) Kaijzel EL, Snoeks TJ, Buijs JT, van der PG, Lowik CW. Multimodal imaging and treatment of bone metastasis. *Clin Exp Metastasis* 2009;26:371-379.

(12) Zhang L, Lee KC, Bhojani MS, et al. Molecular imaging of Akt kinase activity. *Nat Med* 2007 Sep;13:1114-1119.

(13) Zeamari S, Rumping G, Floot B, Lyons S, Stewart FA. In vivo bioluminescence imaging of locally disseminated colon carcinoma in rats. *Br J Cancer* 2004 Mar 2;90:1259-1264.

(14) Gross S, Piwnica-Worms D. Molecular imaging strategies for drug discovery and development. *Current Opinion in Chemical Biology* 2006 Aug;10:334-342.

(15) Rice BW, Cable MD, Nelson MB. In vivo imaging of light-emitting probes. *Journal of Biomedical Optics* 2001 Oct;6:432-440.

(16) Ge Wang, Yi Li, Ming Jiang. Uniqueness theorems in bioluminescence tomography. *Med Phys* 2004;31:2289-2299.

(17) Mark JHea. Development of an MR-compatible SPECT system (MRSPECT) for simultaneous data acquisition. *Physics in Medicine and Biology* 2010;55:1563.

(18) Mawlawi O, Townsend D. Multimodality imaging: an update on PET/CT technology. *European Journal of Nuclear Medicine and Molecular Imaging* 2009 Mar 1;36:15-29.

(19) Brooksby B, Pogue BW, Jiang S, et al. Imaging breast adipose and fibroglandular tissue molecular signatures by using hybrid MRI-guided near-infrared spectral tomography. *Proc Natl Acad Sci U S A* 2006 Jun 6;103:8828-8833.

(20) Yuan Z, Zhang Q, Sobel ES, Jiang H. Tomographic x-ray--guided three-dimensional diffuse optical tomography of osteoarthritis in the finger joints. *Journal of Biomedical Optics* 2008 Jul;13:044006-044010.

(21) Gulsen G, Birgul O, Unlu MB, Shafiiha R, Nalcioglu O. Combined diffuse optical tomography (DOT) and MRI system for cancer imaging in small animals. *Technol Cancer Res Treat* 2006 Aug;5:351-363.

(22) Guven M, Yazici B, Intes X, Chance B. Diffuse optical tomography with a priori anatomical information. *Physics in Medicine and Biology* 2005;50:2837-2858.

(23) Brooksby B, Brooksby B, Jiang S, et al. Combining near-infrared tomography and magnetic resonance imaging to study in vivo breast tissue: implementation of a Laplacian-type regularization to incorporate magnetic resonance structure. *J Biomed Opt* 2005 Sep;10:051504.

(24) Klose AD, Beattie BJ, Dehghani H, et al. In vivo bioluminescence tomography with a blocking-off finite-difference SP3 method and MRI/CT coregistration. *Med Phys* 2010 Jan;37:329-338.

(25) Kuo C, Coquoz O, Troy TL, Xu H, Rice BW. Three-dimensional reconstruction of in vivo bioluminescent sources based on multispectral imaging. *Journal of Biomedical Optics* 2007 Mar;12:024007-024012.

(26) Liu K, Yang X, Liu D, et al. Spectrally resolved three-dimensional bioluminescence tomography with a level-set strategy. *J Opt Soc Am A* 2010 Jun 1;27:1413-1423.

(27) Gu X, Zhang Q, Larcom L, Jiang H. Three-dimensional bioluminescence tomography with model-based reconstruction. *Opt Express* 2004 Aug 23;12:3996-4000.

(28) George Alexandrakis et al. Tomographic bioluminescence imaging by use of a combined optical-PET (OPET) system: a computer simulation feasibility study. *Physics in Medicine and Biology* 2005;50:4225.

(29) Liu J, Wang Y, Qu X, et al. In vivo quantitative bioluminescence tomography using heterogeneous and homogeneous mouse models. *Opt Express* 2010 Jun 7;18:13102-13113.

(30) Alexandrakis G, Rannou FR, Chatziioannou AF. Effect of optical property estimation accuracy on tomographic bioluminescence imaging: simulation of a combined optical PET (OPET) system. *Physics in Medicine and Biology* 2006;51:2045-2053.

(31) Wang G, Cong W, Durairaj K, et al. In vivo mouse studies with bioluminescence tomography. *Opt Express* 2006 Aug 21;14:7801-7809.

(32) Cong A, Wenxiang C, Yujie L, Santago P, Chatziioannou A, Ge W. Differential Evolution Approach for Regularized Bioluminescence Tomography. *Biomedical Engineering, IEEE Transactions on* 2010 Sep;57:2229-2238.

(33) Liji Cao and Jorg Peter. Bayesian reconstruction strategy of fluorescence-mediated tomography using an integrated SPECT-CT-OT system. *Physics in Medicine and Biology* 2010;55:2693.

(34) Tian J, Liu K, Lu Y, et al. Evaluation of the simplified spherical harmonics approximation in bioluminescence tomography through heterogeneous mouse models. *Opt Express* 2010 Sep 27;18:20988-21002.

(35) Yan H, Unlu MB, Nalcioglu O, Gulsen G. Bioluminescence tomography with structural and functional a priori information. San Francisco, California, USA: SPIE; 2010 755712-755716.

(36) Kim JB, Urban K, Cochran E, et al. Non-invasive detection of a small number of bioluminescent cancer cells in vivo. *PLoS One* 2010;5:e9364.

(37) Zhao H, Doyle TC, Coquoz O, Kalish F, Rice BW, Contag CH. Emission spectra of bioluminescent reporters and interaction with mammalian tissue determine the sensitivity of detection in vivo. *Journal of Biomedical Optics* 2005 Jul;10:041210-041219.

(38) Paroo Z, Bollinger RA, Braasch DA, et al. Validating bioluminescence imaging as a high-throughput, quantitative modality for assessing tumor burden. *Mol Imaging* 2004 Apr;3:117-124.

(39) Cheong W, Prahl S, Welch A. A review of the optical properties of biological tissues. *Quantum Electronics, IEEE Journal of* 1990;26:2166-2185.

(40) Patterson MS, Wilson BC, Wyman DR. The propagation of optical radiation in tissue I. Models of radiation transport and their application. *Lasers in Medical Science* 1991 Jun 1;6:155-168.

(41) Flock ST, Wilson BC, Patterson MS. Total attenuation coefficients and scattering phase functions of tissues and phantom materials at 633 nm. *Med Phys* 1987 Sep;14:835-841.

(42) Jacques S, Patterson MS. Light-tissue Interactions. In: Webb CE, Jones J.D.C., eds. Handbook of laser technology and applications IOP Publishing, 2004:1955-1993.

(43) Comsa DC, et al. Bioluminescence imaging of point sources implanted in small animals post mortem: evaluation of a method for estimating source strength and depth. *Physics in Medicine and Biology* 2007;52:5415.

(44) Dehghani H, Davis SC, Jiang S, Pogue BW, Paulsen KD, Patterson MS. Spectrally resolved bioluminescence optical tomography. *Opt Lett* 2006 Feb 1;31:365-367.

(45) Chaudhari AJ, Darvas F, Bading JR, et al. Hyperspectral and multispectral bioluminescence optical tomography for small animal imaging. *Phys Med Biol* 2005 Dec 7;50:5421-5441.

(46) Naser MA, Patterson MS. Algorithms for bioluminescence tomography incorporating anatomical information and reconstruction of tissue optical properties. *Biomed Opt Express* 2010 Sep 1;1:512-526.

(47) Boas DA, Brooks DH, Miller EL, et al. Imaging the body with diffuse optical tomography. *Signal Processing Magazine, IEEE* 2001 Nov;18:57-75.

(48) Dehghani H, Pogue BW, Poplack SP, Paulsen KD. Multiwavelength Three-Dimensional Near-Infrared Tomography of the Breast: Initial Simulation, Phantom, and Clinical Results. *Appl Opt* 2003 Jan 1;42:135-145.

(49) Dehghani H, White BR, Zeff BW, Tizzard A, Culver JP. Depth sensitivity and image reconstruction analysis of dense imaging arrays for mapping brain function with diffuse optical tomography. *Appl Opt* 2009 Apr 1;48:D137-D143.

(50) Srinivasan S, Pogue BW, Carpenter C, Yalavarthy PK, Paulsen K. A boundary element approach for image-guided near-infrared absorption and scatter estimation. *Med Phys* 2007 Nov;34:4545-4557.

(51) Simon RA, Schotland CJ. Optical tomography: forward and inverse problems. *Inverse Problems* 2009;25:123010.

(52) Wang L, Jacques SL, Zheng L. MCML--Monte Carlo modeling of light transport in multi-layered tissues. *Computer Methods and Programs in Biomedicine* 1995 Jul;47:131-146.

(53) Gandjbakhche AH, Weiss GH. V: Random Walk and Diffusion-Like Models of Photon Migration in Turbid Media. In: Wolf E, ed. Progress in Optics, Volume 34 ed Elsevier, 1995:333-402.

(54) Arridge et al SR. The theoretical basis for the determination of optical pathlengths in tissue: temporal and frequency analysis. *Physics in Medicine and Biology* 1992;37:1531.

(55) Arridge SR, Schweiger M, Hiraoka M, Delpy DT. A finite element approach for modeling photon transport in tissue. *Med Phys* 1993 Mar;20:299-309.

(56) Paulsen KD, Jiang H. Spatially varying optical property reconstruction using a finite element diffusion equation approximation. *Med Phys* 1995 Jun;22:691-701.

(57) Dehghani H, Brooksby B, Vishvanath K, Pogue BW, Paulsen KD. The effects of internal refractive index variation in near-infrared optical tomography: a finite element modelling approach. *Physics in Medicine and Biology* 2003;48:2713.

(58) Hielscher AH, Alcouffe RE, Barbour RL. Comparison of finite-difference transport and diffusion calculations for photon migration in homogeneous and heterogeneous tissues. *Physics in Medicine and Biology* 1998;43:1285.

(59) Ren K, Abdoulaev GS, Bal G, Hielscher AH. Algorithm for solving the equation of radiative transferin the frequency domain. *Opt Lett* 2004 Mar 15;29:578-580.

(60) Ryzhik L, Papanicolaou G, Keller JB. Transport equations for elastic and other waves in random media. *Wave Motion* 1996 Dec;24:327-370.

(61) Haskell RC, Svaasand LO, Tsay TT, Feng TC, McAdams MS, Tromberg BJ. Boundary conditions for the diffusion equation in radiative transfer. *J Opt Soc Am A* 1994 Oct 1;11:2727-2741.

(62) Farrell TJ, Patterson MS, Wilson B. A diffusion theory model of spatially resolved, steady-state diffuse reflectance for the noninvasive determination of tissue optical properties in vivo. *Med Phys* 1992 Jul;19:879-888.

(63) Schweiger M, Arridge SR, Hiraoka M, Delpy DT. The finite element method for the propagation of light in scattering media: boundary and source conditions. *Med Phys* 1995 Nov;22:1779-1792.

(64) Pekar J, Patterson MS. Fabrication and characterization of phantoms with tissue-like optical properties from 500 to 700 nm. *Medical Laser Application* 2010 Aug;25:147-153.

(65) Feldkamp LA, Davis LC, Kress JW. Practical cone-beam algorithm. *J Opt Soc Am A* 1984 Jun 1;1:612-619.

(66) Paulus MJ, Gleason SS, Kennel SJ, Hunsicker PR, Johnson DK. High resolution X-ray computed tomography: an emerging tool for small animal cancer research. *Neoplasia* 2000 Jan;2:62-70.

(67) Huyn Kim K, Cho G. Radiation effects on the resolution (MTF) of the scintillator coupled CMOS APS array imager for non-destructive test X-ray imaging. *Annals of Nuclear Energy* 2004 May;31:805-811.

(68) Polynomial Gain Correction for RadEye Sensors. Santa Clara, CA: Rad-icon Imaging Corp; 2005.

(69) Samei E, Flynn MJ, Reimann DA. A method for measuring the presampled MTF of digital radiographic systems using an edge test device. *Medical Physics* 1998 Jan;25:102-113.

(70) Jeong MH, Cho HS, Kim S, et al. Development of a portable digital radiographic system based on FOP-coupled CMOS image sensor and its performance evaluation. 2004 1604-1609.

(71) Dobbins III JT, Ergun DL, Rutz L, Hinshaw DA, Blume H, Clark DC. DQE(f) of four generations of computed radiography acquisition devices. *Medical Physics* 1995 Oct;22:1581-1593.

(72) DQE Measurements for RadEye EV Sensors. Santa Clara, CA: Rad-icon Imaging Corp; 2005.

(73) Wang H, Smith MF, Stone CD, Jaszczak RJ. Astigmatic single photon emission computed tomography imaging with a displaced center of rotation. *Medical Physics* 1998 Aug;25:1493-1501.

(74) White TA, Roney TJ, Pink RJ, et al. Comparison of fan- and cone-beam imaging capabilities on a portable x-ray imaging system. Denver, CO, USA: SPIE; 1999 138-146.

(75) Noo F, Clackdoyle R, Mennessier C, White TA, Roney TJ. Analytic method based on identification of ellipse parameters for scanner calibration in cone-beam tomography. *Phys Med Biol* 2000 Nov;45:3489-3508.

(76) Hubbell JH, Seltzer SM. Tables of X-Ray Mass Attenuation Coefficients and Mass Energy-Absorption Coefficients from 1 keV to 20 MeV for Elements Z = 1 to 92 and 48 Additional Substances of Dosimetric Interest. 2006.

(77) Pogue BW, Patterson MS. Review of tissue simulating phantoms for optical spectroscopy, imaging and dosimetry. *J Biomed Opt* 2006 Jul;11:041102.

(78) Moffitt T, Chen YC, Prahl SA. Preparation and characterization of polyurethane optical phantoms. *J Biomed Opt* 2006 Jul;11:041103.

(79) Brooksby B, Jiang S, Dehghani H, et al. Combining near-infrared tomography and magnetic resonance imaging to study in vivo breast tissue: implementation of a Laplacian-type regularization to incorporate magnetic resonance structure. *J Biomed Opt* 2005 Sep;10:051504.

(80) Grossweiner LI. Optical dosimetry in photodynamic therapy. *Lasers Surg Med* 1986;6:462-466.

(81) Flock ST, Jacques SL, Wilson BC, Star WM, van Gemert MJ. Optical properties of Intralipid: a phantom medium for light propagation studies. *Lasers Surg Med* 1992;12:510-519.

(82) Madsen EL, Hobson MA, Shi H, Varghese T, Frank GR. Tissue-mimicking agar/gelatin materials for use in heterogeneous elastography phantoms. *Phys Med Biol* 2005 Dec 7;50:5597-5618.

(83) Wagnieres G, Cheng S, Zellweger M, et al. An optical phantom with tissue-like properties in the visible for use in PDT and fluorescence spectroscopy. *Phys Med Biol* 1997 Jul;42:1415-1426.

(84) Iizuka MN, Sherar MD, Vitkin IA. Optical phantom materials for near infrared laser photocoagulation studies. *Lasers Surg Med* 1999;25:159-169.

(85) Firbank M, Oda M, Delpy DT. An improved design for a stable and reproducible phantom material for use in near-infrared spectroscopy and imaging. *Phys Med Biol* 1995 May;40:955-961.

(86) Sukowski U, Schubert F, Grosenick D, Rinneberg H. Preparation of solid phantoms with defined scattering and absorption properties for optical tomography. *Physics in Medicine and Biology* 1996;41:1823-1844.

(87) Bays R, Wagnieres G, Robert D, et al. Three-dimensional optical phantom and its application in photodynamic therapy. *Lasers Surg Med* 1997;21:227-234.

(88) Di Ninni P, Martelli F, Zaccanti G. The use of India ink in tissue-simulating phantoms. *Opt Express* 2010 Dec 20;18:26854-26865.

(89) Farrell TJ, Patterson MS, Wilson B. A diffusion theory model of spatially resolved, steady-state diffuse reflectance for the noninvasive determination of tissue optical properties in vivo. *Med Phys* 1992 Jul;19:879-888.

(90) Hyde DE, Farrell TJ, Patterson MS, Wilson BC. A diffusion theory model of spatially resolved fluorescence from depth-dependent fluorophore concentrations. *Phys Med Biol* 2001 Feb;46:369-383.

(91) Diamond KR, Farrell TJ, Patterson MS. Measurement of fluorophore concentrations and fluorescence quantum yield in tissue-simulating phantoms using three diffusion models of steady-state spatially resolved fluorescence. *Phys Med Biol* 2003 Dec 21;48:4135-4149.

(92) Kienle A, Patterson MS. Determination of the optical properties of turbid media from a single Monte Carlo simulation. *Phys Med Biol* 1996 Oct;41:2221-2227.

(93) Weersink RA, Hayward JE, Diamond KR, Patterson MS. Accuracy of noninvasive in vivo measurements of photosensitizer uptake based on a diffusion model of reflectance spectroscopy. *Photochem Photobiol* 1997 Sep;66:326-335.

(94) Prahl S A. Optical absorption of hemoglobin. 1998.

(95) Dehghani H, Srinivasan S, Pogue BW, Gibson A. Numerical modelling and image reconstruction in diffuse optical tomography. *Philos Transact A Math Phys Eng Sci* 2009 Aug 13;367:3073-3093.

(96) Yalavarthy PK, Pogue BW, Dehghani H, Paulsen KD. Weight-matrix structured regularization provides optimal generalized least-squares estimate in diffuse optical tomography. *Med Phys* 2007 Jun;34:2085-2098.

(97) Dehghani H, Carpenter CM, Yalavarthy PK, Pogue BW, Culver JP. Structural a priori information in near-infrared optical tomography. San Jose, CA, USA: SPIE; 2007 64310B-7.

(98) Marquardt DW. An Algorithm for Least-Squares Estimation of Nonlinear Parameters. *Journal of the Society for Industrial and Applied Mathematics* 1963 Jun 1;11:431-441.

(99) Ntziachristos V, Yodh AG, Schnall M, Chance B. Concurrent MRI and diffuse optical tomography of breast after indocyanine green enhancement. *Proceedings of the National Academy of Sciences of the United States of America* 2000 Mar 14;97:2767-2772.

(100) Yalavarthy PK, Pogue BW, Dehghani H, Carpenter CM, Jiang S, Paulsen KD. Structural information within regularization matrices improves near infrared diffuse optical tomography. *Opt Express* 2007 Jun 25;15:8043-8058.

(101) Mourant JR, Fuselier T, Boyer J, Johnson TM, Bigio IJ. Predictions and measurements of scattering and absorption over broad wavelength ranges in tissue phantoms. *Appl Opt* 1997 Feb 1;36:949-957.

(102) Wang X, Pogue BW, Jiang S, et al. Image reconstruction of effective Mie scattering parameters of breast tissue in vivo with near-infrared tomography. *Journal of Biomedical Optics* 2006 Jul;11:041106-041113.

(103) Savitzky A, Golay MJE. Smoothing and Differentiation of Data by Simplified Least Squares Procedures. *Analytical Chemistry* 1964 Jul 1;36:1627-1639.

(104) Kepshire DS, Davis SC, Dehghani H, Paulsen KD, Pogue BW. Subsurface diffuse optical tomography can localize absorber and fluorescent objects but recovered image sensitivity is nonlinear with depth. *Appl Opt* 2007 Apr 1;46:1669-1678.

(105) Shewchuk JR. Delaunay refinement algorithms for triangular mesh generation. *Computational Geometry* 2002 May;22:21-74.

(106) Dehghani H, Davis SC, Pogue BW. Spectrally resolved bioluminescence tomography using the reciprocity approach. *Med Phys* 2008 Nov;35:4863-4871.

(107) Kuo C, Coquoz O, Troy TL, Xu H, Rice BW. Three-dimensional reconstruction of in vivo bioluminescent sources based on multispectral imaging. *J Biomed Opt* 2007 Mar;12:024007.

(108) Naser MA, Patterson MS. Improved bioluminescence and fluorescence reconstruction algorithms using diffuse optical tomography, normalized data, and optimized selection of the permissible source region. *Biomed Opt Express* 2011 Jan 1;2:169-184.

(109) Chu M, et al. Light transport in biological tissue using three-dimensional frequency-domain simplified spherical harmonics equations. *Physics in Medicine and Biology* 2009;54:2493.

(110) Klose AD. The forward and inverse problem in tissue optics based on the radiative transfer equation: A brief review. *Journal of Quantitative Spectroscopy and Radiative Transfer* 2010 Jul;111:1852-1853.

(111) Wright S, Schweiger M, Arridge SR. Reconstruction in optical tomography using the PN approximations. *Measurement Science and Technology* 2007;18:79.

(112) Lu Y, Machado HB, Douraghy A, Stout D, Herschman H, Chatziioannou AF. Experimental bioluminescence tomography with fully parallel radiative-transfer-based reconstruction framework. *Opt Express* 2009 Sep 14;17:16681-16695.

(113) Bouchard JP, Veilleux I, Jedidi R, Noiseux I, Fortin M, Mermut O. Reference optical phantoms for diffuse optical spectroscopy. Part 1: Error analysis of a time resolved transmittance characterization method. *Opt Express* 2010 May 24;18:11495-11507.

(114) Vesselov LM, Whittington W, Lilge L. Performance evaluation of cylindrical fiber optic light diffusers for biomedical applications. *Lasers Surg Med* 2004;34:348-351.

(115) Van Staveren H, Marijnissen H, Aalders M, Star W. Construction, quality assurance and calibration of spherical isotropic fibre optic light diffusers. *Lasers in Medical Science* 1995 Jun 10;10:137-147.

(116) Ripoll J, Ntziachristos V. Imaging Scattering Media from a Distance: Theory and Applications of Noncontact Optical Tomography. *Modern Physics Letters B* 2004;18:1403-1431.